Design of an Experimental Test Set-up for Buckling of a Trailing Edge Composite Bonded Joint Specimen Based on Semi-analytical and Numerical Models

Luis Eduardo Espinosa Chavez

November 27th, 2017

Faculty of Aerospace Engineering · Delft University of Technology

Design of an Experimental Test Set-up for Buckling of a Trailing Edge Composite Bonded Joint Specimen Based on Semi-analytical and Numerical Models

By

Luis Eduardo Espinosa Chavez

in partial fulfilment of the requirements for the degree of

Master of Science

in Aerospace Engineering at the Delft University of Technology,

and

Master of Science

in Engineering Wind Energy at Technical University of Denmark

To be defended on November 27, 2017.

Supervisors:	Dr. Ir. Kim Branner	DTU
	Dr. Ir. P. U. Haselbach	DTU
	Dr. Ir. S. Teixeira De Freitas	TU Delft
	Dr. F. Lahuerta Calahorra	WMC
Thesis committee:	Dr. Ir. Roland Schmehl	TU Delft
	Dr. Ir. Julie Teuwen	TU Delft

An electronic version of this thesis is available at http://repository.tudelft.nl/.

TU Delft

DTU Technical University of Denmark

Knowledge Centre WMC

Abstract

The trailing edge of wind turbine blades are commonly manufactured as an adhesive joint of the pressure-side and suction-side composite panels of the blade. Under some conditions, a lead-to-trailing (LTT) edgewise bending moment can induce buckling at the trailing edge adhesive joint, which may lead to early failure of the blade due to delamination. As a structural instability, buckling in wind turbines has been the focus of much research especially in full-scale tests and more recently at the sub-component level. These higher-level tests, however, are done on pre-manufactured wind turbine blades and require extensive preparation in order to adapt the testing rig to each blade section, as well as incurring into elevated costs.

An additional test level has been suggested for elements and details of wind turbine blades. It has been suggested that this level can fulfill many purposes: New concepts, modifications, material combinations and orientations can be tested, partial safety factors of larger scale tests can be reduced or even certifying minor details of the blade can be done at the element and detail level. As such, the focus of this project is to develop a testing method for a simplified trailing edge bonded joint with a custom designed hinged clamping system upon which a compressive moment can be imposed to induce buckling.

The design of this test will initially be based on a semi-analytical buckling plate model, where in-plane and out-of-plane displacements are coupled through the Von Karman strain-displacement relations. This semi-analytical tool is employed to quickly estimate the buckling loads for plates of varying dimensions. Strain-free imperfections can be included in the model for twisted/pre-bent plates in order to estimate their effect on reducing the load-bearing capacity of the structure. The semi-analytical tool is complemented with FE models for all the design parameters.

The semi-analytical and numerical results are compared to demonstrate the agreement of both approaches aimed to provide a sturdy base for the research. Next, the experimental buckling loads and force-displacement curves are shown against the predictions from the previous approaches with good agreement. Nevertheless, the observable discrepancies between the experimental and numerical results showed that the desired joint-fixity at the boundaries was not fully realized, therefore leading to a slightly different post-buckling behavior. In the end, suggestions are given to improve on the experimental clamping system in order to improve and expand the scope of this research.

Dedicatory and Acknowledgements

"In eternity there is no time, only an instant long enough for a joke."

— Hermann Hesse, Steppenwolf

One of the most valuable lessons that the last two years and a half have taught me, while I have been working to obtain my Master's Degree, is strangely enough, not an academic one. It is one about the appreciation of life; to find the humor and joy in every situation even at times when life deals us a bad hand. And it was MUCH easier to find the positive side of things when surrounded by people that supported me and encouraged me at every step of the way.

During this time, I have been lucky to be within an amazing group of friends that were always a constant source of inspiration. Whether newly forged friendships with people from the EWEM Program, the amazing (ex)board of ASE 'Aeolus', or those friends that despite the 9,000 km of distance always found a way to stay connected, I feel lucky to have shared this experience with you.

I want to thank the entire staff at Knowledge Center WMC, who made me feel welcome and part of the team during my every day at their facility. Special thanks to Sandra van den Outenaar for all your help during my transition between Denmark and The Netherlands, in all the administrative matters and more importantly for the help in finding me a roof over my head. Ben Hendriks for giving me the opportunity to be part of the team and for being a great (and humorous) leader. Rogier Nijssen, Koen Schellevis, Frank Stroet and Maarten Jan de Ruiter for their help during the project. Sibrand Raijmaekers and Remko de Ronde for turning the daily one-hour commute into an enjoyable time with good conversation, music, and my occasional snore.

Pushing myself to reach new heights, to deliver the best possible result would not have been possible without the encouragement and supervision of Sofia Teixeira, Philipp Ulrich Haselbach, Kim Branner and Francisco Lahuerta. Although difficult at times, I could not be any more grateful for the high standards that you held me to. Thank you for making me strive to become a better engineer.

Last, but certainly not least, this thesis would not have been possible without the presence of my family. I consider myself an extremely lucky person to have landed in a family of great values, and of people that were a constant reminder that I was not alone in this experience, at every high and every low. Thank you, Julia, Pedro and Monica, for keeping that brotherly and sisterly bond strong.

And thank you, Angelica and Emilio, for your constant support, encouragement, inspiration, and for being exemplary parents and role models.

The author acknowledges and is thankful for the contribution of the EU 7th framework programs FP7-ENERGY-2013 IRPWIND Project (under Grant Agreement 609795) and the Dutch TKI-WoZ research SLOWIND project to motivate and partly fund this research.

Table of Contents

Symbols & Abbreviations

Roman Notation & Symbols

a ..... Plate's length
$[A]$ ..... Stretching-Shearing Stiffness Matrix
AR ..... Plate's aspect ratio
b ..... Plate's width
b_l ..... Adhesive length
b_t ..... Adhesive thickness
$[B]$ ..... Stretching-Bending Coupling Matrix
$[D]$ ..... Bending-Twisting Stiffness Matrix
E ..... Young's Modulus
fs_t ..... Composite facesheet thickness
G ..... Shear Modulus
G_{perma} ..... Permanent glue contact constraint in FE
G_{break} ..... Breakable glue contact constraint in FE (dependent on adhesive properties)
h ..... Plate's absolute thickness
$[K_s]$ ..... Eigenvalue problem stiffness matrix
$[K_g]$ ..... Eigenvalue problem geometric matrix
K_a ..... Effective length factor for plate's length a
K_b ..... Effective length factor for plate's width b
m ..... Buckling mode / half-sine waves
M_x ..... Edge distributed bending moment around x-axis
M_y ..... Edge distributed bending moment around y-axis
M_{xy} ..... Edge distributed twisting moment
N_x ..... Edge distributed load in x-direction
N_y ..... Edge distributed load in y-direction
N_{xy} ..... Edge shear load
N^* ..... Critical buckling load
N_{s-a} ..... Semi-analytical edge distributed applied load
N_{num} ..... FE applied load
N_{exp} ..... Experimental test applied load
$[Q]$ ..... Stiffness Matrix
$[R]$ ..... Rotation matrix
R ..... Radius of curvature / gyration
T ..... Touching contact constraint in FE
U ..... Internal strain energy
$u(x,y)$ ..... In-plane displacement field along the x-coordinate of the plate
u_0 ..... Undetermined $u(x,y)$ amplitude coefficient
$v(x,y)$ ..... In-plane displacement field along the y-coordinate of the plate
v_0 ..... Undetermined $v(x,y)$ amplitude coefficient
W ..... Energy exerted by external loads

$w(x,y)$ ..... Out-of-plane displacement field along the z-coordinate of the plate
w_0 ..... Undetermined $w(x,y)$ amplitude coefficient
$\overline{w}(x,y)$ ..... Initial (strain-free) out-of-plane displacement field / imperfection
w_{ini} ..... Known initial displacement amplitude coefficient

Green Notation & Symbols

β ..... Blade (plate) twist angle
β_m ..... Plate's change of twist per meter
γ ..... Shear strain
Δ ..... Determinant of stiffness matrix
ε ..... Normal strain
ε^0 ..... Plate's mid-plane strain
κ ..... Plate curvature
λ ..... Free-edge displacement constant $= 5/12$
μ ..... Poisson Ratio
Π ..... Total Potential Energy
σ ..... Normal stress
τ ..... Shear stress
Ψ ..... Blade (plate) skew angle

Abbreviations

CLPT ..... Classical Laminated Plate Theory
DTU ..... Danmarks Tekniske Universitet / Technical University of Denmark
FEA ..... Finite Element Analysis
IWES Fraunhofer ..... Institute for Wind Energy and Energy System Technology
SSP34m ..... 34m blade developed by SSP Technologies
TTL ..... Trail-to-Leading bending moment
LTT ..... Lead-to-trailing bending moment
TEB01/TEB02/TEB03 ..... Trailing edge buckling experimental specimens 01 / 02 /03
WMC ..... Wind turbine, Materials and Constructions. Hosting company for this research

List of Figures

List of Tables

Chapter 1 – Introduction

Wind turbine blades are highly complex structures as their aerodynamic geometry requires the use of curved composite panels to attain a slender, lightweight profile. Additionally, its components have different material properties depending on the purpose they fulfill, such as uniaxial or biax fiber reinforced composites or the presence of epoxy adhesives to bond components together. As such, blades have to be carefully manufactured, tested and certified to ensure that they will operate successfully throughout their 25 or 30-year operational lifespan. However, there are several factors that may play a role in unexpected early failure of a component, or in the worst case, the entire blade itself. One of these factors is the increased flexibility of the blade. Due to technological advancements within the wind energy market, longer blades are being developed, requiring a more slender and lightweight configuration to reduce the increase in weight. This leads to higher susceptibility to aeroelastic effects [1], which can be loosely defined as the deformation of the structure induced by the airflow. In addition to aeroelastic effects, current manufacturing methods increase the propensity of early failure as having complete control of the manufacturing conditions of the blade's components is difficult. Imperfections from manufacturing appear in the form of uneven bond thickness, dry spots/air bubbles [2], stress concentrations due to uneven pressure during the adhesive curing cycle and even mishandling from the operators.

During its operational lifetime, a wind turbine blade will experience various combined loads, three of which are the edgewise moment, flapwise moment and torsion, illustrated in figures 1.1a, 1.1b and 1.1c.

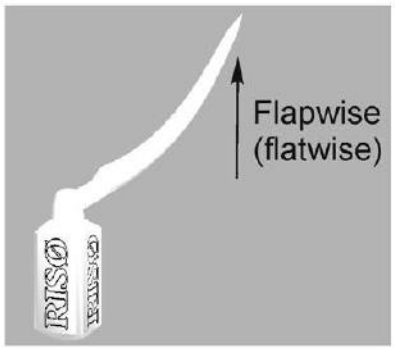

Figure 2.1a - Flapwise bending moment. [3]

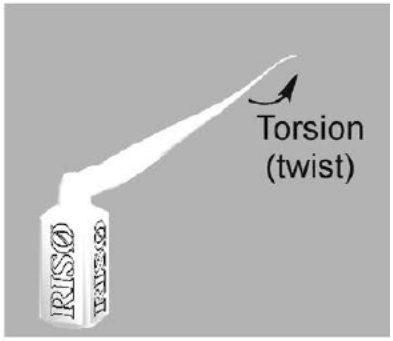

Figure 1.1b - Torsion moment. [3]

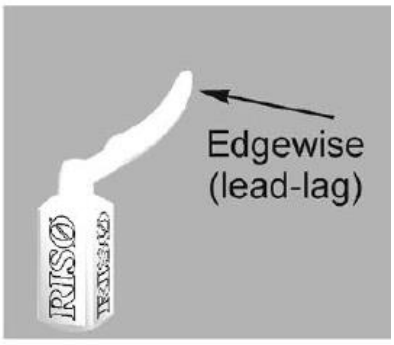

Figure 1.1c - Edgewise bending moment. [3]

Flapwise moment (figure 1.1a), as the name implies, induces bending along the flatness of the blade. Torsion induces a twist along the span of the blade (figure 1.1b). Lastly, the edgewise moment (figure 1.1c) induces a bending along the edges of the blade, either displacing the trailing edge towards the leading edge (Trail-to-Leading or TTL) or the leading edge towards the trailing edge (Lead-to-trailing or LTT).

Due to the low stiffness of the blade in the edgewise direction (compared to flapwise and torsion), the LTT bending moment becomes a driving load which, in some cases, may cause buckling of the trailing edge. Buckling is a type of structural instability that induces large out-of-plane deformations of the structure (figure 1.2a), which commonly results in structural failure due to debonding of the composite panels (figure 1.2b).

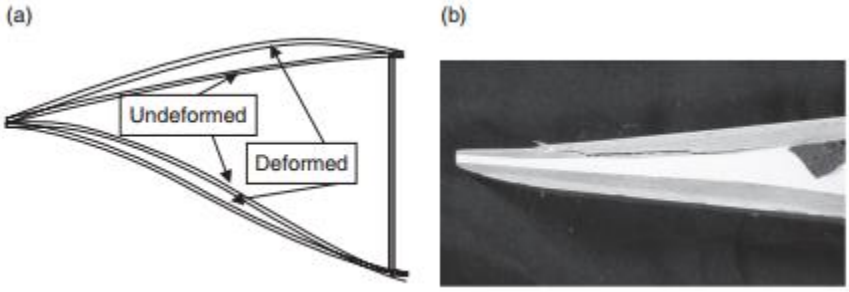

Figure 1.2 -a) Out-of-plane deformations on the trailing edge of the blade due to buckling. b) Cross-sectional view of the debonding of the composite laminates at the trailing edge. Obtained from [4]

This failure mode is a prevalent one in installed and operating wind turbines and it incurs a significant cost to replace and fix the failed blade, as well as costs from downtime. Examples of the failure that trailing edge debonding can cause to wind turbine blades can be observed in figures 1.3a&b.

Figure 1.3 a) Trailing edge debonding of operational wind turbine blade. b) Catastrophic failure of blade induced by trailing edge debonding. Obtained from [5]

To certify that wind turbine blades will be able to operate under normal and certain extreme conditions that they will experience during their lifetime, various tests are done during the design process. These ensure that the likelihood of the event of failure is well understood and minimized. A test pyramid (figure 1.4) is proposed ([6],[7],[8]) comprised of full-scale, sub-component, elements and details and coupon level tests.

1) Full scale tests are used in certification of wind turbine blades at the end of the design process to determine the model uncertainty for the entire blade. These tests are commonly carried out only at the end of the design phase and only a few number of tests are required.
2) Sub-component tests have been recommended by Sørensen et al. [6] for un-scaled sections of the full blade as a means to estimate model uncertainties specific to components or failure modes.
3) Elements & detail tests are generic tests which can be used to check the validity of new concepts, or to test specific combinations or modifications in an easier way than full-scale/sub-component tests and when coupon tests are insufficient [7].
4) Coupon tests are done to obtain specific mechanical properties of materials from statistical data, stemming from a large number of tests carried out.

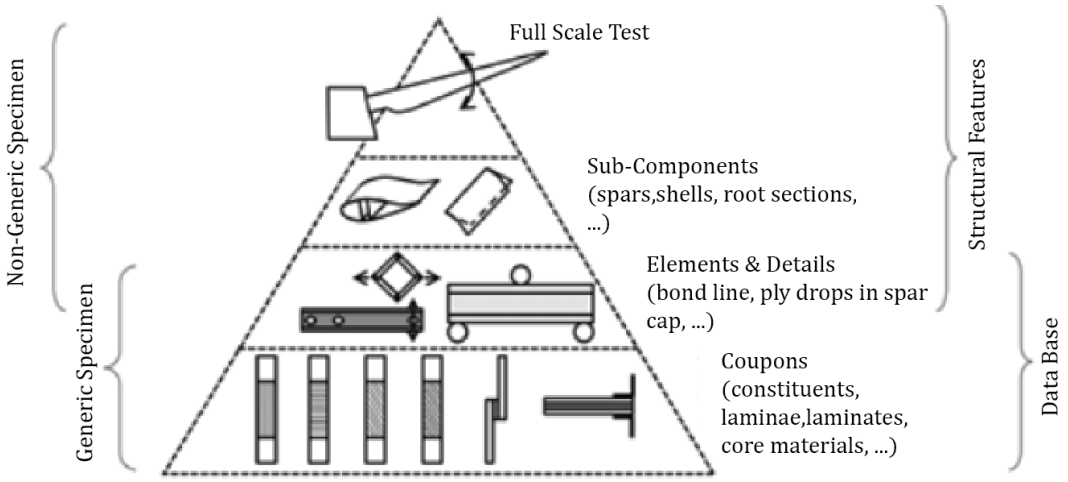

Figure 1.4 – Test pyramid for different scales employed to estimate material properties and load bearing capacity in wind turbine blades. Obtained from [7].

Full scale tests for trailing edge buckling have been carried out extensively, such as those done by DTU ([9],[10],[11]). Coupon tests are also currently being used to study the fracture mechanics of trailing edge adhesive joints, such as those by Eder & Bitsche [2]. Furthermore, sub-component level tests have recently been used for blade certification under the DNVGL-ST-0376 standard [14].

Trailing edge buckling sub-component tests have been designed by Knowledge Center WMC, IWES Fraunhofer and DTU within the IRPWind Research Framework ([12],[13],[14],[15]). Valuable information on the buckling loads and strains through the blade were obtained and comparative results were drawn to full-scale tests. However, tests at this level are quite difficult and expensive to reproduce. The requirement of an already pre-manufactured blade and the costs this incurs leads to a bottleneck for statistical and measurement data. Currently there is a distinct lack of testing at the element and detail level especially regarding trailing edge buckling. Research regarding this test level only led to a broad proposal from IWES Fraunhofer about their application [7].

Therefore, there is a major point of interest within this research project to develop a custom manufacturing test at the element/detail level by manufacturing specimens that resembles a trailing edge bonded joint using commonplace composite and adhesive materials employed in actual wind turbine blades. A custom test set-up will be designed such that a compressive edge moment can be introduced into the structure, leading to an out-of-plane buckling displacement. The set-up will attempt to replicate the desired boundary conditions chosen, ensuring proper joint fixity and obtaining compliant results. Two different modelling methods will be employed as guidelines for the design: A semi-analytical model based on theory of stability of structures and the principle of minimum potential energy, as well as a Finite Element Analysis of the designed test specimen. Several variables are included in the model to account for the geometrical complexity of the trailing edge: blade skew [16], bond length and thickness [17], blade twist [18], [19], and the introduction of the bending moment as a purely compressive load on the trailing edge. These geometric parameters are expected to reduce the load-bearing capacity of the specimen before, during and after buckling and these effects will be quantified. The pre-critical behavior, buckling load and bifurcation load of the plate is studied for varying dimensions and under the effects of the variables above.

Chapter 2 – Literature/Background Studies

In this chapter, the state-of-the-art on trailing edge buckling tests at the full-scale and sub-component level will be presented to illustrate their importance in certifying the structure against operational and limit loads. Next, a general introduction to buckling as a structural instability is given, introducing the principle of minimum potential energy, Lyapunov's theory of stability and the Trefftz criterion. These concepts are presented in a simplified case for derivation of the stability and equilibrium equations of a composite plate, which serves to illustrate the application of the theory. The choice of boundary conditions is presented, which will be employed throughout the research, as well as the concept of effective length to relate the results between clamped and simply-supported structures. As the scope of the study covers a simplified analytical approach, supporting research done previously on analytical plate modelling will be presented, from which concepts and ideas are taken to develop the semi-analytical model. Finally, the objectives and research questions to be explored are given, followed by a general outline that the research will follow.

2.1 State of the art

2.1.1 Operational / Limit Loads of Wind Turbine Blades

Blades are designed to operate effectively without instabilities (such as buckling) by complying with the established design standards. However, in extreme scenarios, such as in high turbulence or at extreme wind speeds, the loads that the wind turbine blade experiences may surpass the expected operational loads. These are limit load conditions in which the blade's components are more prone to failure. Standard IEC-61400-23 [20] proposes a series of Design Load Cases (DLCs) for full scale tests which assess the expected static, dynamic and extreme loads on the wind turbine components. Results from the tested parameters such as stress, strain, strength, fatigue resistance, among others, must be either accurately or conservatively estimated [20]. This provides some degree of confidence that situations leading to failure will not occur. Nevertheless, with the large number of variables that come into play during blade operation, resistance to failure is not always guaranteed.

A recurring failure mode of installed wind turbine blades is debonding of the trailing edge adhesive joint, which may occur when a LTT edgewise bending moment induces buckling of the trailing edge (figure 2.1).

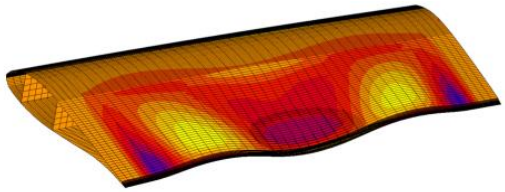

Figure 3.1 - Trailing edge buckling of a wind turbine blade section [21].

A parametric FE study from Branner et al [14] showed that the modelled blade is strongest in the flapwise direction, and weakest in the direction towards the trailing edge (figure 2.2). In general for a wind turbine blade, the spar caps (figure 2.3) provide most of the flapwise stiffness, whereas the box-like structure that the spar caps and shear webs form supply most of the torsional stiffness. Finally, the leading and trailing edge carry the edgewise moments.

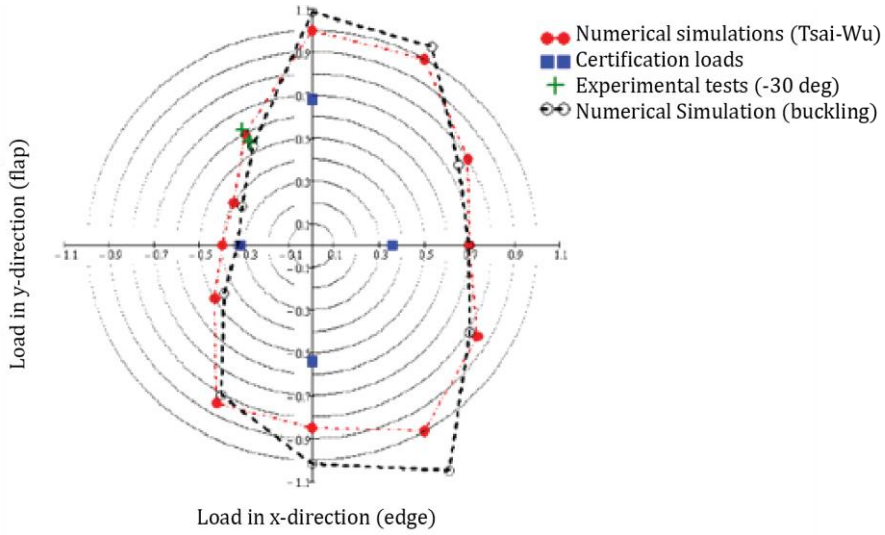

Figure 2.2 - Load carrying capacity of the SSP34m blade based on Tsai-Wu failure criteria and non-linear buckling analysis [14].

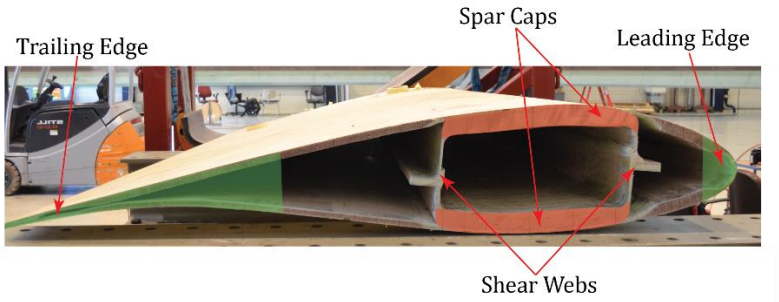

Figure 2.3 - Main load carrying elements of the blade.

As the LTT edgewise bending moment induces compression at the trailing edge and peeling stresses rise at the adhesive, any existing imperfections (such as poorly bonded areas, trapped air bubbles or handling damage, etc) could lead to crack initiation and eventually final failure of the blade [4].

Studies and projects to increase the load bearing capacity of the trailing edge have been done both by academia and the industry; GE - General Electric has patented a few options for the inclusion of high-stiffness trailing edge bonding caps/shells preformed to the aerodynamic shape of the airfoil and manufactured specifically to alleviate the edgewise bending loads [22], [23]. As patented inventions, it is hard to gauge their effectiveness in reducing trailing edge failure, but it can be foreseen that implementing these on a wind turbine blade would drive the manufacturing complexity and as a result the overall costs. In a competitive energy market where up and coming wind power technologies must strive against an already established market especially for non-renewables, reducing the costs of manufacturing labor is at the forefront of the interests for renewable energy companies.

2.1.2 Full Scale Tests

Full-scale tests are highly complex tests carried out a few times (if not only once) at the end of the design process. This test level models the operational conditions with much more certainty and certify that the blade will be able to support the load cases that it will experience, following the IEC-61400-23 standard. DTU carried out a couple of full scale tests of an SSP34m blade under an LTT edgewise bending moment. In their first test from January 2010 [10], the SSP34m blade was truncated at $25m$ and loads were applied in the LTT edgewise direction at 3 points along the span through wire-connected winches (figure 2.4). The deformation of the trailing edge panels was measured using position sensors (LT-ASMs) from the inside of the blade and with NT length transducers from the outside. The deflections measured showed great similarities with the predicted FEM analysis and the measurement provided a good expectation of where failure could occur under an extreme load.

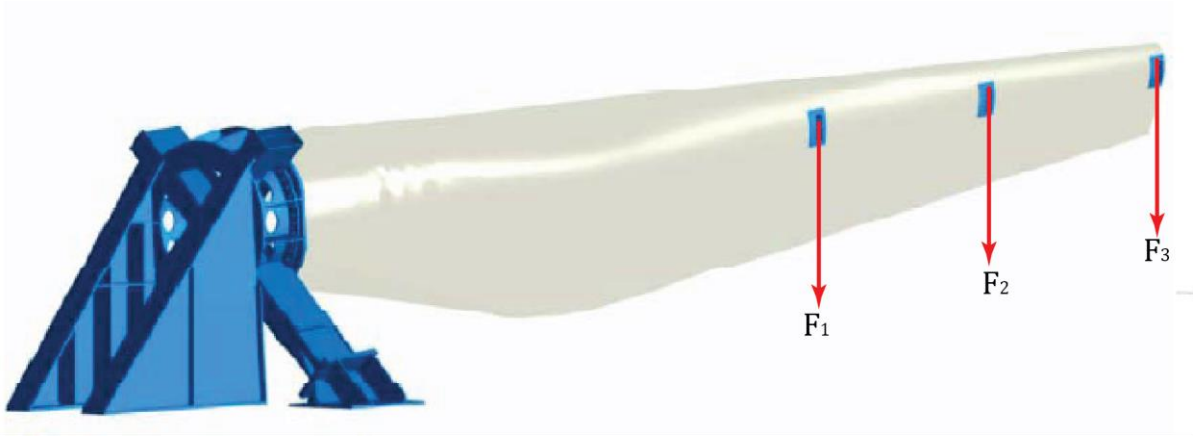

Figure 2.4 - Test right for introduction of edgewise bending moment through 3 winches along the span of the blade up to the 25m cut-off [9.5],[10].

In an attempt to reduce the propensity for the trailing edge of a blade to buckling, the researchers at DTU tested a reinforcement method at the trailing edge of the same SSP34m blade. Coupling between the pressure and suction side panels of the blade was introduced through attachment of 6mm nylon wires [11] (figure 2.5). The test load was applied up to 80% of the certification load. While the reinforcement reduced the amplitude of deflection from the panels, deformation closer to the tip of the blade increased (where there were no more coupling cables). Longitudinal and transverse strains at the line of attachment from the cables appeared to diminish, although minimally.

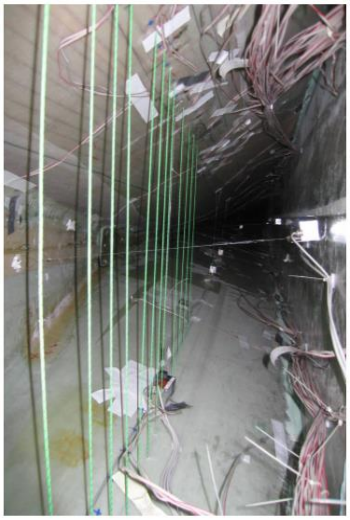

Figure 2.5 - Trailing edge reinforcement test through nylon cable couplings from DTU [11].

2.1.3 Sub-Component Tests (WMC, DTU, IWES)

In the past years, a special focus has been given to the development of mid-level tests for sub-components of wind turbine blades. This level of tests has some advantages over the full-scale level in the sense that more complex loading conditions can be applied, and a larger number of tests can be carried out. This test level also allows for the estimation of model uncertainty in relation to a given failure mode or structural integrity of a component of the blade [4]. Working within the IRPWind research framework, Knowledge Center WMC, IWES Fraunhofer and DTU carried out trailing edge buckling sub-component tests on cross-sectional cut outs of the SSP34m blade. Their respective test set-up had certain differences [12]:

1) Knowledge Center WMC tested a full cross-sectional cut out in a hinged C-Frame rig designed and built at their facilities (Figure 2.6a).
2) DTU also employed a custom C-frame rig, although the cut-out of the blade spanned roughly 75% of the blade's chord (Figure 2.6b).
3) IWES Fraunhofer employed a compression testing machine with off-axis supports at each of the blade's edges. This test also employed a partial cut of the chord length of the blade (Figure 2.6c)

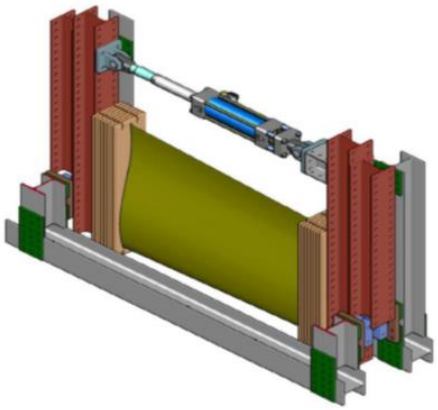

Figure 2.6a) WMC Test

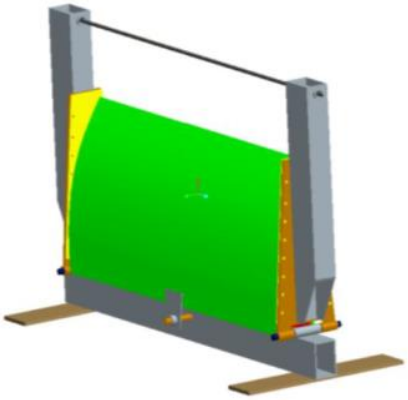

Figure 2.6b) DTU Test

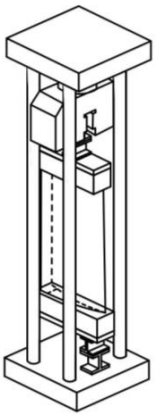

Figure 2.6c) IWES Test

These rigs are equipped with a hinge around the point of the blade's chord where the edgewise buckling moment is zero (roughly at the quarter-chord point from the leading edge) as shown in figure 2.7. This hinge allows a rotation when a compressive load was applied at the actuator located above the trailing edge. This compressive load simulates an LTT edgewise bending moment.

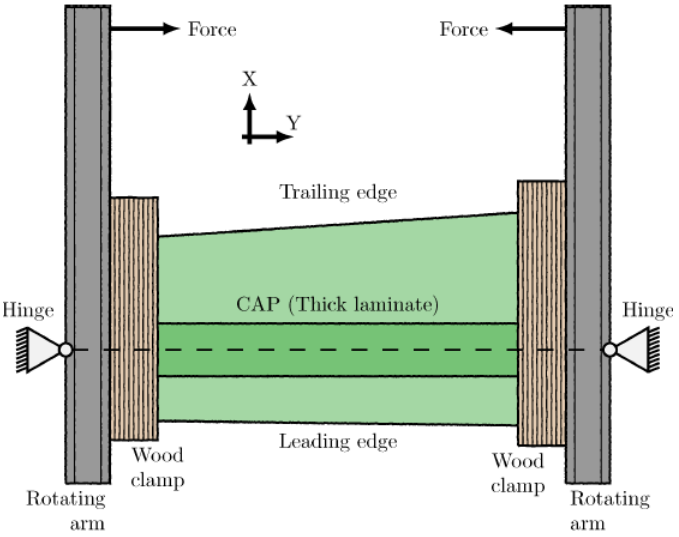

Figure 2.7 - C-frame rig of WMC sub-component test, hinges located at quarter chord of the blade and a compressive load is applied at the top of the rotating arms [21].

Although possessing similar set-ups, the WMC and DTU tests provided slight differences in their outputs. DTU [14] compared the applicability of the sub-component test to a full-scale test which showed the formation of a buckling wave at the $14.5m$ span of the blade. This behavior appeared on the sub-component FE analysis as well. Strains were comparable for both models at lower loads and only differed at higher loads. Failure occurred at 130% of the certification load for the full-scale simulation whereas the sub-component failed between $120 - 125\%$ of said load.

On the other hand, WMC [13],[21] showed the three stages that occurred during testing: pre-buckling, post-buckling and delamination. The differences in apparent edgewise stiffness and buckling displacement amplitudes was illustrated between the pre- and post-buckling stages. Buckling was reached at an edgewise moment of $95\ kNm$, and delamination occurred at $142\ kNm$. This demonstrated that even after buckling, the blade was capable of carrying nearly 1.5x the load. The adhesive failure due to delamination was finally attributed to the large strain fields stemming from the progression of the buckling wave. Another strength that these sub-component tests possess is that they are carried out on full scale blade sectional cut-outs, which include comparable manufacturing and handling defects that operational wind turbines have. This, however, may also be regarded as a limitation if an experimental study is aimed at testing and studying the effects of varying different geometric parameters of the blade. It is for this reason that the element and detail level is considered.

2.1.4 Elements & Details Tests

A trade-off can be made between complexity and accuracy of the test for freedom in variation of certain parameters of the test by shifting the level of the test pyramid to the element and detail level. A test at this level may still be employed for structural elements such as the trailing edge represents, but it is a more generic specimen. Currently and as mentioned by Sørensen et al. [6] only full-scale, sub-component and coupon tests are being carried out for wind turbine blades. There is currently no set standard for tests at the element/detail level. Detail tests can fulfill many purposes [7]:

1) Reduce partial safety factors on larger scale tests such as those required by hygrothermal tests, as these effects can be introduced directly into the test itself.
2) Test new material combinations, concepts, and modifications of existing components that are more easily tested than at a full-scale or sub-component test.
3) Certify the effects of minor details on the blade avoiding the necessity of a full-scale test.
4) Validate numerical models.

Taking these points into account, a custom test is to be designed within this research, for which the test specimen will resemble a trailing edge adhesive joint as much as possible using materials and dimensions employed in actual wind turbine blades. The approach from the sub-component testing rig from WMC and DTU will take a central focus within this research, adopting the C-frame rig they employed in a scaled down version. The test specimen will undergo a compressive load on a clamp hinged system,

such that buckling will occur. Additionally, this custom test will provide the possibility to carry out experiment tests within a wider range of geometric parameters.

Before delving deeper into the specifics of the custom test to be carried out, one vital question must be answered: What exactly is buckling?

2.2 – Equilibrium and Stability: Buckling

When dealing with thin structures undergoing compressive loads, a certain type of structural instability will arise once the compressive load reaches a critical point. Any increment to that already critical load will induce an out-of-flatness motion of the structure. In more technical terms, the critical load is reached when the strain within the structure cannot increase anymore without undergoing large deformations in order to be able to take in additional increments to the compressive load. Buckling of structures typically occurs prior to the ultimate strength of the material, which means that large elastic deformation may take place without failure of the material. Nevertheless, despite the structure not reaching material failure, considerable load-bearing capacity may be lost due to buckling. When dealing with stability/instability of structures and critical points, it is useful to refer to the "ball on a hill" diagram, commonly used in this kind of problems:

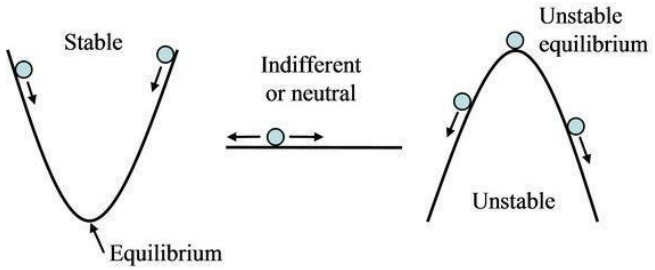

Figure 2.8 - "Ball on a Hill" diagram depicting critical points of stability of a system.

A structure is deemed to be in critical equilibrium when the compressive load that was applied to it is equal to the maximum allowable internal strain energy that it can take up. However, this is not enough to know whether the system is stable, unstable or neutral (otherwise known as asymptotically stable). Imagining equilibrium is depicting the ball at the points of the curves (or line) where it will not undergo motion: at the bottom of the cup, at any point on the straight line or at the top of the hill on figure 2.8 respectively.

It is until a degree of freedom of the system is disturbed that the ball will begin rolling, be it by an additional increase of the compressive load, or a slight out-of-flatness deflection of the thin structure, or

any other perturbation. In the first case, the ball will regain its equilibrium and as such the system is deemed to be stable. If the equilibrium point of the ball is located atop of the hill, it will not regain its equilibrium past the perturbation and will deflect indeterminately, therefore being unstable.

Obtaining the critical points of a system and its stability can be done mathematically with the use of Lyapunov's Theory of Stability and Trefftz criterion.

2.2.1 Lyapunov's Theory of Stability

The stability of plates, which determines how a system will react under an applied load prior and past its critical point (under which buckling occurs), has been thoroughly studied in the past for several loading conditions, from linearly increasing to cyclic loads. Lyapunov's theory of stability establishes that a system can be determined to be in equilibrium by inducing a small increment θ_1 on a degree of freedom of the system, and determining the reaction it will have on the total potential energy Π of the system. Expanding the potential energy into its first, second and third variations induced by the increment on the degree of freedom is done in Equation 2.1. Equating the first variation of the potential energy to zero will determine the pre-critical and post-critical paths [23].

$$\Pi(\theta_0 + \theta_1) = \left.\frac{\partial \Pi}{\partial \theta}\right|_{\theta_0} \theta_1 + \frac{1}{2!}\left.\frac{\partial^2 \Pi}{\partial \theta^2}\right|_{\theta_0} \theta_1^2 + \frac{1}{3!}\left.\frac{\partial^3 \Pi}{\partial \theta^3}\right|_{\theta_0} \theta_1^3 + h.o.t. \tag{2.1}$$

$$\left.\frac{\partial \Pi}{\partial \theta}\right|_{\theta_0} = 0 \rightarrow \begin{cases} \theta_0 = 0 \; \forall \; N \\ N^* \; \forall \; \theta_0 \neq 0 \end{cases} \tag{2.2}$$

Π in Eq. 2.1 is the potential energy of the system established as a Lyapunov function referring to the summation of the internal strain energy and work done by an external load N. This state of equilibrium, determined by the first variation of the potential energy (Eq. 2.2), exists as long as the initial state θ_0 remains equal to zero under a load N. When the load N reaches a critical (bifurcation) point at a load N^* the initial state θ_0 will no longer equal to zero. Figure 2.9 gives a visual representation of the pre-critical and post-critical paths of the system in blue.

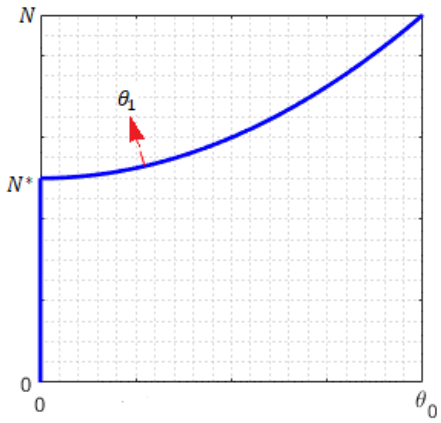

Figure 2.9 - Pre-critical, Post-critical paths and stability of equilibrium from perturbation of a degree of freedom θ_1.

After the critical load N^* is reached, the post-critical equilibrium path may be stable or unstable. Inducing an infinitesimally small increment in a degree of freedom of the system θ_1 can be evaluated on the second variation of the potential energy equation from equation 2.1. The Trefftz criterion states that if the second variation (Eq. 2.3) of the Total Potential Energy is larger than zero at the path of equilibrium, the system will be stable. On the other hand, if the second variation of the TPE is negative, the system will be unstable in its equilibrium and any deviation from the path of equilibrium will cause the structure to collapse.

$$\left.\frac{\partial^2 \Pi}{\partial \theta^2}\right|_{\theta_0} \begin{cases} > 0 \rightarrow stable \\ < 0 \rightarrow unstable \end{cases} \tag{2.3}$$

Knowing the basics for the stability of equilibrium of a system, these concepts will be now applied in a general derivation of the stability equations of a composite plate.

2.2.2 Buckling in Classical Laminated Plate Theory

Classical laminated plate theory (CLPT) can be used to determine the mechanical properties of fiber reinforced composite plate under plane-stress conditions. CLPT can be used to relate the mid-plane strains (ε^0) and curvatures (κ^0) of a plate to the applied moments and normal forces on the edges of the plate as follows:

$$\begin{Bmatrix} N_x \\ N_y \\ N_{xy} \\ M_x \\ M_y \\ M_{xy} \end{Bmatrix} = \begin{bmatrix} A_{11} & A_{12} & A_{16} & B_{11} & B_{12} & B_{16} \\ A_{21} & A_{22} & A_{26} & B_{21} & B_{22} & B_{26} \\ A_{61} & A_{62} & A_{66} & B_{61} & B_{62} & B_{66} \\ B_{11} & B_{12} & B_{16} & D_{11} & D_{12} & D_{16} \\ B_{21} & B_{22} & B_{26} & D_{21} & D_{22} & D_{26} \\ B_{61} & B_{62} & B_{66} & D_{61} & D_{62} & D_{66} \end{bmatrix} \begin{Bmatrix} \varepsilon_x^0 \\ \varepsilon_y^0 \\ \gamma_{xy}^0 \\ \kappa_x^0 \\ \kappa_y^0 \\ \kappa_{xy}^0 \end{Bmatrix} \tag{2.4}$$

The $[ABD]$ matrix is composed of a set of stiffness constants specific to the mechanical properties of the layers of the composite plate, lay-up configuration and fiber-matrix orientations. As this section only illustrated the application of the concepts of stability and equilibrium on a composite plate, the derivation of this matrix will be further explained in chapter 3. Once the plate's $[ABD]$ matrix is determined, the equilibrium and stability equations based on the Lyapunov's theory of stability can be determined considering the plate will undergo large out-of-plane deflections. Using Von Karman strain-displacement relations allows for coupling the in-plane deflections that will occur during the pre-critical loading of a plate and the post-critical out-of-flatness displacements. This will lead to modelling the non-linear behavior of the buckling instability. The Von-Karman strain-displacement relations are given below in equations 2.5a, along with the plate curvatures 2.5b [25]:

$$\varepsilon_x^0 = \frac{\partial u}{\partial x} + \frac{1}{2}\left(\frac{\partial w}{\partial x}\right)^2 \qquad \varepsilon_y^0 = \frac{\partial v}{\partial y} + \frac{1}{2}\left(\frac{\partial w}{\partial y}\right)^2 \qquad \gamma_{xy}^0 = \frac{\partial u}{\partial y} + \frac{\partial v}{\partial x} + \frac{\partial w}{\partial x}\frac{\partial w}{\partial y} \tag{2.5a}$$

$$\kappa_x = -\frac{\partial^2 w}{\partial x^2} \qquad \kappa_y = -\frac{\partial^2 w}{\partial y^2} \qquad \kappa_{xy} = -2\frac{\partial^2 w}{\partial x\, \partial y} \tag{2.5b}$$

The variables $u(x,y)$, $v(x,y)$ and $w(x,y)$ are the in-plane displacement fields along the x-coordinate, y-coordinate and the out-of-flatness displacement along the z-coordinate of the plate respectively. From this point onwards, the out-of-flatness will be referred to as out-of-plane, as the x-coordinate will be aligned with the length of the plate, the y-coordinate as the width and z-coordinate as the plate's thickness.

In a composite plate with a symmetric and balanced ply lay-up, the stretching and shearing reaction of the plate can be decoupled from the bending and twisting, leading to the $[B]$ matrix to be neglected. Additionally, assuming that the plate's orthotropic axes are aligned with the xyz-reference frame axis, the A_{16}, A_{26}, D_{16} and D_{26} terms can also be neglected. The summation of forces in the x and

y-directions can be expressed in the forms given by equations (2.6a & 2.6b), whereas equation 2.6c gives the equilibrium equation in the z-direction for the plate with an applied transverse load N [26].

$$N_{x,x} + N_{xy,y} = A_{11}\left(u_{,x} + \frac{1}{2}w_{,x}^2\right)_{,x} + A_{12}\left(v_{,y} + \frac{1}{2}w_{,y}^2\right)_{,x} + A_{66}\left(u_{,y} + v_{,x} + w_{,x}w_{,y}\right)_{,y} = 0 \qquad (2.6a)$$

$$N_{xy,x} + N_{y,y} = A_{12}\left(u_{,x} + \frac{1}{2}w_{,x}^2\right)_{,y} + A_{22}\left(v_{,y} + \frac{1}{2}w_{,y}^2\right)_{,y} + A_{66}\left(u_{,y} + v_{,x} + w_{,x}w_{,y}\right)_{,x} = 0 \qquad (2.6b)$$

$$\begin{aligned} &D_{11}w_{,xxxx} + 2D_{12}w_{,xxyy} + D_{22}w_{,yyyy} + D_{66}2w_{,xyxy} \\ &\quad - \left(A_{11}\left(u_{,x} + \frac{1}{2}w_{,x}^2\right)w_{,xx} + A_{12}\left(v_{,y} + \frac{1}{2}w_{,y}^2\right)w_{,xx}\right. \\ &\quad + 2A_{66}\left(u_{,y} + v_{,x} + w_{,x}w_{,y}\right)w_{,xy} + A_{12}\left(u_{,x} + \frac{1}{2}w_{,x}\right)w_{,yy} \\ &\quad \left. + A_{22}\left(v_{,y} + \frac{1}{2}w_{,y}^2\right)w_{,yy}\right) = N \end{aligned} \qquad (2.6c)$$

In a buckling problem formulation, during the pre-buckling stage the displacement $w(x, y)$ will still not be apparent, and so equation (2.6c) above disappears. Therefore, the critical buckling load is governed by equations 2.6a and 2.6b.

Using the adjacent-equilibrium criterion allows investigate for further equilibrium configurations for the plate in an already existent state of equilibrium among its displacements u, v and w upon which a small displacement (u_1, v_1, w_1) can be imposed, such that the displacement terms can be substituted by:

$$u = u_0 + u_1 \qquad v = v_0 + v_1 \qquad w = w_0 + w_1 \qquad (2.7)$$

The inclusion of these displacement terms in the equilibrium equations from the scope of the Lyapunov's Theory of Stability would determine that once the equilibrium equations are expanded, the (u_0, v_0, w_0) terms correspond to the state of equilibrium (and therefore zero), and the quadratic and cubic terms of (u_1, v_1, w_1) can be neglected due to being infinitesimally small. The change in internal forces due to the imposed small displacement is given by:

$$N_x = N_{x0} + \Delta N_x \qquad N_y = N_{y0} + \Delta N_y \qquad N_{xy} = N_{xy0} + \Delta N_{xy} \qquad (2.8)$$

The differential terms ΔN represent the increase in internal forces due to the imposed displacement (u_1, v_1, w_1). Expanding N_x yields:

$$N_{x0} + \Delta N_x = A_{11}\left(u_{0,x} + \frac{1}{2}w_{0,x}^2 + u_{1,x} + \frac{1}{2}w_{1,x}^2\right) + A_{12}\left(v_{0,y} + \frac{1}{2}w_{0,y}^2 + v_{1,y} + \frac{1}{2}w_{1,y}^2\right) \tag{2.9}$$

N_y and N_{xy} can be expanded similarly. Taking the first variation of the force equilibrium equations containing the (u_1, v_1, w_1) terms yield a set of equations valid for two plate configurations: a flat one lying on the primary path of equilibrium and a bent plate configuration for the secondary path of equilibrium. While this analysis does not provide insight into the slope or shape of the secondary path of equilibrium, the bifurcation point can be accurately obtained, yielding the critical buckling load.

$$N_{x1,x} + N_{xy1,y} = A_{11}\left(u_{1,x} + \frac{1}{2}w_{1,x}^2\right)_{,x} + A_{12}\left(v_{1,y} + \frac{1}{2}w_{1,y}^2\right)_{,x} + A_{66}\left(u_{1,y} + v_{1,x} + w_{1,x}w_{1,y}\right)_{,y} = 0 \tag{2.10a}$$

$$N_{xy1,x} + N_{y1,y} = A_{12}\left(u_{1,x} + \frac{1}{2}w_{1,x}^2\right)_{,y} + A_{22}\left(v_{1,y} + \frac{1}{2}w_{1,y}^2\right)_{,y} + A_{66}\left(u_{1,y} + v_{1,x} + w_{1,x}w_{1,y}\right)_{,x} = 0 \tag{2.10b}$$

$$D_{11}w_{,xxxx} + 2D_{12}w_{,xxyy} + D_{22}w_{,yyyy} + D_{66}2w_{,xyxy} - \left(N_{x0}w_{,xx} + 2N_{xy0}w_{,xy} + N_{y0}w_{,yy}\right) = 0 \tag{2.10c}$$

Equations (2.10a,b,c) serve as the basis for obtaining the critical buckling loads of the plate in the semi-analytical model and will be further elaborated in chapter 4.2.

2.2.3 Boundary Conditions and Displacement Fields

In plate modelling, selecting the right boundary conditions plays an important role in obtaining accurate results. Boundary conditions are constraints (or lack thereof) at points throughout the plate that specify the allowable displacements, rotations, or reactionary forces and moments. Boundary conditions that satisfy specified displacements and rotations are commonly known as geometric or essential boundary conditions. On the other hand, boundary conditions satisfying forces and moments are known as natural boundary conditions.

The two most commonly used essential boundary conditions in plate modelling are clamped and simply supported. When these boundary conditions are imposed on a random displacement $\phi(x)$ in a

system, this displacement must satisfy the constraints imposed by each condition: A simply supported boundary (S) must prevent displacement ($\phi(x) = 0$) from happening at the specified coordinates, while rotations may still happen. On the other hand, a clamped boundary condition (C) prevents both displacement and rotation ($\phi(x) = 0 \ \& \ \phi'(x) = 0$) from happening at the clamped point.

To visualize these boundary conditions, the case of a bar of length $a = 2\ m$ clamped on one end at the point $x = 0$ and simply supported at the opposite end $x = a$ is shown in figure 2.10.

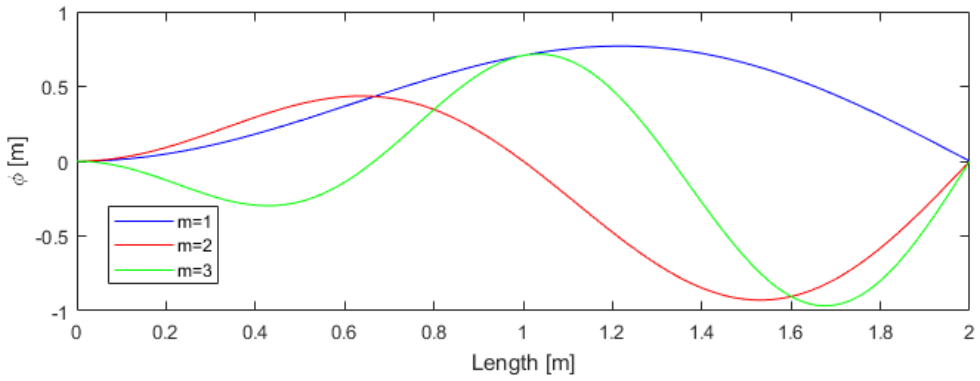

Figure 2.10 - Clamped-Simply Supported bar and possible displacements.

The displacement field may take several different shapes, known as modes and shown for the different values of m in figure 2.10. These modes will be determined by factors such as the bending stiffness of the bar and its dimensions. A solution to the displacement field for the clamped-simply supported bar may be given by equation 2.11, where ϕ_0 is an undetermined deflection amplitude coefficient, and m is a variable displacement mode, or in other words, the number of half-sine waves that the displacement adopts:

$$\phi(x) = \phi_0 \sin\left(\frac{\pi x}{2a}\right) \sin\left(\frac{m\pi x}{a}\right) \tag{2.11}$$

A boundary condition that is not employed as commonly as simple supports or clamps is a free edge. This condition is much more problem-specific. Visualizing the same 2-meter bar being clamped at the end where $x = 0$ and free at $x = a$ (figure 2.11), one may expect the deflection to occur as depicted roughly by either of the shown lines given by the solution for the displacement in equation 2.12:

$$\phi(x) = \phi_0 \sin^2\left(\frac{\lambda\pi x}{a}\right) \tag{2.12}$$

Where λ is a value that will determine the displacement at the free edge $x = a$. While one may expect the blue line ($\lambda = \frac{1}{2}$) as an acceptable value for the solution, it must be noted that this value

represents a rotation equal to zero ($\phi'(a) = 0$) which is a solution particular to a clamped boundary. Furthermore, a clamp at the boundary would induce a reactionary moment at such location; as a free-edge there is no supporting constraint to allow this reactionary moment and therefore the value of $\lambda = \frac{1}{2}$ would not be acceptable. Barbero [27] worked out the exact solution for the buckling of a plate with a free-edge, which yielded very similar results for a value of $\lambda = \frac{5}{12}$ (red line).

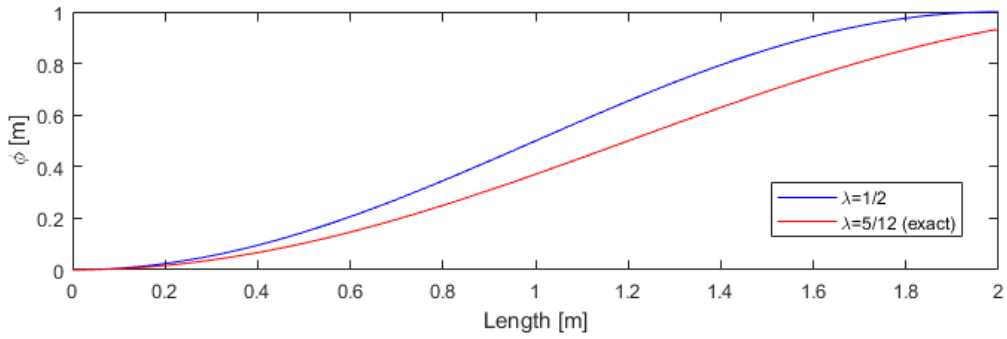

Figure 2.11 - Clamped-Free bar for approximated and exact solution.

One final type of constraint that will be used within this research is a sliding edge constraint. This constraint may retain the clamped or simply supported requirements for the displacement field, whilst allowing for shortening of the structure (in-plane motion). Figure 2.12 shows a clamped-clamped bar with non-sliding edges (blue) and a clamped-clamped bar where both ends are allowed to slide horizontally (red):

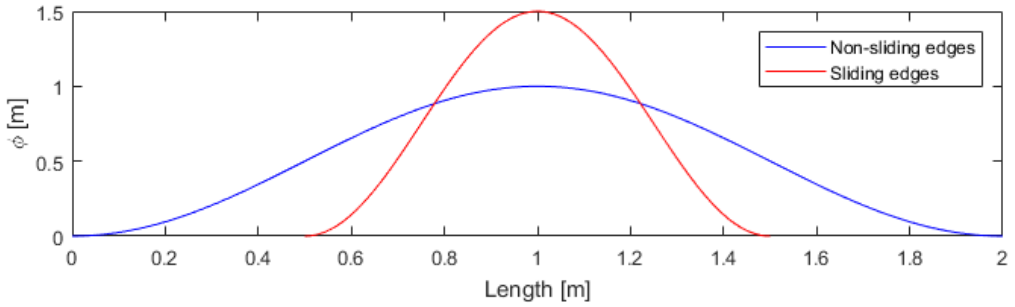

Figure 2.12 - Sliding boundary conditions of a bar where vertical $\phi(x)$ and horizontal $\xi(x)$ displacements show interdependency.

For a bar with sliding boundary conditions, a single vertical displacement function $\phi(x)$ will no longer suffice, and a secondary horizontal (in-plane) displacement field $\xi(x)$ must be specified such that new conditions are met:

$$\xi(0) \neq 0 \qquad\qquad \xi(a) \neq 0$$

A general solution to the in-plane displacement boundary conditions may be given by equation 2.13:

$$\xi(x) = \xi_0 \cos\left(\frac{\pi x}{a}\right) \tag{2.13}$$

Buckling problems that employ the Von Karman relations for large displacements possess coupling between the in-plane and out-of-plane displacements. For that reason care must be taken when specifying the solutions for these coupled displacement fields. However, before attempting to define the plate model within this research and imposing the necessary boundary conditions on it, one last concept used in the buckling of structures will be presented.

2.2.4 Effective Length

Effective length is a concept used to interrelate the constraining effects from clamped boundary conditions of a structural element of length a under compression to an equivalent, but simply supported element of length Ka, where K is a factor dependent on the established boundary conditions at each end [28].

While accurate implementation of boundary conditions in partial differential equation problems (such as the analytical solution in this research) is possible and, more often than not, required, a common approach used to simplify the formulation is through application of the effective length concept. In fact, early solutions to the coupled-displacement plate analysis within this research demonstrated a highly convoluted formulation for the desired clamped boundary conditions which will be explained section 3.3. Instead, the effective length of simply-supported boundaries will be applied.

Simply supported ends of a structure have, by definition, zero-reactionary moment and therefore the resistance to lateral deflection depends entirely on its bending stiffness. On the other hand, clamped ends that counteract the rotations at their locations would lead to a buckled shape that spans a shorter, and therefore, effective length. Figures 2.13a) and 2.13b) illustrate this:

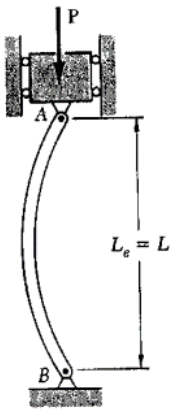

Figure 2.13a) Simply supported beam at both ends with an effective length L. Obtained from [29].

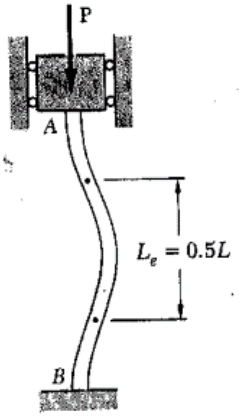

Figure 2.13b) Clamped beam at both ends with an effective length 0.5L. Obtained from [29].

Different factors K that relate the effective column length to the pinned (simply-supported), moment-free ends have been derived theoretically and are presented in Table 2.1 below. These theoretical values are oftentimes not directly applicable in experimentation, as end-fixity is an idealized condition that is rarely fulfilled entirely. Slight rotations may still happen leading to the obtention of slightly higher effective length coefficients K.

B.C.s	**a) C-C**	**b) C-S**	**c) C-T**	**d) S-S**	**e) C-F**	**f) S-T**
		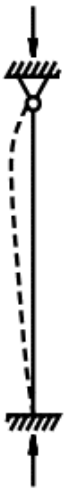	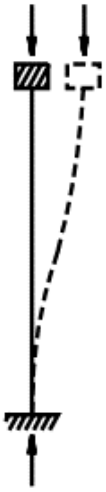	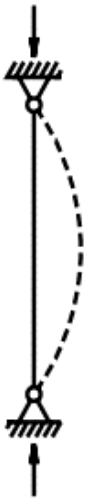	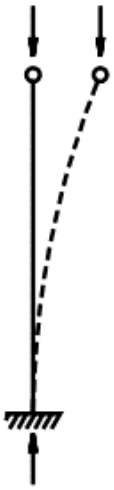	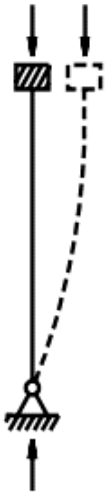
Theoretical K	0.5	0.7	1.0	1.0	2.0	2.0
Recommended K	0.65	0.8	1.2	1.0	2.1	2.0

Table 2.1 – End boundary conditions C (clamped), S (simply supported), T (Translating) and F (free) combinations, theoretical and recommended effective length coefficients K. Obtained from [28]

It is important to note that an additional boundary condition is proposed in Table 2.1 in cases c) and f). A translating boundary is one that allows displacement at the constraint coordinates but restricts rotations. In order to remain consistent with the free-end conditions established by the λ value proposed

by Kassapoglou [25] where the rotation and moment at the free-edge have nearly disappeared, case c) of Table 2.1 will be employed for clamped-free conditions.

2.3 Supporting Plate Modelling Research.

Plate theory has been widely used to model a variety of flat and shell structures under different loading and boundary conditions and there is abundant literature from which this project can draw upon to model the trailing edge as a standalone specimen. While some specific approaches to the formulations of these models are useful and will be adopted within this research, to the author's best knowledge, there are no analytical models specifically tailored to the study of a wind turbine blade's trailing edge.

Helms et al [17] propose a taper-taper adhesive bonded composite joint where the taper angle θ is given with respect to the composite plate's surface. Their findings show that for a taper angle of 0°, corresponding to a sandwich structure with the bond acting as core, the critical buckling load decreases considerably, and it increases substantially for higher angles.

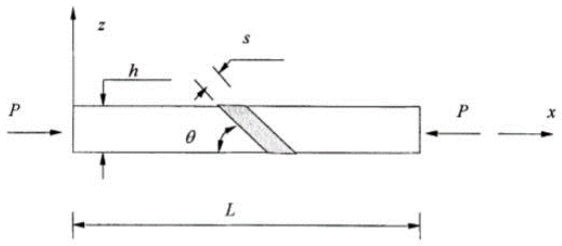

Figure 2.14 – Taper-taper adhesive joint as given by Helms et al [17].

On the other hand, due to the fact that adhesives possess smaller stiffness modulus than the adhered composite panels, reducing the adhesive's thickness will increase the buckling load of the joint. It is unclear whether partially bonded composite plates (such as the trailing edge section of the blade) will be affected largely by the presence of the adhesive in increasing buckling loads.

Kim & Kwon [30] developed a model for the buckling of generic one-edge-free plate problems. The boundary and loading conditions employed are similar to those within this study, the only difference being the constraints at $x = 0$ and $x = a$ in which in-plane motion was prevented. As such, their formulation did not make use of Von Karman large deflection relations. Instead, their solution depended on the use of displacement fields represented as a summation of functions that comply with the essential boundary conditions (equation 2.15):

$$w(x,y) = \sum_{1}^{m} \sum_{1}^{n} f_w(mx)\, f_w(ny) \tag{2.15}$$

Using a one-term solution in their analysis yielded highly accurate results for a clamped-clamped/simply supported-free plate in comparison to a two-term solution. Therefore, one term displacement fields will suffice within this research.

Skewed plates showed large reductions of load-bearing capacity in the works of Daripa & Singha [16]. Their buckling and post-buckling experimental tests showed that skew and wavering inclined edges reduce the critical buckling load by around 25% for a $\Psi = 15°$ and 38% for $\Psi = 30°$. While the expected skew angle in wind turbine blades is not expected to reach such high degrees, it is interesting to determine the effect this could have in trailing edge buckling. Additionally, in their research, a method to implement initial imperfections was found. An initial imperfection can be considered as a pre-existing out-of-flatness of the plate such as that which the twist angle induces. This imperfection is included as a strain-free initial deflection $\overline{w}(x, y)$ which, as the name implies, does not affect the internal strain energy terms of the total potential energy equation. On the contrary, it is only prescribed on the terms related to the energy exerted by the external loads. This point is adopted within this research.

Jensen et al [31] developed an extended buckling and post-buckling analytical model that applies Von Karman's strain-displacement relations to show the reduction of the buckling loads due to coupling in the elastic behavior. Their formulation allowed to separate the coupling due to asymmetric and unbalanced plates within the linear and non-linear analyses which was adopted within this project during the derivation of the stability and equilibrium equations in given in chapter 3.4 and the integrations from appendix C.

2.4 Research Questions and Objectives

Objectives in research for this project will be given covering the three main sections: Semi-analytical modelling, numerical analysis and the experimental set-up and testing. The central focus of these objectives will be to provide guidelines on developing a custom element/detail test of a trailing edge adhesive joint that encompasses several geometric factors. For sections in the research that do not provide the desired/expected results, suggestions for improvement and justifications are sought such that a future iteration of the research will have additional tools and information.

Objective 1: *Apply relevant theory in stability of structures (Lyapunov's theory of stability, Rayleigh-Ritz) into developing a semi-analytical model of plate buckling under specified conditions that reflect a (simplified) wind turbine trailing edge. The results obtained from the semi-analytical model should remain compliant with those from FE modelling and Experimental testing.*

Question 1: How can a SSP34m wind turbine blade be simplified in its geometry and boundary conditions into a semi-analytical plate model? How can the implementation of these parameters be improved in future research to develop an element/detail test for trailing edge buckling?

Subquestion 1.1: What is the expected effect of the blade skew Ψ and twist β in reducing the critical buckling load if modelled as a modified initial geometry or an initial imperfection, respectively?

Subquestion 1.2. How can one quantify the effects in reduction of load-bearing capacity of the plate to provide a straight forward comparison with the numerical and experimental sections?

Subquestion 1.3: What are the limitations of the applied concepts and methods (effective length, one-term solution from displacement fields, initial imperfection modelling) in the accuracy of the results for the semi-analytical model? Can any suggestions be provided to elaborate and improve those areas?

Subquestion 1.4: In regards of the concept of effective length on simply supported boundaries, do the results show agreement within an acceptable range to those of FE analysis with clamped boundaries?

Objective 2: *Provide results from a reliable FE model to work as the link between the semi-analytical and experimental results that account for the desired loading and boundary conditions and variation of geometric parameters to be compared.*

Question 2: What parameters and within what range is it possible to analyze numerically the plate models such that a comparison can be drawn to both the semi-analytical solution and experimental results?

Subquestion 2.1: What is the best way to ensure a proper load introduction into the MSC Marc plate model to simulate a compressive edgewise moment? What approach must be taken to include the hinged corners of the clamp?

Subquestion 2.2: How must the interaction between the elements of the plate model (clamps, composite panels, adhesive) be included to better ensure the analysis will yield comparable results with the experimental test during pre-buckling and post-buckling?

Subquestion 2.3: Are the results from varying the geometric parameters comparable to the semi-analytical solutions?

Objective 3: *Present the experimental results from the custom designed test in comparison to the semi-analytical and numerical results in order to demonstrate that the test fulfilled its purpose. Provide guidelines and suggestions for improvements to the aspects of the set-up that did not perform as desired.*

Question 3: Does the custom experimental clamping system and specimens have the versatility to be employed on testing the multiple parameters included in this research? Can it be used to test for variations in materials, quality and imperfections?

Subquestion 3.1: Did the custom clamping system fulfill the desired boundary constraints or did problems arise regarding joint fixity?

Subquestion 3.2. Did the experimental test yield the expected buckling loads, shapes and strains expected from the semi-analytical and numerical tests? What aspects must be addressed for improvements?

Subquestion 3.2: How can the custom clamping system be improved to allocate and test a coupon that better resembles a wind turbine's trailing edge?

2.5 Project Outline

The background and literature supporting the research project has established the methods, objectives and results from previous trailing edge buckling studies at WMC and DTU. These topics will work as the basis upon which the remainder of the research is done. Firstly, Chapter 3 will present the geometry of the reference wind turbine blade in the previous trailing edge tests (SSP34m), explaining certain parameters such as chord distribution and blade twist. The effect of these parameters on buckling will be included within the research. Next, an approach will be proposed to simplify a section of the blade into a custom specimen, comprised of two composite panels bonded at one edge. The most optimal boundary conditions for each method (semi-analytical, numerical and experimental) will be chosen for the plate's edges.

A semi-analytical model derivation is proposed in Chapter 4 to determine the buckling loads of the plate under a variety of geometric dimensions, as well as the effect of the initial imperfections. A solution for the stability problem will be given in the form of an eigenvalue problem with coupled in-plane/out-of-plane displacements. A preliminary comparison between the results of a fully bonded plate and debonded composite plates is given.

Chapter 5 explains the process to manufacture the test specimens and the custom hinged clamp system. The set-up is designed to be able to induce buckling at the trailing edge adhesive joint. The main objective is to define the accuracy and applicability of this custom trailing edge coupon test at an element/detail level by ensuring proper boundary constraints (joint fixity), strain gauge placement and mounting the system into a $100\ kN$ compression machine. The results from this section are filtered and aligned to have them ready for comparison with the semi-analytical and numerical methods.

Chapter 6 will focus on modelling the experimental set-up in a Finite Element Analysis program (MSC Marc Mentat). In this chapter, a mesh-sensitivity analysis is carried out to show the convergence of the results for the chosen mesh refinement. The chosen mesh is then implemented in a variety of FE models which include variations in the chosen parameters:

-Plate length a / width b -Chord distribution (Skew Ψ) -Initial imperfections $\overline{w}(x, y)$

Chapter 7 will present the results obtain from the three methods used, which will serve to validate (or disprove) the applicability of the concepts and methods used. The buckling loads obtained from the semi-analytical model will be compared with the FE results. Effects of initial imperfections will also be compared for both methods. Next, the results of the FE models and the experimental tests will be compared to show (or disprove) the capability of the custom test set-up to keep the desired constraints throughout the entire test. Chapter 8 will discuss the strengths and weaknesses of the scientific approach of the project, and suggestions for improvements will be given. This research is expected to serve as the first iteration in the design of a trailing edge adhesive joint coupon experiment at the element and detail test level.

Chapter 3 – Plate Modelling

This chapter will begin by showing the reference SSP34m blade. The geometry will be explained, specifying the parameters which will be included in the modelling of the test specimen. A section of the blade will be then simplified into a bonded composite plate that will undergo a compressive edge load simulating an edgewise bending moment. The constraints on the plate's edges will be shown in a schematic that will be recurrent throughout the following chapters of the project. This is done to illustrate the correlation between the semi-analytical model, numerical (FE) and experimental set-up such that the reader can understand better the comparisons drawn from the results in Chapter 7.

The semi-analytical model is done with simple-supports, and in order to bridge the gap to clamped constraints, the effective length concept is employed. The experimental set-up is designed to have clamped boundaries that allow for controlled behavior of the experiment in aspects such as load introduction as a bending moment and joint fixity. Finally, the freedom that FE analysis brings allows to model both simple supports and clamps, and the results from these FE models will be used respectively to validate the semi-analytical model and to draw a comparison with the experimental clamped system.

3.1 Blade Geometry of SSP34m blade

The trailing edge buckling tests carried out at WMC and DTU were done on a section cut-out of the SSP34m blade. A 3-dimensional view of this cut-out is given in figure 3.1 on the right, where some prominent geometrical parameters are shown: blade skew Ψ, blade twist β, section width a and adhesive length b_l. To understand the implementation of these geometrical parameters in the model, they are further explained within this section using the actual geometry from the SSP34m blade.

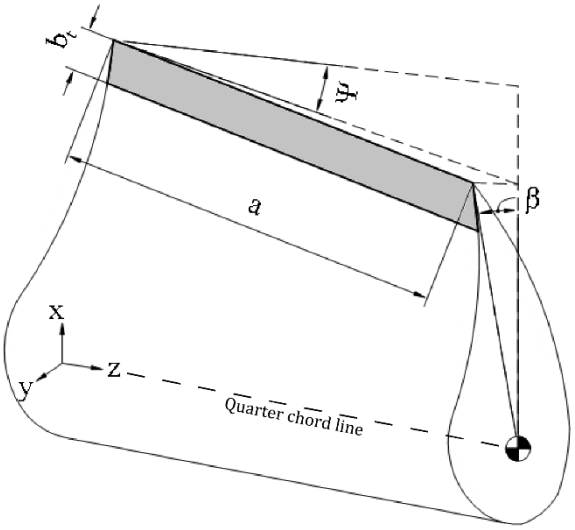

Figure 3.1 - 3D view of a wind turbine blade test cut-out and relevant parameters.

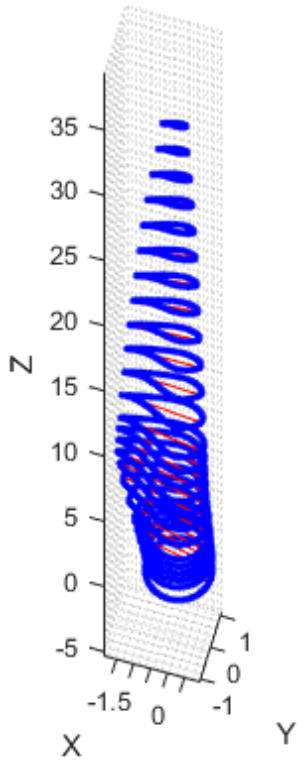

Figure 3.2 - SSP34m airfoil data points 3D plot.

A finite element model building tool for the SSP34m blade from which the blade geometry could be extracted was provided by Philipp Haselbach (supervisor). From the file, the xyz-coordinates of 25 airfoils were obtained. In the blade's frame of reference, the x-axis corresponds to the length (chord-wise), y-axis to the blade's thickness and z-axis to the blade span. Plotting these provided the approximate shape of the blade as seen in figure 3.2. From these airfoil coordinates, the trailing and leading-edge points were discernible and the distance between them provided the chord length at every airfoil position. Appendix B shows the blade's top and edge view, which correspond to the chord lengths and blade thickness respectively. Aligning the chord lengths in a chord-distribution plot (figure 3.3) yields insight into the skew Ψ, one of the geometric parameters to be included within the scope of this study.

Skew is essentially the angle of the trailing edge of the blade due to the tapering chord length along the blade span with relation to the blade's z-axis (figure 3.3a). The immediate skew angle at every point along the blade is shown in figure 3.3b, obtained from equation 3.1, where c_i and c_{i+1} are the chord lengths at spans z_i and z_{i+1} respectively. The minimum value of the twist is found to be $3.6°$ at around $15\ m$ span, increasing up to $6.6°$ near the tip.

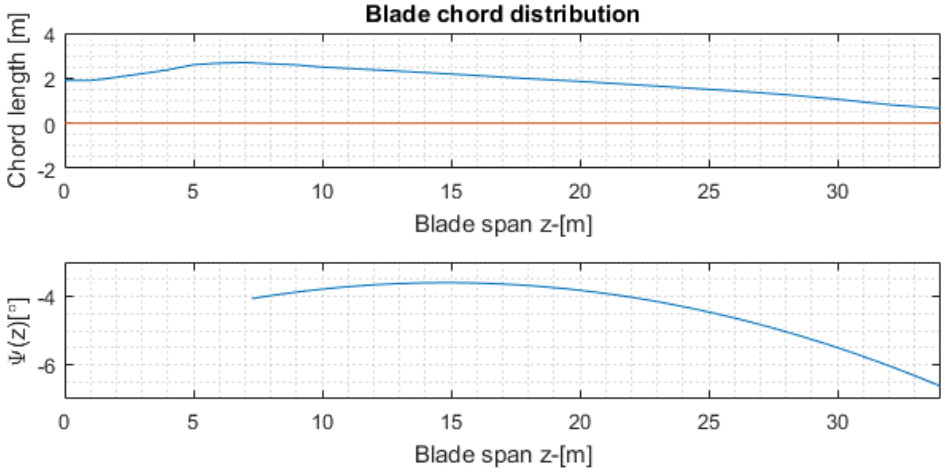

Figure 3.3 Top a) Chord length distribution along the blade span. Bottom b) Skew angle along the blade span.

$$\Psi(z) = \tan^{-1}\left(\frac{c_{i+1} - c_i}{z_{i+1} - z_i}\right) \tag{3.1}$$

From the leading edge and trailing edge points of the blade, the twist β of the blade can also be obtained. Twist in a blade typically happens around the quarter-chord point (figure 3.1). A simple trigonometric relation from the chord lengths, leading and trailing edge coordinates yielded the twist at all 25 span positions observable in figure 3.4a) displayed as crosses.

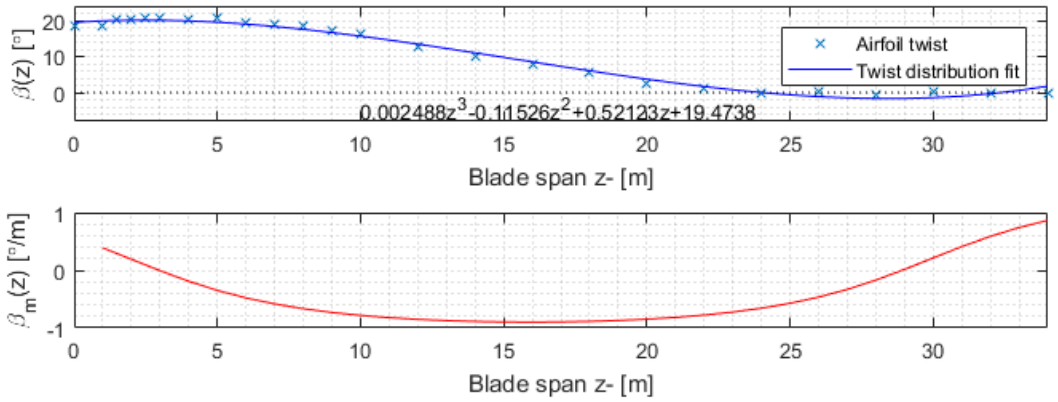

Figure 3.4 – Top a) Blade twist at airfoil locations along the span. Bottom b) Rate of change of slope at a given location along the blade span.

Blade twist is defined as the angle of rotation around the z-axis of the blade, centered at the quarter-chord point. The blade root is taken as the point of reference where $\beta(0) = 0$. In the plates to be considered within this research and as will be explained following in this section, the point of reference will not be the root but a random point along the span of the blade. Furthermore, plates with varying length (and therefore twist) will be discussed. Therefore, the twist distribution is given in a normalized form (rate-of-change or twist per meter β_m). In this manner, the maximum immediate twist change of the blade is found to be $-0.8965°/m$ at $15\ m$ along the span (figure 3.4b), which can easily be evaluated for plates with varying lengths.

In addition, a close look is taken at the trailing edge adhesive joint for its dimensioning within the experimental coupons. From a rough visual approximation in figures 3.5 and 3.6, the bond length b_l is taken as 5% of the local chord. Additionally, the bond thickness b_t and plate thickness h are taken from the WMC report [13]. The thickness of the biax facesheets fs_t is also included as a constant in the model.

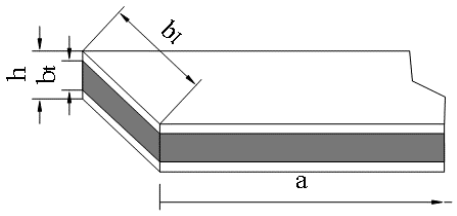

Figure 3.5 - Adhesive line dimensioning.

Figure 3.6 - Adhesive line in a wind turbine blade cross-sectional view.

3.1.1 Simplification into bonded plate

Figure 3.7 shows a cross-sectional cut-out section of the SSP34m blade. The general positioning of the aft and fore shear webs of the blade is shown; the aft shear web serves as a convenient delimitation for the plate model since, along with the spar caps, it provides much of the blade's flapwise stiffness. The area where the shear webs are positioned does not typically buckle under the same loading conditions that cause trailing edge buckling. Choosing the aft shear web as the constraint opposite to the trailing edge also allows idealizing the plate as a skewed rectangle, as opposed to having a trapezoid which would increase the complexity in modelling significantly. Additionally, it is important to mention that the blade's coordinate system (x-chordwise, y-thickness-wise & z-spanwise) will no longer be used. Instead, the cut-out x-coordinate will be aligned with the length (a dimension), y-coordinate along the width (b dimension) and z-coordinate perpendicular to the page.

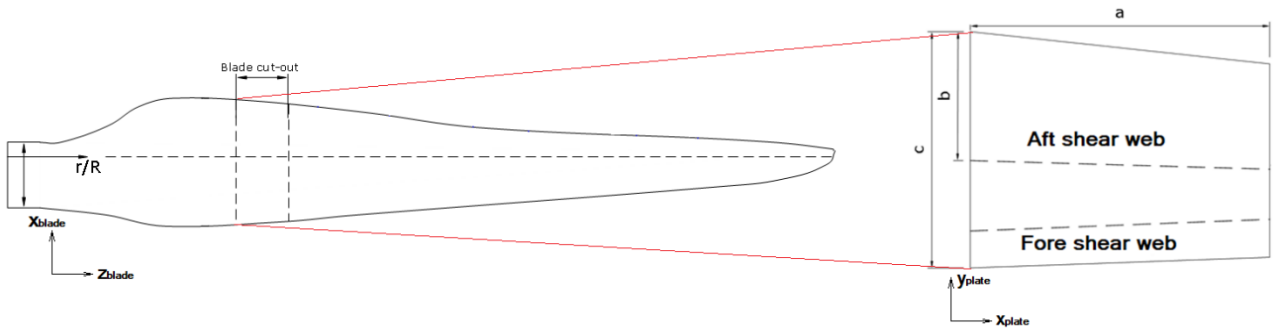

Figure 3.7 – Blade cut-out chosen at random blade span seen as a stand-alone section with length a, chord c and distance from aft shear web to trailing edge b.

The plate's edges are now chosen such that they are compliant with the experimental test from the C-frame test set-ups from WMC and DTU: Under an edgewise bending moment, the short side edges will experience a compressive load along the x-coordinate of the plate. These loaded edges are allowed

rotation around the bottom corners (figure 3.8), permitting an in-plane displacement to take place increasing towards the trailing edge. On the other hand, the bottom edge will not be allowed to displace in the x-y plane, while the top (free) edge does not possess any constraints whatsoever. A figure of these general constrains can be seen below in figure 3.8 and of the cross-sectional view in figure 3.9.

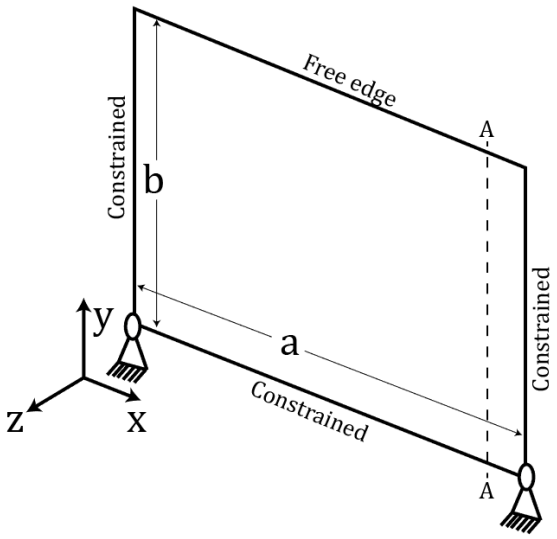

Figure 3.8 - Plate model shape and boundary constraints, along with chosen frame of reference.

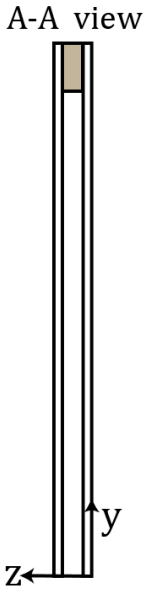

Figure 3.9 - Cross sectional view of the plate model including bondline.

Whether these constraints are simple-supports or clamps will depend on the modelling approach or test set-up, explained in the following subsection.

3.2 Boundary Conditions

The boundary conditions for each method used in the research are presented in the following subsections, explaining the decision making behind the choices. The figures presented for each method will be reiterated in the respective chapter of the method employed and will help illustrate the correlation of the results in order to draw a clear comparison between them.

3.2.1 Semi-Analytical Model

The semi-analytical model derivation that will be given in the following chapter was done initially using simply-supported boundary conditions for all three constrained edges of the plate (figure 3.10a). Simple supports yielded a straightforward process for an already convoluted derivation, which was the main reason for this decision. In order to approximate the solution for the clamped edges, the concept of effective length was used instead, which required the inclusion of two length correction factors K_a and K_b for the plate's length a and width b respectively. From table 2.1 case a), an effective length factor for

the length a of the plate can be chosen as $K_a = 0.5$ which reduces the effective length of the plate as shown in figure 3.10b. The correction factor for the plate's width b is retrieved from case c) of table 2.1 as it best represents the free-edge displacement due to the factor λ discussed previously. In this case, the correction factor $K_b = 1.0$ was calculated and would therefore remain unaffected. However, the recommended correction factors, $K_a = 0.65$ and $K_b = 1.2$, are implemented.

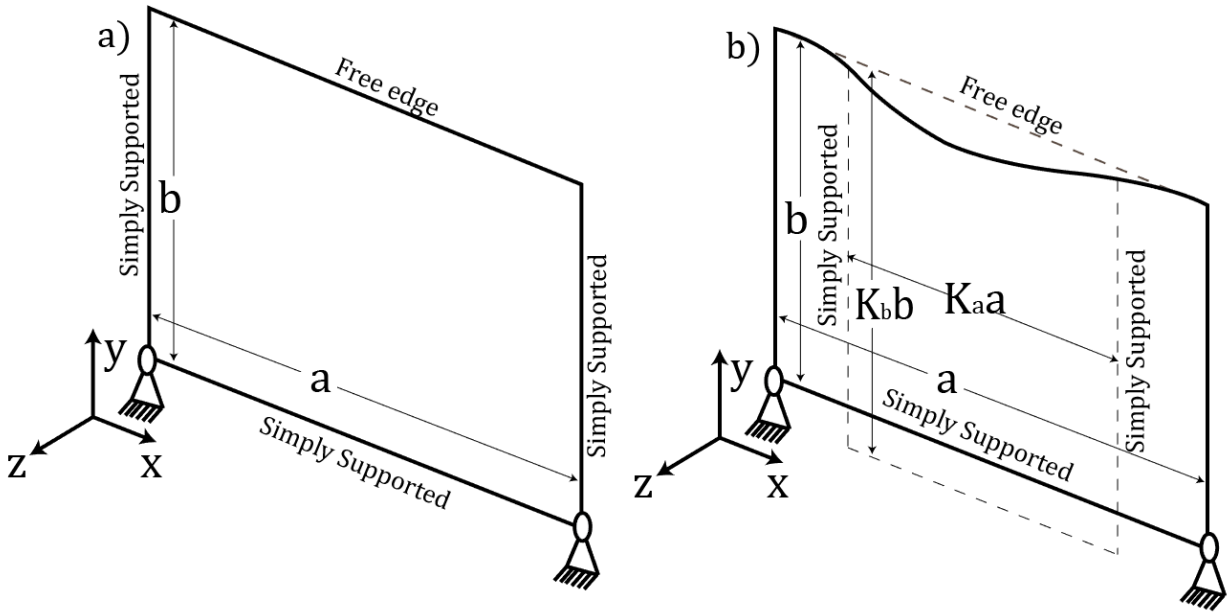

Figure 4.10a) Simply supported boundary conditions for semi-analytical model. b) Effective length correction factors $K_a = 0.65$ and $K_b = 1.2$ according to [28].

3.2.2 Experimental Set-Up

During experimentation, applying the desired boundary conditions is a challenge due to the issue of joint fixity. In this research, clamped boundary conditions (figure 3.11) are chosen for the following reasons: the loaded edges must be clamped in order to distribute the loading stresses and prevent local crushing of the corners where the load is applied. The clamps will also help introduce the compressive load as a distributed edgewise bending moment. The design process of the clamping system will be explained in Chapter 5.

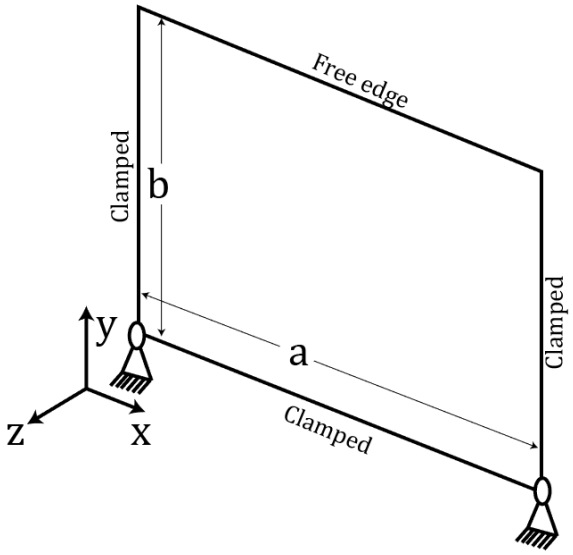

Figure 3.11 - Clamped boundary conditions for the experimental set-up. The clamping system will be designed in Chapter 5.

The designed clamping system may not entirely fulfill the clamped constraints in their entirety, allowing slight out-of-plane displacements or rotations at the edges which will affect the results. These results will be compared to finite element models where boundary conditions can be applied in their totality without joint-fixity issues to determine the degree of joint fixity that the clamping system reached.

3.2.3 Numerical Model

The flexibility that FE Analysis programs gives in regards of applying and modifying boundary conditions straightforwardly gives the possibility to use the models as a bridge between the two other methods employed.

Firstly, applying simply supported boundary conditions to the FE models (figure 3.12a) allows to draw a straight comparison with the semi-analytical model and validate its results. Next, the boundary conditions of the FE models will be changed to clamped (figure 3.12b). This will serve two purposes: Compare and validate the results of the application of the effective length correction factors from the semi-analytical model, and to demonstrate the degree of joint-fixity reached by the experimental clamp system.

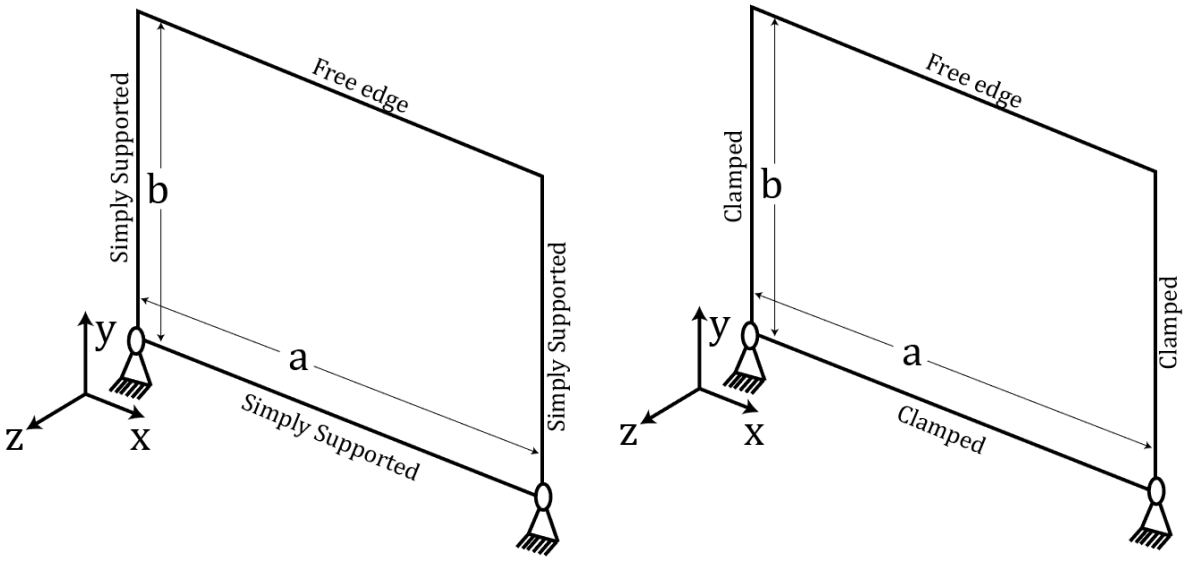

Figure 3.12a) Simply supported boundary conditions of FE models to compare and validate semi-analytical results. b) Clamped boundary conditions of FE model to validate effective length corrected results from semi-analytical model and joint fixity of experimental set-up.

Chapter 4 – Semi-Analytical Method

In this chapter, a baseline semi-analytical model for the plate is derived to estimate the critical buckling loads of the structure and the effect of initial imperfections through a Newton-Raphson iteration. In contrast to analytical models, semi-analytical models require a certain amount of computing power to carry out iterative calculations. The model is derived employing simply-supported boundary conditions as it reduced the complexity considerably of an already convoluted derivation. Afterwards, the model can be solved with inclusion of the effective length correction factors chosen to best approximate the clamped stated of the plate.

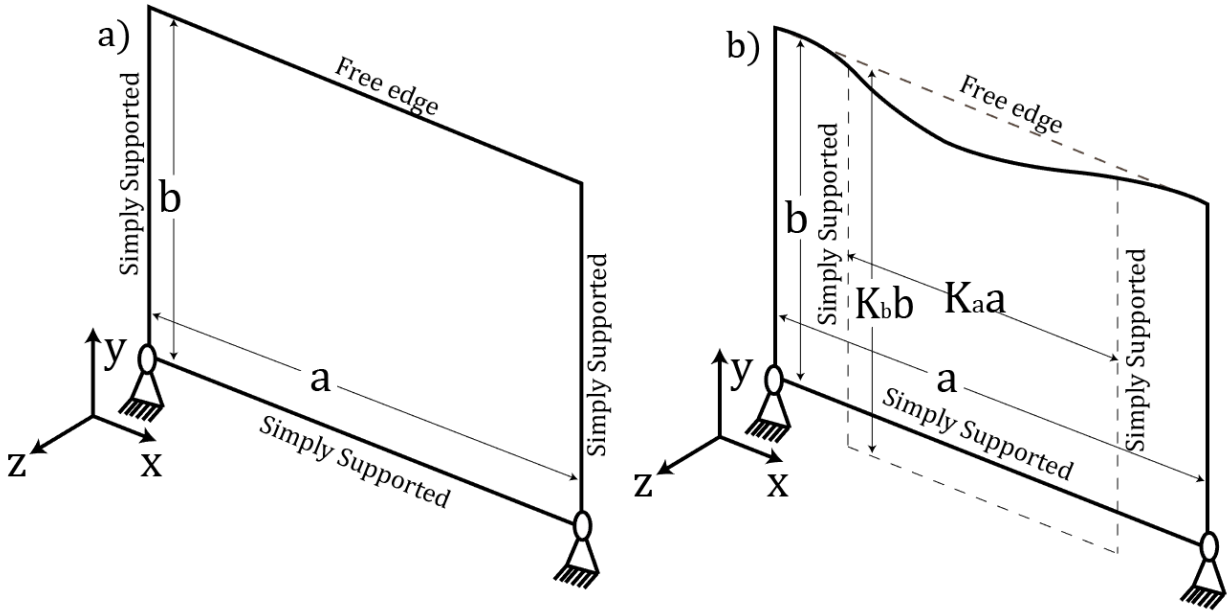

Figure 4.1a) Simply supported boundary conditions for semi-analytical model. b) Effective length correction factors $K_a = 0.65$ and $K_b = 1.2$ according to [28].

A question arises regarding the inclusion of the adhesive line within the model, whether it has an effect on the resulting buckling loads. Two solutions are proposed: modelling the plates fully bonded or disregarding the presence of the adhesive entirely. Finally, comparison of preliminary results from these approaches is given to show the difference between them, from which a decision is made on how to employ the semi-analytical tool.

4.1 Plate Properties – Constitutive Matrix

Classical Laminated Plate Theory is employed in the determination of the stiffness properties of the plates. Assuming that the facesheets of the modelled plate are orthotropic, the 3D stiffness matrix $[Q]$ for the plate can be determined using the inverse of the compliance matrix $[S]$ [33]:

$$[Q] = \begin{bmatrix} \frac{1-\mu_{yz}\mu_{zy}}{E_y E_z \Delta} & \frac{\mu_{yx}+\mu_{yz}\mu_{zx}}{E_y E_z \Delta} & \frac{\mu_{zx}+\mu_{yx}\mu_{zy}}{E_x E_y \Delta} & 0 & 0 & 0 \\ & \frac{1-\mu_{xz}\mu_{zx}}{E_x E_z \Delta} & \frac{\mu_{zy}+\mu_{xy}\mu_{zx}}{E_y E_z \Delta} & 0 & 0 & 0 \\ & & \frac{1-\mu_{xy}\mu_{yx}}{E_x E_y \Delta} & 0 & 0 & 0 \\ & & & G_{yz} & 0 & 0 \\ & SYMMETRIC & & & G_{zx} & 0 \\ & & & & & G_{xy} \end{bmatrix} \quad (4.1)$$

Where the determinant of the stiffness matrix is as follows:

$$\Delta = \frac{1-\mu_{xy}\mu_{yx}-\mu_{yz}\mu_{zy}-\mu_{xz}\mu_{zx}-2\mu_{yx}\mu_{zy}\mu_{xz}}{E_x E_y E_z} \quad (4.2)$$

The stiffness matrix $[Q]$ directly relates stresses to strains. Given a stress vector $\{\sigma\} = \{\sigma_x\ \sigma_y\ \sigma_z\ \tau_{yz}\ \tau_{zx}\ \tau_{xy}\}'$ and a strain vector $\{\varepsilon\} = \{\varepsilon_x\ \varepsilon_y\ \varepsilon_z\ \gamma_{yz}\ \gamma_{zx}\ \gamma_{xy}\}'$, the relationship is given by:

$$\{\sigma\} = [Q]\{\varepsilon\} \quad (4.3)$$

As can be seen on Appendix A, the only Poisson ratios given for the facehseets are μ_{xy}, μ_{yz} and μ_{zx}. Using reciprocal relations with the Young's modulus provided, the remaining Poisson ratios can be obtained:

$$\mu_{yx} = \frac{E_y}{E_x}\mu_{xy} \qquad \mu_{zy} = \frac{E_z}{E_y}\mu_{yz} \qquad \mu_{xz} = \frac{E_x}{E_z}\mu_{zx} \quad (4.4)$$

4.1.1 ABD Matrix

Classical Laminated Plate Theory (CLPT) was introduced briefly in chapter 2.2.2 and the relevant stiffness properties are obtained in this section. To calculate the ABD matrix for the entire plate, an integration of the thickness of the respective ply is done for the i[th] terms of the constitutive matrix $[Q]$ for $i = 1,2,6$ and the rotation matrix $[R]$ over the skew angle Ψ, in order to align the fibers parallel to the skewed edges:

$$[A_{3x3}] = \int_{-h/2}^{h/2} [R][Q_i][R]'\, dz \quad (4.5)$$

$$[B_{3x3}] = \int_{-h/2}^{h/2} [R][Q_i][R]'(z)\, dz \tag{4.6}$$

$$[D_{3x3}] = \int_{-h/2}^{h/2} [R][Q_i][R]'(z^2)\, dz \tag{4.7}$$

The rotation over the skew angle is given by the matrix below for the respective i[th] terms from the stiffness matrix $[Q]$:

$$[R] = \begin{bmatrix} \cos^2\Psi & \sin^2\Psi & 2\cos\Psi\sin\Psi \\ \sin^2\Psi & \cos^2\Psi & -2\cos\Psi\sin\Psi \\ -\cos\Psi\sin\Psi & \cos\Psi\sin\Psi & \cos^2\Psi - \sin^2\Psi \end{bmatrix} \tag{4.8}$$

An important challenge arises in calculating the effect of the trailing edge bond covering only a fraction of the plate's width on the $[ABD]$ matrix. An initial approach to modelling the bonded plate was to assume a sandwich plate with the composite plates acting as facesheets and the adhesive as core based on Helms et al [17], but delimiting the bonded area due to the adhesive is difficult without employing an advanced penalty method that falls out of the scope of this project. The presence of the adhesive bond is not expected to increase the extension-shearing properties $[A]$ of the plate as its mechanical properties are much lower than those of the composite plates; on the other hand, the bending-twisting properties $[D]$ are significantly increased. Two extreme scenarios are then modelled:

1) A fully bonded sandwich plate which includes the adhesive mechanical properties and thickness in the calculation of the plate's $[ABD]$ matrix.

2) Modelling each composite plate separately, neglecting the presence of the adhesive bond and its effect on the $[D]$ matrix.

4.2 Potential Energy Equation

The Principle of Minimum Potential Equation (PMPE) is based on the knowledge that for a conservative structure, the state of stable equilibrium of the system will undergo the path of minimum energy within the kinematically admissible deformations. By stating the total potential energy of the system as a sum of the internal strain energy due to the deformations and the work potential done by external body forces, the resulting equation can be minimized to find the critical point of stability.

4.2.1 Internal Strain Energy

Using the minimum potential energy method, the increments internal strain energy δU and the work done by external forces δW must be derived, as done by C. Kassapoglou [25] (*Design and Analysis of Composite Structures, Chapter 5.4 page 108*). For the internal strain energy:

$$\delta U = \iiint_V \{\sigma_x \delta\varepsilon_x + \sigma_y \delta\varepsilon_y + \sigma_z \delta\varepsilon_z + \tau_{xz}\delta\gamma_{xz} + \tau_{xy}\delta\gamma_{xy} + \tau_{yz}\delta\gamma_{yz}\} dxdydz \tag{4.9}$$

However, the transverse stress is neglected ($\sigma_z = 0$) and the internal variation of energy is:

$$\delta U = \iiint_V \{\sigma_x \delta\varepsilon_x + \sigma_y \delta\varepsilon_y + \tau_{xy}\delta\gamma_{xy} + \tau_{xz}\delta\gamma_{xz} + \tau_{yz}\delta\gamma_{yz}\} dxdydz \tag{4.10}$$

In the equation above, the stresses can be integrated over z to yield the internal forces and moments, including the contribution from the transverse shears as shown in [25]:

$$\int_{-\frac{h}{2}}^{\frac{h}{2}} \begin{bmatrix} \sigma_x \\ \sigma_y \\ \tau_{xy} \end{bmatrix} dz = \begin{bmatrix} N_x \\ N_y \\ N_{xy} \end{bmatrix}, \int_{-\frac{h}{2}}^{\frac{h}{2}} z \begin{bmatrix} \sigma_x \\ \sigma_y \\ \tau_{xy} \end{bmatrix} dz = \begin{bmatrix} M_x \\ M_y \\ M_{xy} \end{bmatrix} \tag{4.11}$$

Substituting the forces and moments into the internal energy variation yields:

$$\delta U = \iint_A \{N_x \delta\varepsilon_x^0 + N_y \delta\varepsilon_y^0 + N_{xy}\delta\gamma_{xy}^0 + M_x \delta\kappa_x + M_y \delta\kappa_y + M_{xy}\delta\kappa_{xy}\} dxdy \tag{4.12}$$

From the ABD matrix of the material, the stretching (membrane), bending and stretching-bending change of energy can be obtained from the relation between forces and moments to mid-plane strains and curvatures as stated in equation 2.4 and repeated below for clarity:

$$\begin{Bmatrix} N_x \\ N_y \\ N_{xy} \\ M_x \\ M_y \\ M_{xy} \end{Bmatrix} = \begin{bmatrix} A_{11} & A_{12} & A_{16} & B_{11} & B_{12} & B_{16} \\ A_{21} & A_{22} & A_{26} & B_{21} & B_{22} & B_{26} \\ A_{61} & A_{62} & A_{66} & B_{61} & B_{62} & B_{66} \\ B_{11} & B_{12} & B_{16} & D_{11} & D_{12} & D_{16} \\ B_{21} & B_{22} & B_{26} & D_{21} & D_{22} & D_{26} \\ B_{61} & B_{62} & B_{66} & D_{61} & D_{62} & D_{66} \end{bmatrix} \begin{Bmatrix} \varepsilon_x^0 \\ \varepsilon_y^0 \\ \gamma_{xy}^0 \\ \kappa_x^0 \\ \kappa_y^0 \\ \kappa_{xy}^0 \end{Bmatrix} \tag{2.4/4.13}$$

Solving for every force and moment and substituting into δU:

$$\delta U = \iint_A [(A_{11}\varepsilon_x^0 + A_{12}\varepsilon_y^0 + A_{16}\gamma_{xy}^0 + B_{11}\kappa_x + B_{12}\kappa_y + B_{16}\kappa_{xy})\delta\varepsilon_x^0 + (A_{12}\varepsilon_x^0 + A_{22}\varepsilon_y^0 + A_{26}\gamma_{xy}^0 + B_{12}\kappa_x + B_{22}\kappa_y + B_{26}\kappa_{xy})\delta\varepsilon_y^0 + (A_{16}\varepsilon_x^0 + A_{26}\varepsilon_y^0 + A_{66}\gamma_{xy}^0 + B_{16}\kappa_x + B_{26}\kappa_y + B_{66}\kappa_{xy})\delta\gamma_{xy}^0 + (B_{11}\varepsilon_x^0 + B_{12}\varepsilon_y^0 + B_{16}\gamma_{xy}^0 + D_{11}\kappa_x + D_{12}\kappa_y + D_{16}\kappa_{xy})\delta\kappa_x + (B_{12}\varepsilon_x^0 + B_{22}\varepsilon_y^0 + B_{26}\gamma_{xy}^0 + D_{12}\kappa_x + D_{22}\kappa_y + D_{26}\kappa_{xy})\delta\kappa_y + (B_{16}\varepsilon_x^0 + B_{26}\varepsilon_y^0 + B_{66}\gamma_{xy}^0 + D_{16}\kappa_x + D_{26}\kappa_y + D_{66}\kappa_{xy})\delta\kappa_{xy}]\, dxdy \quad (4.14)$$

$$U_A = \frac{1}{2}\iint_A \{\varepsilon'[A]\varepsilon\}\, dA \qquad U_B = \iint_A \{\varepsilon'[B]\kappa\}\, dA \quad (4.15a\text{-}16a)$$

$$U_D = \frac{1}{2}\iint_A \{\kappa'[D]\kappa\}\, dA \quad (4.17a)$$

The variation of the internal energy δU is rearranged into the terms pertaining to the A, B and D matrix respectively:

$$U_A = \frac{1}{2}\iint_A \left\{A_{11}(\varepsilon_x^0)^2 + 2A_{12}(\varepsilon_x^0)(\varepsilon_y^0) + 2A_{16}(\varepsilon_x^0)(\gamma_{xy}^0) + A_{22}(\varepsilon_y^0)^2 + 2A_{26}(\varepsilon_y^0)(\gamma_{xy}^0) + A_{66}(\gamma_{xy}^0)^2\right\} dxdy \quad (4.15\text{-b})$$

$$U_B = \iint_A \left\{B_{11}(\varepsilon_x^0)\kappa_x + B_{12}\left((\varepsilon_y^0)\kappa_x + (\varepsilon_x^0)\kappa_y\right) + B_{16}\left((\gamma_{xy}^0)\kappa_x + (\varepsilon_x^0)\kappa_{xy}\right) + B_{22}(\varepsilon_y^0)\kappa_y + B_{26}\left((\gamma_{xy}^0)\kappa_y + (\varepsilon_y^0)\kappa_{xy}\right) + B_{66}(\gamma_{xy}^0)\kappa_{xy}\right\} dxdy \quad (4.16b)$$

$$U_D = \frac{1}{2}\iint_A \{D_{11}\kappa_x^2 + 2D_{12}\kappa_x\kappa_y + 2D_{16}\kappa_x\kappa_{xy} + D_{22}\kappa_y^2 + 2D_{26}\kappa_y\kappa_{xy} + D_{66}\kappa_{xy}^2\} dxdy \quad (4.17b)$$

$$U = U_A + U_B + U_D \quad (4.18)$$

4.2.2 Energy from External Work and initial deflection

The work done on a plate from a distributed edge load for buckling problems is given by equation 3.20, where δW_b is the variation of body forces and δW_s of surface forces. By expanding the variation of the body and surface forces in equation 3.21 the relevant distributed in-plane forces N_x, N_y, shear force N_{xy}, transverse shears Q_x and Q_y and edge moments M_x and M_y can be obtained:

$$\delta W = \delta W_b + \delta W_s \quad (4.19)$$

$$= \iint_A \{p_x \delta u + p_y \delta v + p_z \delta w\} dx dy$$
$$+ \int_0^b \left[N_x \delta u + N_{xy} \delta v + Q_x \delta w - M_x \delta \left(\frac{\delta w}{\delta x} \right) \right]_{x=0}^{x=a} dy \quad (4.20)$$
$$+ \int_0^a \left[N_{xy} \delta u + N_y \delta v + Q_y \delta w - M_y \delta \left(\frac{\delta w}{\delta y} \right) \right]_{y=0}^{y=b} dx$$

Consider the normal and shear force resultants:

$$\frac{\delta N_x}{\delta x} + \frac{\delta N_{xy}}{\delta y} = p_x \quad (4.21)$$

$$\frac{\delta N_{xy}}{\delta x} + \frac{\delta N_y}{\delta y} = p_y \quad (4.22)$$

$$\frac{\delta Q_x}{\delta x} + \frac{\delta Q_y}{\delta y} = p_z = 0 \quad (4.23)$$

Substituting these into the first term of the external work differential and solving the terms yield the following external work equation which will serve to calculate the critical buckling load from the edge distributed in-plane load terms N_x and N_y:

$$\iint_A \{p_x \delta u + p_y \delta v\} dx dy = \iint_A \left\{ \left(-\frac{\delta N_x}{\delta x} - \frac{\delta N_{xy}}{\delta y} \right) \delta u + \left(-\frac{\delta N_{xy}}{\delta x} - \frac{\delta N_y}{\delta y} \right) \delta v \right\} dx dy \quad (4.24)$$

$$W = -\frac{1}{2} \iint_A \left\{ N_x \left(\left(\frac{\delta w}{\delta x} \right)^2 \right) + N_y \left(\left(\frac{\delta w}{\delta y} \right)^2 \right) \right\} dx dy \quad (4.25)$$

Chapter 3.1.1 established that under a pure edgewise bending moment, the modelled section would undergo a uniaxial compressive load in the x-direction, therefore only the external work term containing N_x is kept. The solution of the analytical method proposed in this section yields a constant distributed edge force. In the results section, it will be discussed how this distributed edge force compares to its numerical and experimental loading counterparts.

It is important in the external work contribution to the potential energy equation to include initial imperfections $\overline{w}(x, y)$ on the structure. Daripa & Singha [16] determined the inclusion of such term as strain-free, therefore disregarding it in the internal strain energy part of the equation. The final form of the external work contribution is:

$$W = -\frac{1}{2} \iint_A \left\{ N_x \left(\left(\frac{\delta w}{\delta x} \right)^2 + 2 \frac{\delta \overline{w}}{\delta x} \frac{\delta w}{\delta x} \right) \right\} dx dy \quad (4.26)$$

The internal strain and external work equations can finally be added to obtain the potential energy equation. Simplifications to the potential energy equation come from the fact that the plates are balanced and symmetric and therefore $[B] = 0$.

$$\Pi = U + W \tag{4.27}$$

$$\frac{1}{2}\iint_A \left\{A_{11}(\varepsilon_x^0)^2 + 2A_{12}(\varepsilon_x^0)(\varepsilon_y^0) + 2A_{16}(\varepsilon_x^0)(\gamma_{xy}^0) + A_{22}(\varepsilon_y^0)^2 + 2A_{26}(\varepsilon_y^0)(\gamma_{xy}^0) + A_{66}(\gamma_{xy}^0)^2\right\} dxdy$$
$$+\frac{1}{2}\iint_A \left\{D_{11}(\kappa_x)^2 + 2D_{12}(\kappa_x)(\kappa_y) + 2D_{16}(\kappa_x)(\kappa_{xy}) + D_{22}(\kappa_y)^2 + 2D_{26}(\kappa_y)(\kappa_{xy}) + D_{66}(\kappa_{xy})^2\right\} dxd$$
$$-\frac{1}{2}\iint_A \{N_x((w_x)^2 + 2\bar{w}_x w_x)\} dxdy \tag{4.28}$$

4.3 Boundary Conditions and Displacement Fields

In plate buckling problems, displacement fields can be given as the product of functions from the two most prominent plate dimensions. More specifically, the displacement fields $u(x,y)$, $v(x,y)$ and $w(x,y)$ proposed in section 2.2.3 for the equilibrium and stability equations may be given as:

$$u(x,y) = f_u(x)f_u(y) \tag{4.29a}$$
$$v(x,y) = f_v(x)f_v(y) \tag{4.30a}$$
$$w(x,y) = f_w(x)f_w(x) \tag{4.31a}$$

Based on the work of Singh et al. [32] the behavior for large deflection of the plate with sliding edges can be approached with the allowable displacement fields $u(x,y)$ and $v(x,y)$ in equations (4.29b-30b) below such that the boundary conditions in equations (4.32-4.33) are satisfied. For the sake of simplicity in the analytical model, the constrained edges were assumed to be simply supported, yielding an out-of-plane displacement field $w(x,y)$ (4.31b), determined such that the geometric boundary conditions are met (4.34-4.35):

$$u(x,y) = u_0 \cos\left(\frac{m\pi x}{a}\right)\sin\left(\frac{\lambda n\pi y}{b}\right) \tag{4.29b}$$
$$v(x,y) = v_0 \sin\left(\frac{m\pi x}{a}\right)\sin\left(\frac{\lambda n\pi y}{b}\right) \tag{4.30b}$$
$$w(x,y) = w_0 \sin\left(\frac{m\pi x}{a}\right)\sin\left(\frac{\lambda n\pi y}{b}\right) \tag{4.31b}$$

$$u(0,y) \neq 0 \quad u(a,y) \neq 0 \tag{4.32}$$
$$v(x,b) \neq 0 \tag{4.33}$$
$$w(0,y) = w(a,y) = 0 \tag{4.34}$$
$$w(x,0) = 0 \tag{4.35}$$

It is important to note the constant $\lambda = \frac{5}{12}$, introduced by Kassapoglou [25] for plates with a free edge. This constant ensures that there is still a slope at the free edge $y = b$. Since this is an unconstrained edge, having a slope equal to zero (and thus a reactionary moment) is not the case in question.

4.4 Total Potential Energy Integration

Up until this point, the equations of equilibrium and stability for the plate have been obtained from textbook formulations ([25][26][27][28][29]). Implementing the chosen boundary conditions for the custom plate model that allow for in-plane displacements on the hinged edges and the free-edge of the plate that will undergo large out-of-plane displacements due to coupling induced by the Von-Karman strain-displacement relations is a derivation specific to this research.

As it has been mentioned, the sliding short edges of the plate allow for large out-of-plane displacements due to buckling, as these are coupled with the in-plane motion. Von Karman's strain-displacement relations establish this relationship along the mid-plane of the plate, given by equations 2.5, repeated below for clarity:

$$\varepsilon_x^0 = \frac{\partial u}{\partial x} + \frac{1}{2}\left(\frac{\partial w}{\partial x}\right)^2 \qquad \varepsilon_y^0 = \frac{\partial v}{\partial y} + \frac{1}{2}\left(\frac{\partial w}{\partial y}\right)^2 \qquad \gamma_{xy}^0 = \frac{\partial u}{\partial y} + \frac{\partial v}{\partial x} + \frac{\partial w}{\partial x}\frac{\partial w}{\partial y} \qquad (2.5/4.36)$$

Additional to these, the curvature terms of the plate are given by the terms:

$$\kappa_x = -\frac{\partial^2 w}{\partial x^2} \qquad \kappa_y = -\frac{\partial^2 w}{\partial y^2} \qquad \kappa_{xy} = -2\frac{\partial^2 w}{\partial x\, \partial y} \qquad (2.5/4.36)$$

In order to evaluate all the terms of the double integral of the total potential energy equation (4.34), it is necessary to expand the mid-plane strain terms being squared and multiplied, from which three types of integrand terms will be obtained: Linear in-plane displacement terms, terms that couple in-plane and out-of-plane and lastly non-linear terms that dictate the post-buckling behavior of the plate, given respectively in table 4.1. At this point a slight change in notation is carried out such that a subscript given to a displacement field denotes a partial derivative in terms of said subscript, e.g. u_x denotes the partial derivative of $u(x, y)$ in terms of x, w_{yy} denotes a double partial derivative of $w(x, y)$ in terms of y and so on.

	Linear in-plane	**In-plane/Out-of-plane coupling**	**Non-linear Out-of-plane**
$\left(\boldsymbol{\varepsilon_x^0}\right)^2$	u_x^2	$\frac{1}{2}u_x w_x^2$	$\frac{1}{4}w_x^4$
$\left(\boldsymbol{\varepsilon_x^0}\right)\left(\boldsymbol{\varepsilon_y^0}\right)$	$u_x v_y$	$\frac{1}{2}(u_x w_y^2 + v_y w_x^2)$	$\frac{1}{4}w_x^2 w_y^2$

$(\boldsymbol{\varepsilon_y^0})^2$	v_y^2	$\frac{1}{2}v_y w_y^2$	$\frac{1}{4}w_y^4$
$(\boldsymbol{\varepsilon_x^0})(\boldsymbol{\gamma_{xy}^0})$	$u_x u_y + u_x v_x$	$\frac{1}{2}(u_y w_x^2 + v_x w_x^2) + u_x w_x w_y$	$\frac{1}{2}w_x^3 w_y$
$(\boldsymbol{\varepsilon_y^0})(\boldsymbol{\gamma_{xy}^0})$	$u_y v_y + v_x v_y$	$\frac{1}{2}(u_y w_y^2 + v_x w_y^2) + v_y w_x w_y$	$\frac{1}{2}w_x w_y^3$
$(\boldsymbol{\gamma_{xy}^0})^2$	$u_y^2 + 2u_y v_x + v_x^2$	$2(u_y w_x w_y + v_x w_x w_y)$	$w_x^2 w_y^2$

Table 4.1 – Linear, coupling and non-linear strain terms of the total potential energy equation which factor the stretching/shearing terms of the $[A]$ stiffness matrix.

Table 4.2 below gives the curvature terms from the bending stiffness values of the total potential energy.

Curvature term	Displacement derivative	Curvature term	Displacement derivative
$(\boldsymbol{\kappa_x})^2$	w_{xx}^2	$(\kappa_x)(\kappa_y)$	$w_{xx}w_{yy}$
$(\boldsymbol{\kappa_x})(\boldsymbol{\kappa_{xy}})$	$2w_{xx}w_{xy}$	$(\kappa_y)^2$	w_{yy}^2
$(\boldsymbol{\kappa_y})(\boldsymbol{\kappa_{xy}})$	$w_{yy}w_{xy}$	$(\kappa_{xy})^2$	$4w_{xy}^2$

Table 4.2 – Curvature terms which factor the bending stiffness terms from the $[D]$ matrix.

Carrying out the integrals for all the terms is a lengthy process, but by using the property of orthogonality of the x-dependent functions for all displacement fields can simplify things considerably.

The property of orthogonality of the x-function allows for a straightforward integration. These properties, otherwise known as orthogonal relations, state that the integration of trigonometric functions can be determined as follows:

$$\int_0^a \sin\left(\frac{m\pi x}{a}\right)\sin\left(\frac{n\pi x}{a}\right)dx = \begin{cases}\frac{a}{2}\ if\ m = n \neq 0\\ 0\ if\ m\ \neq n\end{cases} \tag{4.37a}$$

$$\int_0^a \cos\left(\frac{m\pi x}{a}\right)\cos\left(\frac{n\pi x}{a}\right)dx = \begin{cases}\frac{a}{2}\ if\ m = n \neq 0\\ 0\ if\ m\ \neq n\\ a\ if\ m = n = 0\end{cases} \tag{4.37b}$$

$$\int_0^a \sin\left(\frac{m\pi x}{a}\right)\cos\left(\frac{n\pi x}{a}\right)dx = 0 \tag{4.37c}$$

These integration properties may be freely applied to the terms of the displacement fields along the x-direction as they are trigonometric functions of integers: 1 for the in-plane displacement fields $u(x,y)$, $v(x,y)$ and m for the out-of-plane. However, due to the presence of the free-edge constant λ,

the integration for the y-functions must be fully carried out for every term. These integrations will not be fully expanded here for the sake of brevity, but the final result for every term is provided in appendix C.

4.4.1 Initial Imperfection Terms in Semi-Analytical Model

Initial imperfection terms $\overline{w_x}w_x$

Two initial imperfections are included in the study of the semi-analytical model: blade twist as an initial deflection and secondly, as will be mentioned in Chapter 4 and Chapter 6, a pre-bent displacement caused by a failed experimental test.

Twist as initial deflection

As discussed in section 3.1 regarding the approach of simplifying the geometric dimensions of the blade, the twist is included as a strain-free displacement field $\overline{w}(x,y)$ which attains its maximum at the corner of the plate with the coordinates $x = a$ and $y = b$ with the form:

$$\overline{w}(x,y) = y\sin(\beta_m x) \tag{4.38}$$

From which the first derivative with respect to x is:

$$\overline{w_x}(x,y) = \beta_m y\cos(\beta_m x) \tag{4.39}$$

Substituting $\overline{w_x}$ and the general out-of-plane displacement derivative with respect to x, w_x into a double integral, the equation below can be evaluated:

$$\iint_A \overline{w_x}\, w_x dA = w_0\beta_m\left(\frac{m\pi}{a}\right)\int_0^a \cos(\beta_m x)\cos\left(\frac{m\pi x}{a}\right)dx \int_0^b y\sin\left(\frac{\lambda\pi y}{b}\right)dy$$

Orthogonal properties may no longer be applied to the x-integral as the value of β_m will no longer be an integer. Therefore, the x-integral is expanded for every term:

$$\int_0^a \cos(\beta_m x)\cos\left(\frac{m\pi x}{a}\right)dx$$

$$= \int_0^a \frac{1}{2}\left[\cos\left(\left(\beta_m - \frac{m\pi}{a}\right)x\right) + \cos\left(\left(\beta_m + \frac{m\pi}{a}\right)x\right)\right]dx$$

Integrating every term yields the following equation:

$$-\frac{1}{2}\left[\frac{a\sin(\beta_m a - m\pi)}{(\beta_m a - m\pi)} + \frac{a\sin(\beta_m a + m\pi)}{(\beta_m a + m\pi)}\right]$$

The y-integral is stated below once more, and its integration is carried out through integration by parts:

$$\int_0^b y \sin\left(\frac{\lambda\pi y}{b}\right) dy = \left(\frac{b}{\lambda\pi}\right)^2 \sin(\lambda\pi) - \frac{b^2}{\lambda\pi}\cos(\lambda\pi)$$

Substituting both solved integrals into the base equation is given below:

$$\iint_A \overline{w_x}\, w_x dA = \frac{w_0\beta_m}{2}\left(\frac{m\pi}{a}\right)\left[\frac{a\sin(\beta_m a - m\pi)}{(\beta_m a - m\pi)} + \frac{a\sin(\beta_m a + m\pi)}{(\beta_m a + m\pi)}\right]\left[\frac{b^2}{\lambda\pi}\cos(\lambda\pi) - \left(\frac{b}{\lambda\pi}\right)^2 \sin(\lambda\pi)\right]$$

Extracting the common a term from the first integral and the b^2 term from the second one, solving for the values of λ and π yields:

$$\iint_A \overline{w_x}\, w_x dA = -0.5749\, w_0\beta_m m b^2 \left[\frac{\sin(\beta_m a - m\pi)}{(\beta_m a - m\pi)} + \frac{\sin(\beta_m a + m\pi)}{(\beta_m a + m\pi)}\right] \quad (4.40)$$

When including this initial displacement, any twist-per-meter β_m can be included, and it is noteworthy that this chosen normalized parameter successfully includes the required flexibility when accounting for the plate length a.

Pre-bent of a plate as initial deflection

Chapter 7 includes remarks on the failed first experimental test due to inappropriate clamping materials on the edge of the plate opposing the free edge. This specimen remained slightly pre-bent after the load was released, and an extra test was carried out to determine the loss of load-bearing of the structure. An implementation of this pre-bent is included in the semi-analytical model for the following strain-free initial displacement field for a single half-sine wave along the x-direction of the plate:

$$\bar{w}(x,y) = w_{ini} \sin\left(\frac{\pi x}{a}\right)\sin\left(\frac{\lambda\pi y}{b}\right) \quad (4.41)$$

The coefficient w_{ini} is the maximum amplitude of the initial displacement, which will be left undetermined at this point to provide a general solution.

The double integral of the initial displacement is:

$$\iint_A \overline{w_x}\, w_x dA = w_{ini} w_0\, m \left(\frac{\pi}{a}\right)^2 \int_0^a \cos\left(\frac{\pi x}{a}\right)\cos\left(\frac{m\pi x}{a}\right) dx \int_0^b \sin^2\left(\frac{\lambda\pi y}{b}\right) dy$$

Both integrals are solved separately. Firstly, the x-integral yields the following result by applying the orthogonal relation 4.37b:

$$\int_0^a \cos\left(\frac{\pi x}{a}\right)\cos\left(\frac{m\pi x}{a}\right) dx$$

$$= \frac{a}{2} \; for \; m = 1$$

$$= 0 \; for \; m \neq 1$$

Whereas the y-integral yields the following:

$$\int_0^b \sin^2\left(\frac{\lambda\pi y}{b}\right) dy = \int_0^b \frac{1}{2}\left(1 - \cos\left(\frac{2\lambda\pi y}{b}\right)\right) dy$$

$$= \frac{1}{2}\left(b + \frac{b\sin\left(\frac{2\lambda\pi y}{b}\right)}{2\lambda\pi}\right)\Bigg|_0^b = \frac{b}{2}\left(1 + \frac{\sin(2\lambda\pi)}{2\lambda\pi}\right)$$

Factoring the results from both integrals is given below, after which the values of λ and π are entered and the equation is solved:

$$\iint_A \overline{w_x}\, w_x dA = \begin{cases} w_{ini} w_0 \left(\frac{\pi}{a}\right)^2 \left(\frac{a}{2}\right)\left(\frac{b}{2}\right)\left(1 + \frac{\sin(2\lambda\pi)}{2\lambda\pi}\right) \; for \; m = 1 \\ 0 \; for \; m \neq 1 \end{cases}$$

$$\iint_A \overline{w_x}\, w_x dA = \begin{cases} 2.9386\, w_{ini} w_0 \left(\frac{b}{a}\right) \; for \; m = 1 \\ 0 \; for \; m \neq 1 \end{cases}$$	(4.42)

The existence of a solution for the buckling mode $m = 1$ only demonstrates that the pre-bent shape of the plate promotes that mode and will therefore lower the buckling load upon which this mode is reached.

4.5 Rayleigh-Ritz Solution

The solution of the area integral of the total potential energy equation (4.28) has been derived so far and the resultants from every term given in Appendix C. The Rayleigh-Ritz method can now be employed with a Newton-Raphson iteration to calculate the bifurcation load at which plate buckling will commence.

The Rayleigh-Ritz method is employed by minimizing the potential energy equation in terms of the unknown displacement field coefficients. As such, the total potential energy is derived for every coefficient (eqs. 3.44-a,b,c) and equated to zero in order to be solved as an eigenvalue problem.

$$\frac{\delta\Pi}{\delta u_0} = 0 \qquad \frac{\delta\Pi}{\delta v_0} = 0 \qquad \frac{\delta\Pi}{\delta w_0} = 0 \qquad (4.43\text{-a,b,c})$$

In a common buckling problem, these derivatives can be placed in a stiffness matrix $[K_s]$ and geometric matrix $[K_g]$ multiplied by the vector of unknown coefficients $\{\delta\}$ in the form:

$$([K_s] - N_{cr}[K_g])\{\delta\} = \{0\} \tag{4.44}$$

However, in this specific plate problem with the sliding edges, the Von Karman large mid-plane displacements yield three nonlinear algebraic equations after the minimization with respect to the unknown coefficients in a problem statement similar to Singh et al [32]:

$$\frac{\delta\Pi}{\delta u_0} = C_{11}u_0 + C_{12}v_0 + C_{13}w_0^2 = 0 \tag{4.43-a}$$

$$\frac{\delta\Pi}{\delta v_0} = C_{21}u_0 + C_{22}v_0 + C_{23}w_0^2 = 0 \tag{4.43-b}$$

$$\frac{\delta\Pi}{\delta w_0} = C_{31}u_0w_0 + C_{32}v_0w_0 + C_{33}w_0^3 + (C_{34} - N_xC_{35})w_0 + C_{41}N_x = 0 \tag{4.43-c}$$

Equations (4.43-a,b,c) are the equivalent of those on the theoretical basis formulation in Chapter 2.2.2 elaborated specifically for this problem. Terms C_{xx} are expanded in appendix D for the case of the 3 constrained edges being simply-supported. The coupling between the in-plane and out-of-plane deflection amplitude coefficients stemming from the Von Karman strain-displacement relations are evident in the equilibrium equation (4.43-c). It is then necessary to solve the first two nonlinear equations for u_0 and v_0 respectively and substituting back into Eq. (4.43-c).

$$u_0 = \left[-\frac{C_{12}\left(\frac{C_{21}C_{13}}{C_{11}} - C_{23}\right)}{C_{11}\left(C_{22} - \frac{C_{21}C_{12}}{C_{11}}\right)} - \frac{C_{13}}{C_{11}} \right] w_0^2 = \mathrm{K}_1 w_0^2 \tag{4.45}$$

$$v_0 = \frac{\left(\frac{C_{21}C_{13}}{C_{11}} - C_{23}\right)}{\left(C_{22} - \frac{C_{21}C_{12}}{C_{11}}\right)} w_0^2 = \mathrm{K}_2 w_0^2 \tag{4.46}$$

$$(C_{34} - N_xC_{35})w_0 = K_3 w_0 \tag{4.47}$$

$$C_{31}\mathrm{K}_1 w_0^3 + C_{32}\mathrm{K}_2 w_0^3 + C_{33}w_0^3 + K_3 w_0 + C_{41}N_x = 0 \tag{4.48}$$

Equation (4.48) is the final resulting equation being a function of the out-of-plane amplitude coefficient w_0 and the applied edge load N_x. Through a Newton-Raphson iteration solver, the critical buckling load of the structure for a chosen aspect ratio can be obtained. The results from this model are

compared to the numerical model solutions in Chapter 7 and further recommendations for improvements of this model are given in Chapter 7.

A final remark to the semi-analytical model is given addressing the question on the 2 possibilities: including the adhesive or modelling each plate separately. Looking at the load vs. aspect ratio plots for both scenarios (figures 4.2 and 4.3), a fully bonded plate yields buckling loads in the range of $N_{cr} = 1.5x10^5 - 6x10^5\ N$, whereas modelling the two facesheets independently, disregarding the adhesive and adding their contributions together yield results in the range of $N_{cr} = 0.4x10^4 - 2x10^4\ N$.

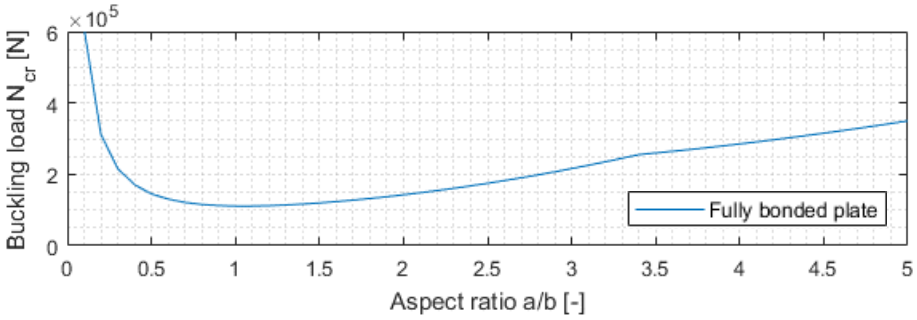

Figure 4.2 - Fully bonded composite plates load vs aspect ratio plot.

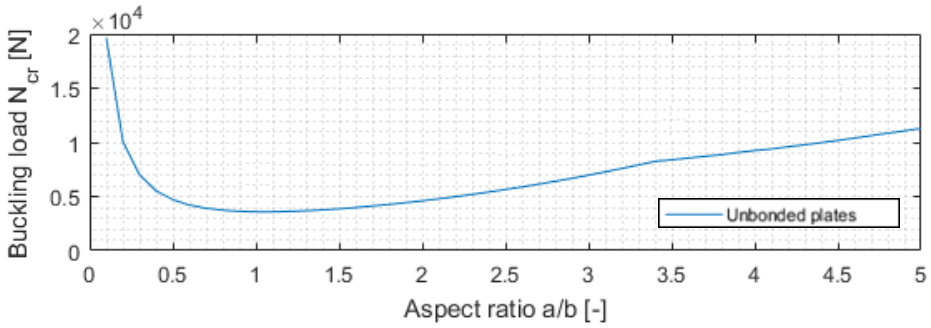

Figure 4.3 - Composite plates modelled separately and contributions to the buckling load added together.

In Chapter 7 where a comparison is drawn between the semi-analytical model and FE plates, it will be shown that disregarding the presence of the adhesive in the semi-analytical model yields results quite comparable to the numerical models where adhesive is present.

Chapter 5 – Experimental Testing

The experimental section of this project focused on designing the test set-up and the free-edge bonded joint specimens. A composite laminate was manufactured through vacuum infusion process, from which three test specimens could be made. These test specimens were manufactured to be compliant with the dimensioning and properties used in the semi-analytical and numerical models from which a comparison of the buckling behavior can be drawn. The process of bonding and adapting the edges to be mounted onto the clamp system is then explained. The clamping system was designed as a steel/nylon hinge clamp system in CATIA that would allow for edge sliding while ideally maintaining a zero slope and deflection at the constrained boundaries as previously established in figure 5.1.

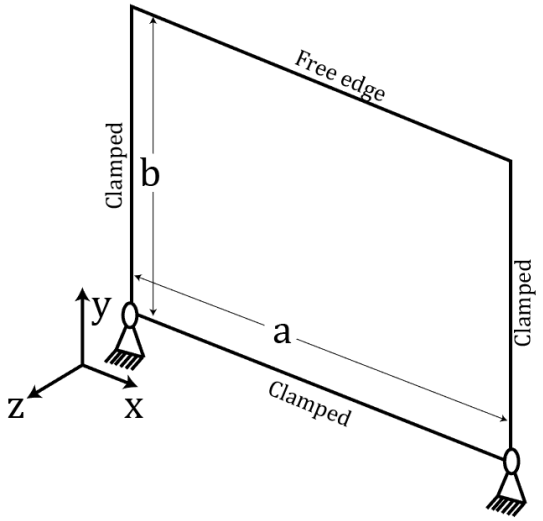

Figure 5.1 - Clamped boundary conditions for the experimental set-up.

Finally, the instrumentation of the specimens with strain gauges is shown: four strain gauges will measure the longitudinal strains along the buckling wave, while another four will measure the strains along the center of the plate to show the introduction of the edge bending moment. Following, the test set-up is shown at the $100\ kN$ compression machine. Finally, the post-processing of the output data from the test is explained.

5.1 Specimen Manufacturing

5.1.1 Composite Vacuum Infusion Process

A type E glass fiber reinforced polymer panel was manufactured at the WMC facilities using a one-sided open mould. A symmetric and balanced lay-up of 4 cross-plies ($[+45/-45/-45/+45]_s$) was used in

order to obtain a laminate that would have decouple stretching and bending ($[B] = A_{16} = A_{26} = D_{16} = D_{26} = 0$). The mould surface was pre-treated with a releasing agent upon which a peel-ply was positioned. On top of the glass fiber plies another peel-ply with a specific roughness was placed to obtain the surface which would be used for bonding of the plates. Finally, a flow mesh was added to facilitate the flow and ensure full impregnation throughout the plate (figure 5.1).

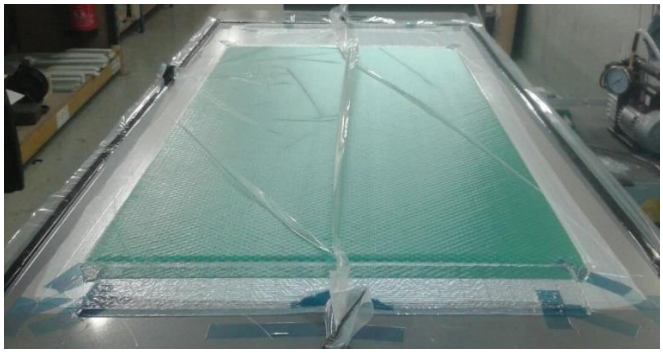

Figure 5.2 - Infusion of a 1.2x0.6m biax glass fiber composite laminate for manufacturing of test specimens.

The maximum dimension attainable for a single impregnation process was 1.20m-by-0.6m. The mechanical properties of the laminate in the fiber orientation direction are given in table 5.1 [33],[34]:

Type E Glass Fiber – Biax 12								
$E_{11}\ [MPa]$	$E_{22}\ [MPa]$	$E_{33}\ [MPa]$	$\mu_{12}\ [-]$	$\mu_{23}\ [-]$	$\mu_{31}\ [-]$	$G_{12}\ [MPa]$	$G_{23}\ [MPa]$	$G_{31}\ [MPa]$
26,000	26,000	13,190	0.15	0.15	0.08	13,500	3535	3535

Table 5.1 – Mechanical properties of Type E biax glass fiber composite in fiber directions 12.

5.1.2 Coupon Manufacturing

A trade-off was made in order to decide the dimension and number of experimental coupons to be manufactured. With a single panel infusion, three coupons with an aspect ratio of 3 could be manufactured.

Given the infused panel dimensions of $1.2x0.6\ m$, six smaller composite plates were cut. The dimensions of each plate of $0.6x0.2\ m$ was sufficient to obtain an aspect ratio of $0.5/0.1667\ = 3$, leaving $5\ cm$ on each short side and $3.3\ cm$ on the long side for clamping. The coupons obtained from this will be called TEB01, TEB02 and TEB03 from now onwards.

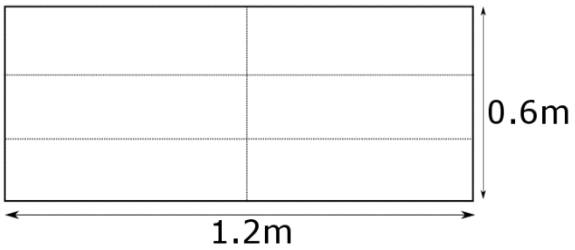

Figure 5.3 - Cutting lay-out of the infused panel.

After cutting the panels, the surfaces were thoroughly cleaned of dirt and other impurities in

preparation for bonding. Given the roughness of the peel plies used during infusion, no further surface preparations were required. The bonding paste used was a mix of Epikote resin MGS BPR 135G3 and Epikure Curing Agent MGS BPH 137G with a mixing ratio of 100:45. Table 5.2 gives the Young's modulus and Poisson ratio of the cured combined material.

Epikote MGS BPR 135G3 / Epikure MGS BPH 137G	
$E\ [MPa]$	$\mu\ [-]$
880	0.35

Table 5.2 – Young's Modulus and Poisson ratio of cured bonding paste [12].

The desired bondline was measured and, in order to keep both plates parallel to each other, nylon separators with the desired $6\ mm$ thickness were placed in an H-configuration (figure 5.4). Care was taken to fill the gap as much as possible, avoiding air-bubbles. After filling the gap with enough bonding paste, the top panel was placed (figure 5.5) and the excess bonding paste was swiped off, obtaining a clean and straight bond-line.

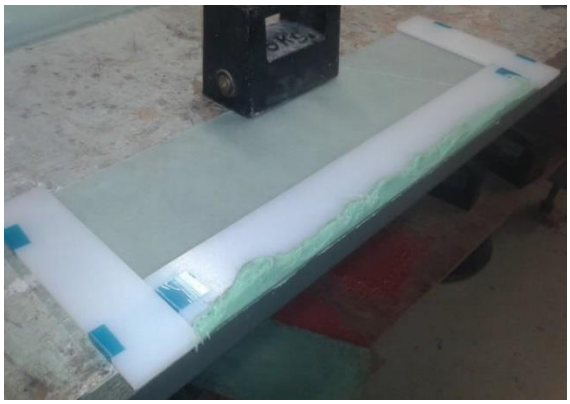

Figure 5.4 – 6 mm nylon separator placed during bonding paste adhesion used for good quality of bonding line and plate distancing.

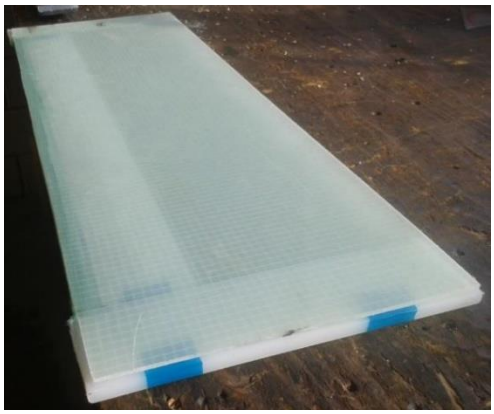

Figure 5.5 - Bonded plates after curing prior to removal of nylon separators.

An overnight curing cycle (table 5.3) was set during which metal weights were placed covering the entirety of the bond-line:

	Curing Cycle		
Temperature	30°C	50°C	70°C
Time	3 hrs	5 hrs	10 hrs

Table 5.3 – Curing cycle used for the bonding paste.

Once the curing cycle finished, the nylon separators could be carefully taken out. A picture of the bond-line quality for each testing specimen can be observed in figures 5.6, 5.7 and 5.8. A suggestion for

follow-up studies is to obtain more samples of trailing edge bond dimensions and to implement them, as well as including manufacturing defects such as uneven pressure distribution during the curing cycle or dry spots/air bubbles, as the quality of the bondline during blade manufacturing cannot be as carefully controlled as it was done in this project with conventional methods. Appendix F shows a table of the main dimensions of the test coupons.

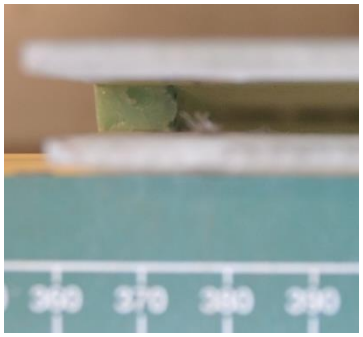

Figure 5.6 - TEB01 Bondline

Figure 5.7 -TEB02 Bondline

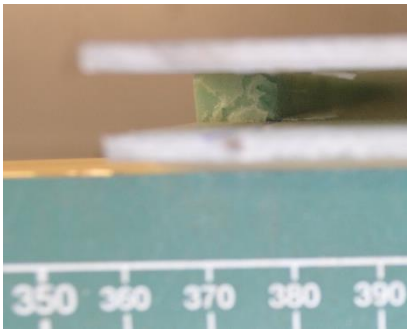

Figure 5.8 - TEB03 Bondline

5.1.3 Edge Preparation

In preparation for mounting the test specimens onto the steel/nylon clamps, $10\ mm$ diameter holes were drilled on the edges of the composite panels as can be observed in figure 5.9. This was done on coupon TEB03. Due to the difficulty of drilling through the composite panels and in order to reduce the rough handling of the remaining test specimens, gaps were instead sawed from the plate's edges into the positions for each hole. This is expected to have a negligible effect on the plate's testing as the clamps will be sufficiently tightened all along every edge and providing support to the facesheets on all sides as will be explained in the following section.

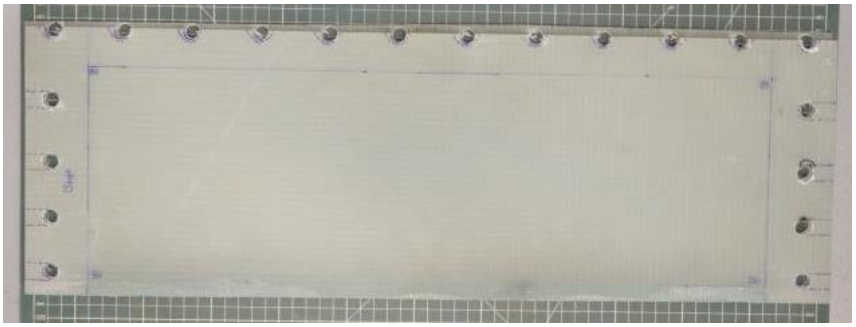

Figure 5.9 - Drilled bonded plate with delimited dimensioning.

5.2 Hinged Clamp System Design

CATIA V5 was used to design the clamp system for the experimental testing of the bonded plate specimens. The clamp consisted of a combination of steel and nylon edge pieces chosen as a trade-off for

stiffness vs. lightness of the clamp (safety measures at the WMC facilities only allow a maximum of $10\ kg$. weight to be handled by employees). Steel was chosen for its Young's modulus, which by being much higher than the glass fiber biax plates it was expected to prevent out-of-plane displacement at the edges.

5.2.1 Clamp

Joint fixity is an important aspect when designing an experimental test set-up. Clamped boundaries around the three chosen edges of the plate not only prevent out-of-plane displacement, they also ensure a controlled introduction of the load into the structure. Additionally, the experimental boundary constraints must resemble as much as possible the constraints that will be imposed in the FE model such that the results can be reliably compared to each other.

For each constrained edge of the plate, three pieces are designed in a way that will provide support to both facesheets as shown in figures 5.10a and 5.11. The clamps placed on the short edges of the plate (sliding clamps) consist of two external steel pieces and a nylon one in the middle. The middle one has a thickness of 6mm in order to keep a constant separation between the specimen's plates while mounted. The long edge clamp opposite to the free bonded edge (posterior clamp) initially consisted of 2 outer nylon plates and a middle steel one, and a redesign required the nylon pieces to be remade with steel.

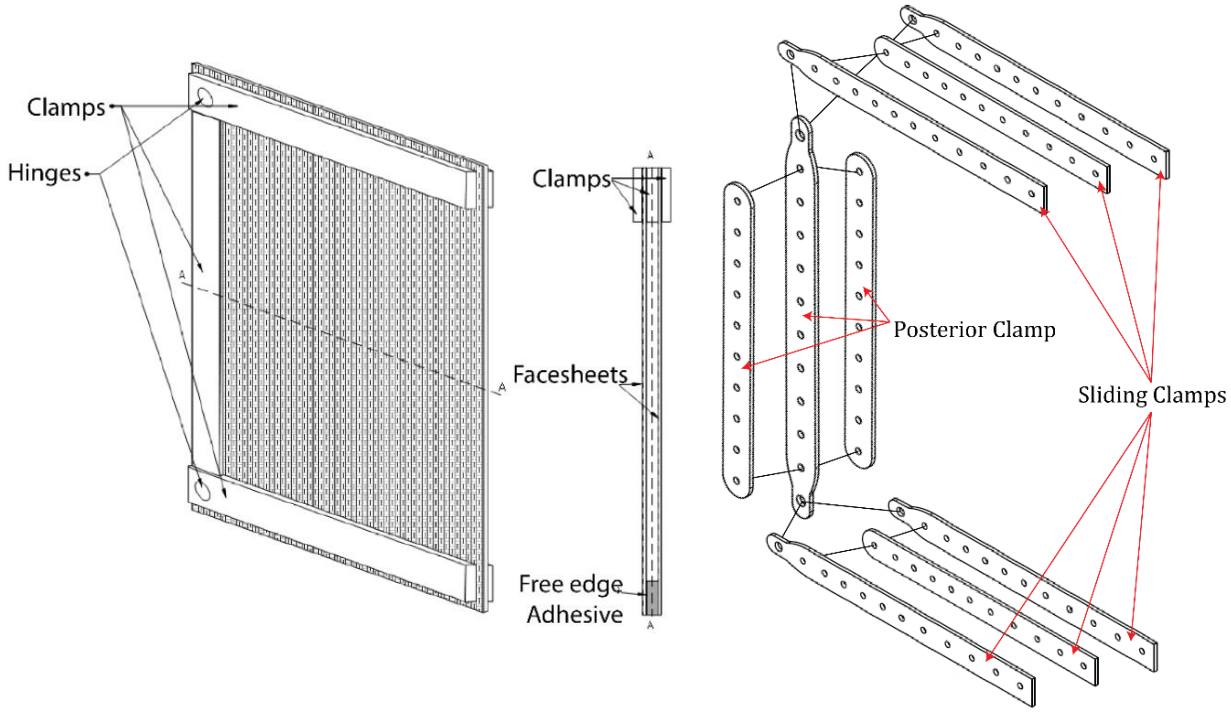

Figure 5.10 a) Preliminary hinged clamp design for adhesive bonded joint plates for buckling tests. b) Exploded view of CATIA clamp elements. Full details found on Appendix E.

Even though this research will only test plates of aspect ratio $AR = 3$, the short edges were drilled with holes at uneven separation (Appendix E GroupID 4) such that aspect ratios $1,2,3,4$ and 5 can be mounted. The long edge had its holes drilled every $5\ cm$. Hinges were placed at the connection between the sliding short edges and the long edge, which would allow an in-plane motion. Appendix E shows the detailed CATIA technical drawing and assembly for the clamp system.

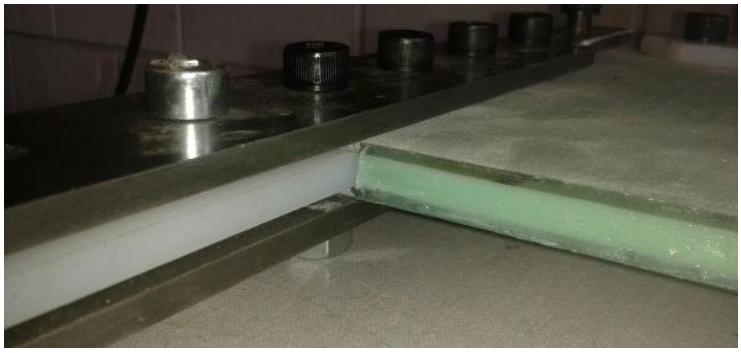

Figure 5.11 - Short edge clamp supporting both facesheets.

5.3 Instrumentation and Test Set-Up

5.3.1 Strain Gauge Placement

Eight measurement channels allowed each test to place 8-single direction strain gauges on the surface of one facesheet for each specimen. The configuration chosen for these strain gauges is shown in figure 5.12 below, where strain gauges 1-4 were placed $2.5\ cm$ off from the free edge aligned at points $[a/8\ , 3a/8,\ 5a/8, 7a/8]$ such that the compression (or in its case, tension) measured during buckling could be reflected as discussed in Chapter 7. The second line of strain gauges (5-8) were along the middle of the plate in the y-direction at points $[b/4\ , b/2,\ 3b/4,\ \sim b]$, while still measuring the x-direction strains to plot the moment from the applied corner load.

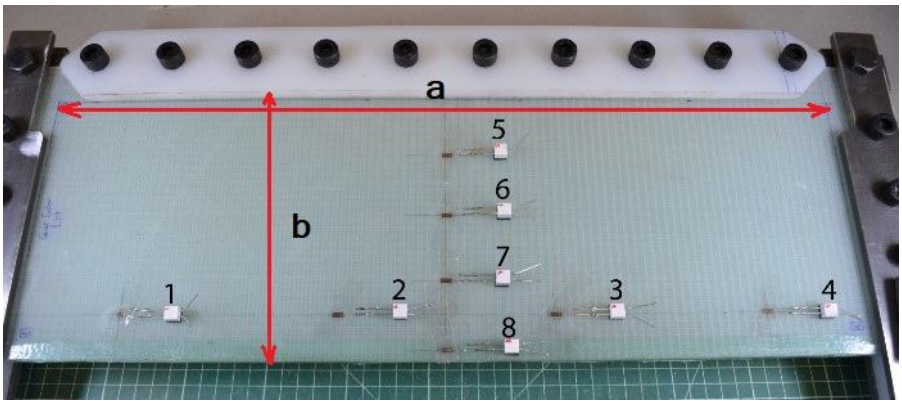

Figure 5.12 - Mounted bonded plate with strain gauge numbering.

5.3.2 Test Set-Up

Once the specimens were equipped with strain gauges and mounted tightly into the clamp, the clamp was attached to a $100\ kN$ compression machine. The set-up is shown in figure 5.13. The machine operated with a rising piston (1) at a speed of $4\ mm/min$. Eight data channels from the strain gauges were plugged into the computer (5), as well as a camera recording the progression of the buckling wave (2).

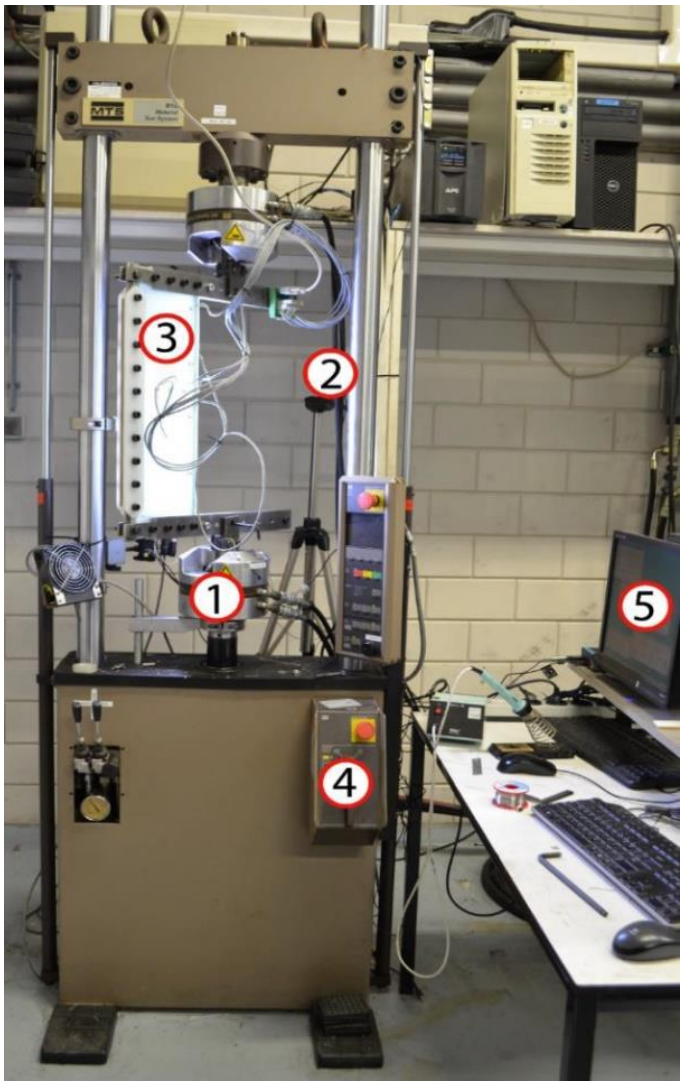

1) Machine compression die: Set up at a speed of 4mm/min of compression.
2) Camera: Positioned perpendicularly to the free edge for recording of the buckling shape.
3) Test specimen: TEB01, TEB02, TEB03 specimens were tested. TEB03 is currently mounted on the first clamp iteration.
4) Machine control: Manual control for pre-mounting of clamp and unloading after test.
5) Computer capturing test data.

Figure 5.13 - Test set-up.

Four tests were carried out: Specimen TEB03 was tested twice, the first time with the nylon/steel posterior clamp as can be observed in figure 5.13. After the nylon pieces were remade with steel, TEB03 was tested once more, to check the effects that plastic deformation from the previous test had on the specimen. TEB01 and TEB02 were subsequently tested with normal settings with the full steel posterior clamp. The test matrix is given below in table 5.4.

Test No.	Specimen	Test Speed	Posterior Clamp	Prebend
1	$TEB03$	$4mm/min$	Nylon/Steel	✗
2	$TEB03(b)$	$4mm/min$	Full Steel	✓
3	$TEB01$	$4mm/min$	Full Steel	✗
4	$TEB02$	$4mm/min$	Full Steel	✗

Table 5.4 – Test Matrix.

5.4 Output Data Processing – Filtering & Alignment

Every experiment provided a .buffer file with the following outputs for post-processing, which was measured at $100\ Hz$:

1) Strain Gauge 1	2) Strain Gauge 2	3) Strain Gauge 3	4) Strain Gauge 4
5) Strain Gauge 5	6) Strain Gauge 6	7) Strain Gauge 7	8) Strain Gauge 8
9) Applied Force	10)Displacement	11) Test time	12) Unixtime

Table 5.5 – Data outputs obtained from experimental tests.

Each test spanned around 10 minutes, yielding roughly 60,000 points of data which required to be filtered. Plotted raw data for all four tests can be observed in figure 5.14 below, with a zoom in area to show the unfiltered data. The filter was applied by grouping data from strain gauges, force and displacement (1-10 from table 5.4) in bins spanning 100 measurements and retrieving the mean value. Filtered data is shown in figure 5.15.

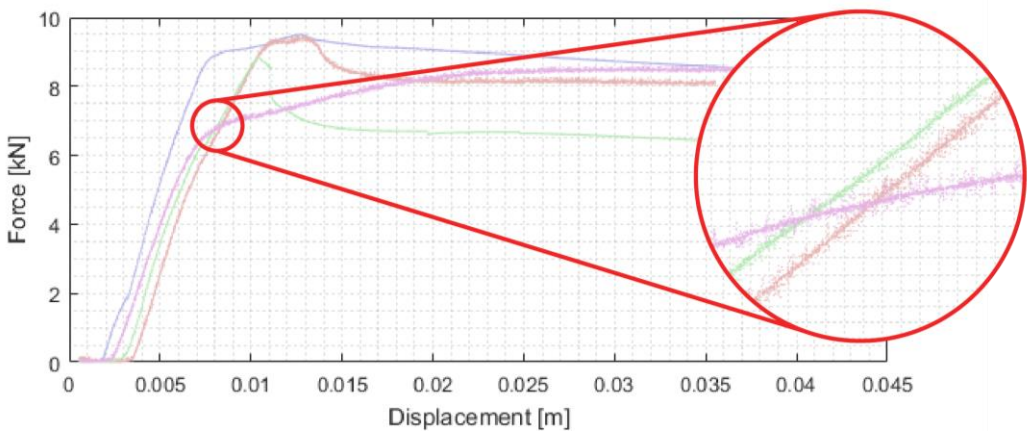

Figure 5.14 - Unfiltered test data.

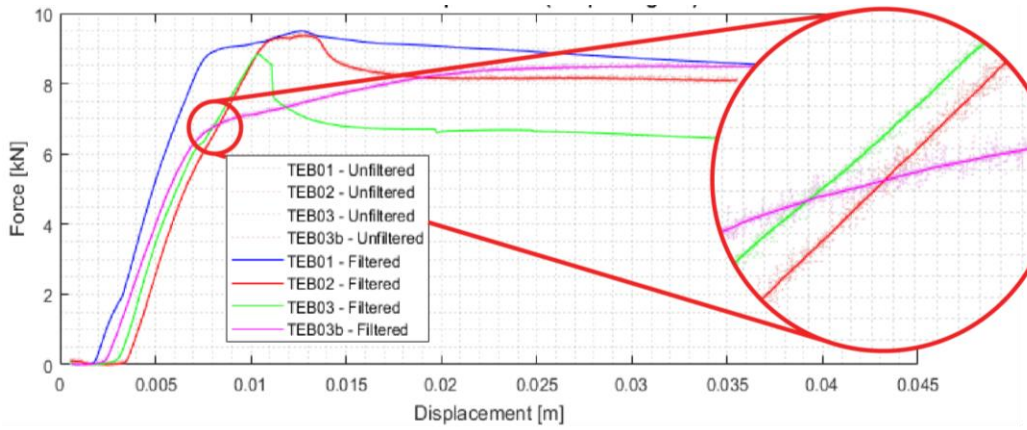

Figure 5.15 - Filtered test data.

Inspecting the filtered data, it can be observed that recording began prior to a precise zero-position for the press' compression piston, shown as a different zero-force initial displacement for every specimen. A minimal threshold force value was set (0.12kN) on the filtered data, deleting all the measurements below that threshold such that all plots could be aligned at the origin of the plot. A close up of the area and the threshold is shown in figure 5.16.

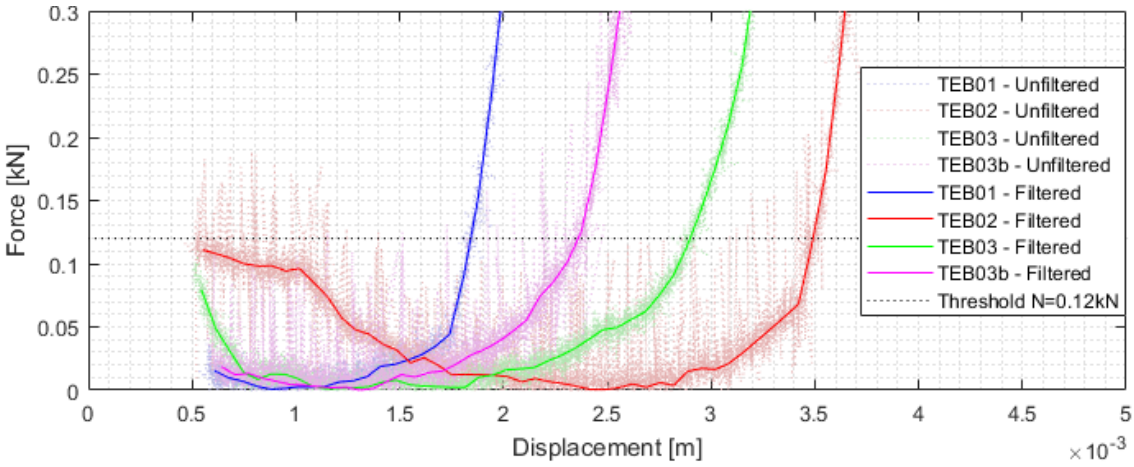

Figure 5.16 - Minimal threshold of N=0.12kN chosen to delete misalignment data from beginning of test recordings.

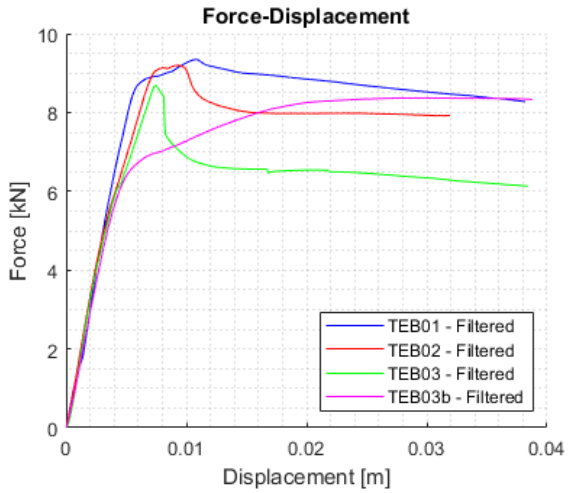

Figure 5.17 - Post-Processed Force-displacement data from 4 tests.

The data point for the zero-initial displacement was also applied to every other measurement for the strain gauges since these share zero-microstrains readings as seen in appendix G. Filtered and aligned data for the force-displacement curves of all tests is provided in figure 5.17 on the left. Four different tests are observable in the data plot. These will be explained in detail in chapter 7.2.

Chapter 6 – Numerical Modelling

The numerical modelling method is explained in this chapter. Firstly, a trade-off is made regarding the choice of element type and class in order to prevent shear locking/hourglass modes of the elements. A contact constraint table is given for the chosen contact bodies in the models to include the interaction between components from the experiments accurately. Next, the clamped boundary conditions from figure 3.12b (shown in figure 6.1b below) are applied to the models that will be compared to the experimental results, followed by a thorough mesh refinement study based on results from linear buckling and non-linear elastic analyses. Finally, several Finite Element models were created with varying parameters in order to draw the comparisons with the results from the semi-analytical and experimental methods. Firstly, simply supported boundary conditions are applied to the FE models to validate the semi-analytical results from the same boundary conditions. Aspect ratio, skew angle and imperfection are also modelled subsequently with clamped boundary conditions to compare with the experimental results. The FEM models will mimic in their best capacity the experimental set-up from Chapter 6. Results from these models will be discussed and compared to their semi-analytical and experimental methods in Chapter 7.

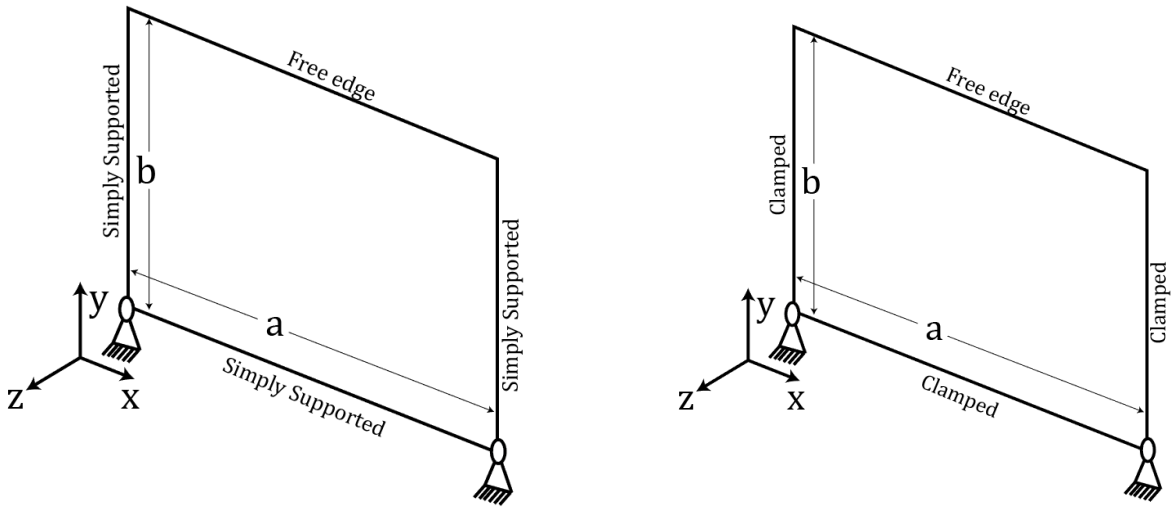

Figure 6.1a) Simply supported boundary conditions of FE models to compare and validate semi-analytical results. b) Clamped boundary conditions of FE model to validate effective length corrected results from semi-analytical model and joint fixity of experimental set-up.

6.1 MSC Marc Mentat Modelling

6.1.1 Element Type selection

Modelling the clamped composite plates with an adhesive line at the free edge was done using the MSC Marc Mentat 2016. Four different contact bodies are modelled: Steel clamps, adhesive line, top

composite facesheet and bottom composite facesheet, which are shown in figure 6.2. Table 6.1 gives the element type and class chosen for each of these contact bodies.

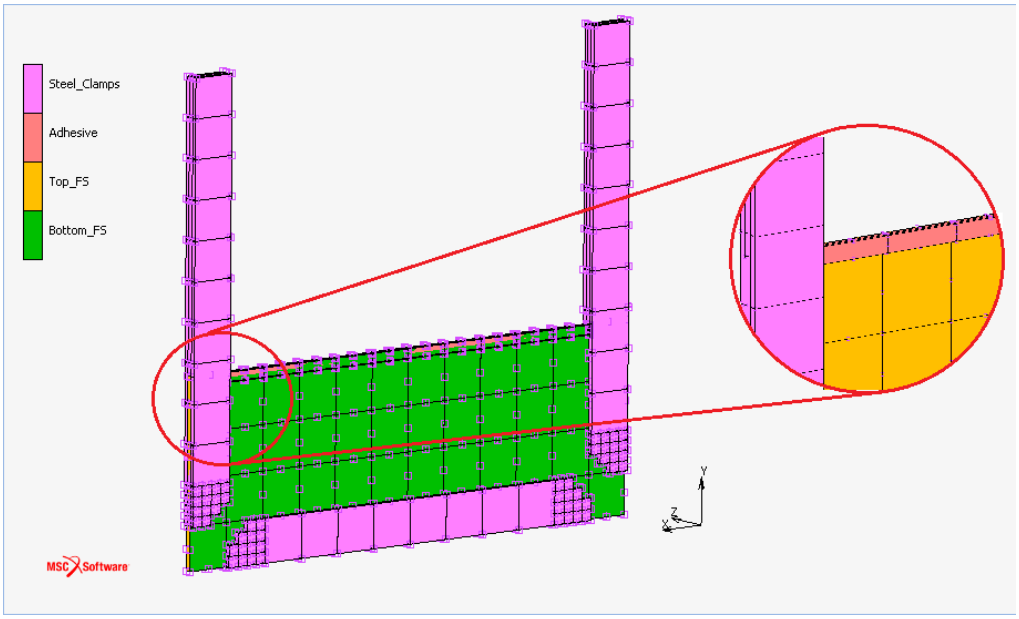

Figure 6.2 – FE model contact bodies for a plate of aspect ratio a/b=3 with close-up to adhesive line.

Contact Body 1	**Contact Body 2**	**Contact Body 3**	**Contact Body 4**
Steel clamps	Top Facesheet	Bottom Facesheet	Adhesive
Hex8 Type 117	Quad8 Type 22	Quad8 Type 22	Hex20 Type 21

Table 6.1 – Type of element chosen for every contact body in the FE models.

The selection criteria for the element type of each body is as follows:

Steel clamps: As steel clamps are an order of magnitude stiffer than the rest of the model components (steel $E = 200\ GPa$ vs composite $E_{11} = 26\ GPa$), Hex8 element was chosen for its low node-count requiring les computational power. Element type 117 is typically preferred for contact analysis, and its stiffness is calculated using one integration point at the centroid (figure 6.3) of the element and an additional consistent stiffness term to eliminate hourglass modes. Locking of these elements is not much of a concern as the results pertaining to the clamp elements are not of interest, as they only serve to introduce the load into the system.

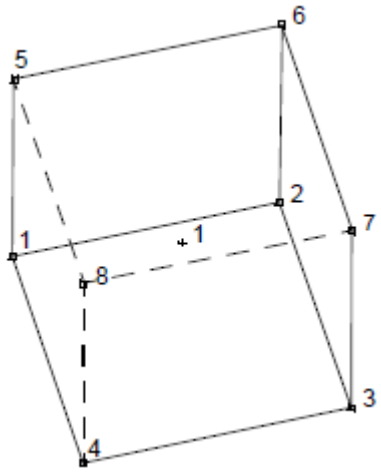

Figure 6.3 - Element 117 nodes (□) and integration point (+). Obtained from [36].

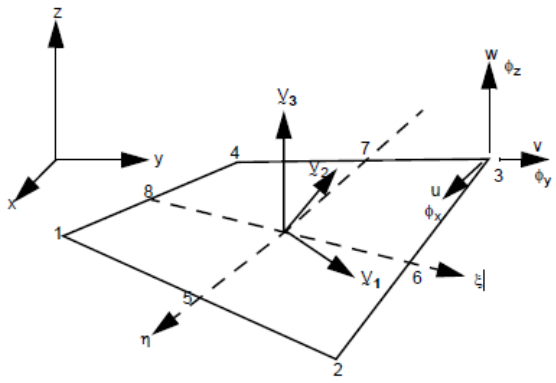

Figure 6.4 - Element 22 form and nodes. Obtained from [36].

Facesheets (Top & Bottom): The composite facesheets of the model were chosen to be Quad8 thick shell elements. Element type 22 (figure 6.4) uses second-order interpolation to retrieve coordinates, displacements – which in turn provide the membrane strain – and rotations which yield the respective curvatures. This element type may also behave accurately in the limiting scenario of thin shells due to how transverse shear strains are calculated.

Adhesive: The choice for the adhesive element type took more consideration due to the possibility of shear locking which would artificially stiffen the structure. As the adhesive line is situated at the edge of largest deformation of the system, a Hex20 solid element was chosen due to its higher node count. A trade-off was made pertaining the choice of element type among element types 57, 7 and 21. Element 57 (figure 6.5b,c) uses a triquadratic interpolation function integrated using eight points for a Gaussian quadrature, which yields very accurate results of the strain field; this element however may exhibit hourglass modes. Element type 7 was referred to by the MSC Marc user manual from element 57 as superior in contact analyses (figure 6.5a). However, this element type belongs to Hex8 elements which would require an even finer mesh. Furthermore, it provides poor shear/bending results [36]. Finally, element type 21, which is a 20-node (Hex20) element with full integration over 27 Gaussian points (figure 6.5b,d) provides accurate shear/bending results without showing hourglass behavior. The additional computational time due to the higher node-count and full integration was acceptable, since overall the full model is not very large for which reason this element type was chosen for the adhesive.

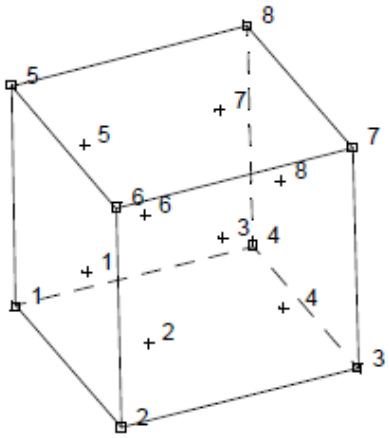

Figure 6.5a - Element 7 nodes (□) and gauss integration points (+). Obtained from [36].

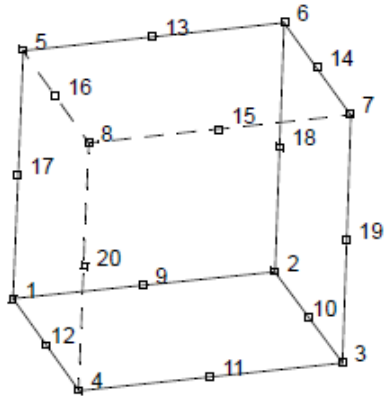

Figure 6.5b - Form and Nodes (□) of elements 21 and 57. Obtained from [36].

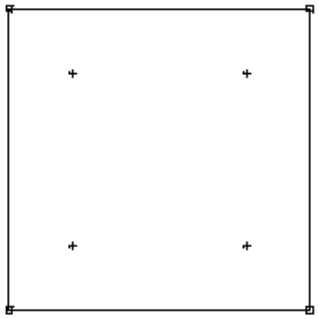

Figure 6.5c - Element 57 integration plane. Obtained from [36].

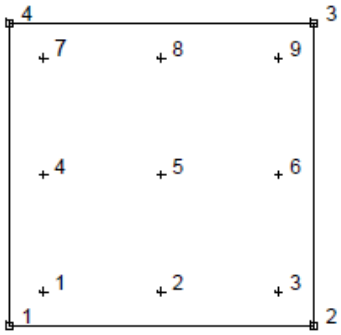

Figure 6.5d - Element 21 integration plane. Obtained from [36].

6.1.2 Materials, Dimensioning and Contact Table

The material properties chosen for the models are the ones given in the manufacturing section of Chapter 5, from tables 5.1 and 5.2. The steel's Young's modulus was set at $200\ GPa$ and its Poisson ratio at 0.26. The maximum length that the experimental testing rig allows (section 5.3) is around $0.6\ m$. This limited the plate's length to a maximum of $a = 0.5\ m$ and two sliding edge clamps of $5\ cm$ each. In the width-direction, there were no limitations. Due to the minimum aspect ratio to be modelled being $AR = 1$, the maximum width of the plate is $b = 0.5\ m$, as well as one static clamp of $5\ cm$ opposite of the free edge. A schematic of the base (unmeshed) model with the respective dimensions is given in figure 6.6 below.

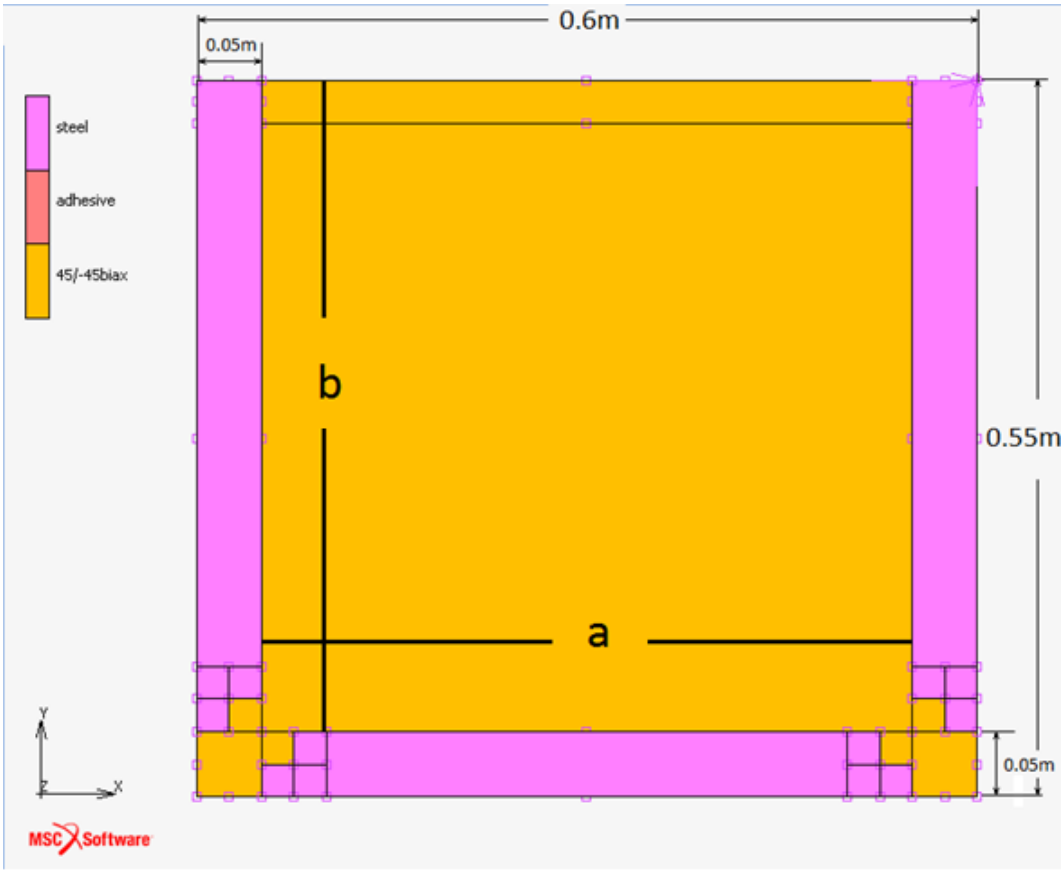

Figure 6.6 - XY-dimensions of Composite plates and steel clamps of FE models (unmeshed).

An important consideration for modelling the steel clamps was to prevent the sharing of nodes at the bottom corners, readily seen in figure 6.6, by the steel sections. This was done to allow the rotation during buckling to be determined by the composite facesheet's mechanical properties (table 5.1) and simulating the hinges to be added on the clamps during the experimental phase.

A transversal view of the adhesive/steel clamp is given in figure 6.7, determining the clamp thickness to be $5\ mm$. Even though the thickness of the steel clamps is somewhat irrelevant to the FE model due its stiffness being much higher than the rest of the elements, it was set at $5\ mm$ to remain consistent with the experimental clamp designed in Chapter 5. The adhesive is $6\ mm$ thick [6]. The adhesive width spans 1/15th of the width (b-dimension) of the plate in order to remain proportional to the dimensions established in figure 3.6. Note that, as the facesheets have been modelled as Quad8 elements, this view does not provide a thickness representation, but they are present in-between the clamps and adhesive. The facesheets were modelled as a 4-ply composite with the lay-up $[+45/-45/-45/+45]_s$ (figure 6.8) so as to keep consistent with the dimensions from [13], as well as being a straightforward manufacturing process as explained in Chapter 5.

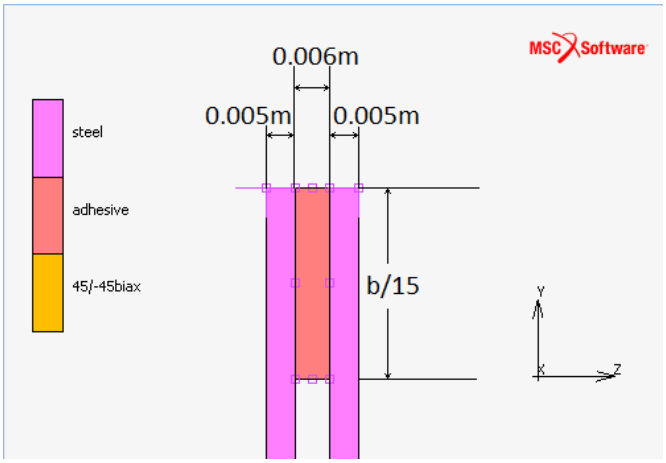

Figure 6.7 - Transversal YZ view of the clamp/adhesive dimensions.

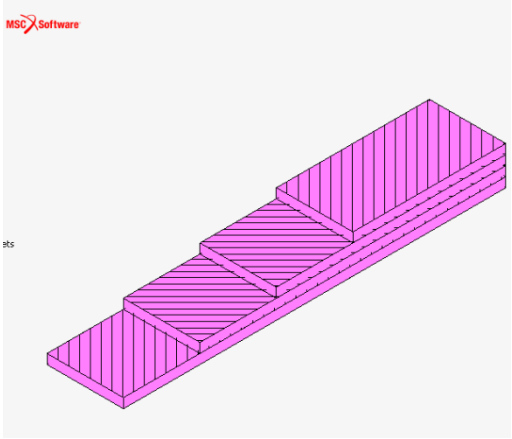

Figure 6.8 - Composite plies lay-up for facesheet material selection in FE model. Color not consistent with figure 6.7.

The four specified bodies in the model undergo certain interactions among themselves during the displacement and buckling process, and these interactions must be inputted as precisely as possible to better approximate the experimental response of the plate/clamp system and the desired clamped boundary conditions. Three different possible interactions are given:

G_{perma}: Permanent glue contact interaction is given among bodies that are expected to remain in perfect contact all throughout the modelling process. This contact constraint is only given between the steel clamps and facesheets. This is chosen instead of tie constraints between nodes, such that the mesh refinement between bodies and their element types can differ, while still maintaining the load transfer from the clamps into the facesheets.

G_{break}: Breakable glue is given for the contact between the facesheets and the adhesive line as well as between the adhesive elements themselves. This allows for the bodies to remain in contact until (and if) failure occurs.

T: Touching contact constraint is given to bodies that are either in initial contact or that may come into contact during displacement of the elements. This constraint is given between the steel clamps and adhesive (which are in initial contact in the experiment through the middle clamp piece) and between the top and bottom facesheets. Even though the facesheets are not in contact, their out-of-plane displacement may occur independently of each other and this constraint will prevent the elements from these bodies to intersect each other.

The contact constraint table (table 6.2) used in the FEA models is given below:

Contact Table Properties				
	Steel Clamps	Top Facesheet	Bottom Facesheet	Adhesive
Steel Clamps	-	G_{perma}	G_{perma}	T
Top Facesheet	G_{perma}	-	T	G_{break}
Bottom Facesheet	G_{perma}	T	-	G_{break}
Adhesive	T	G_{break}	G_{break}	G_{break}

Table 6.2 -Contact bodies interactions table employed in MSC Marc.

6.1.3 Boundary Conditions

A visual representation of the chosen boundary conditions is given below in figure 6.9. These boundary conditions were chosen to best approximate the real-life testing rig with additional constraints to prevent rigid body motion. Conditions 3 and 4 prevent out-of-plane displacement as well as rotations around the y- and x-axes respectively in order to avoid an initial displacement slope at the edge of the plate.

1) Load introduction: A point load is introduced at the nodes on the corner of the steel clamp opposite of the hinge end. The load is introduced with a ramp up from 0 to maximum ($15\ kN$) in 300 increments.
2) Counter support: Displacement is prevented in x- and y-directions on the steel clamp opposite to that where the load was introduced. This simulates the test machine static clamp. Additionally, rotation around the z-axis is prevented on this node to avoid rigid body motion.
3) Out-of-plane displacement (z-axis) and rotation (around y-axis) is applied to the nodes on the sliding edge clamps.
4) Out-of-plane displacement (z-axis) and rotation (around x-axis) is applied to the nodes on the steel clamp opposite of the free edge.
5) Due to the plate being modelled symmetrically and without imperfections, a small transversal (z-direction) load of $10\ N$ is applied at the mid-point node along the free-edge length to induce buckling.

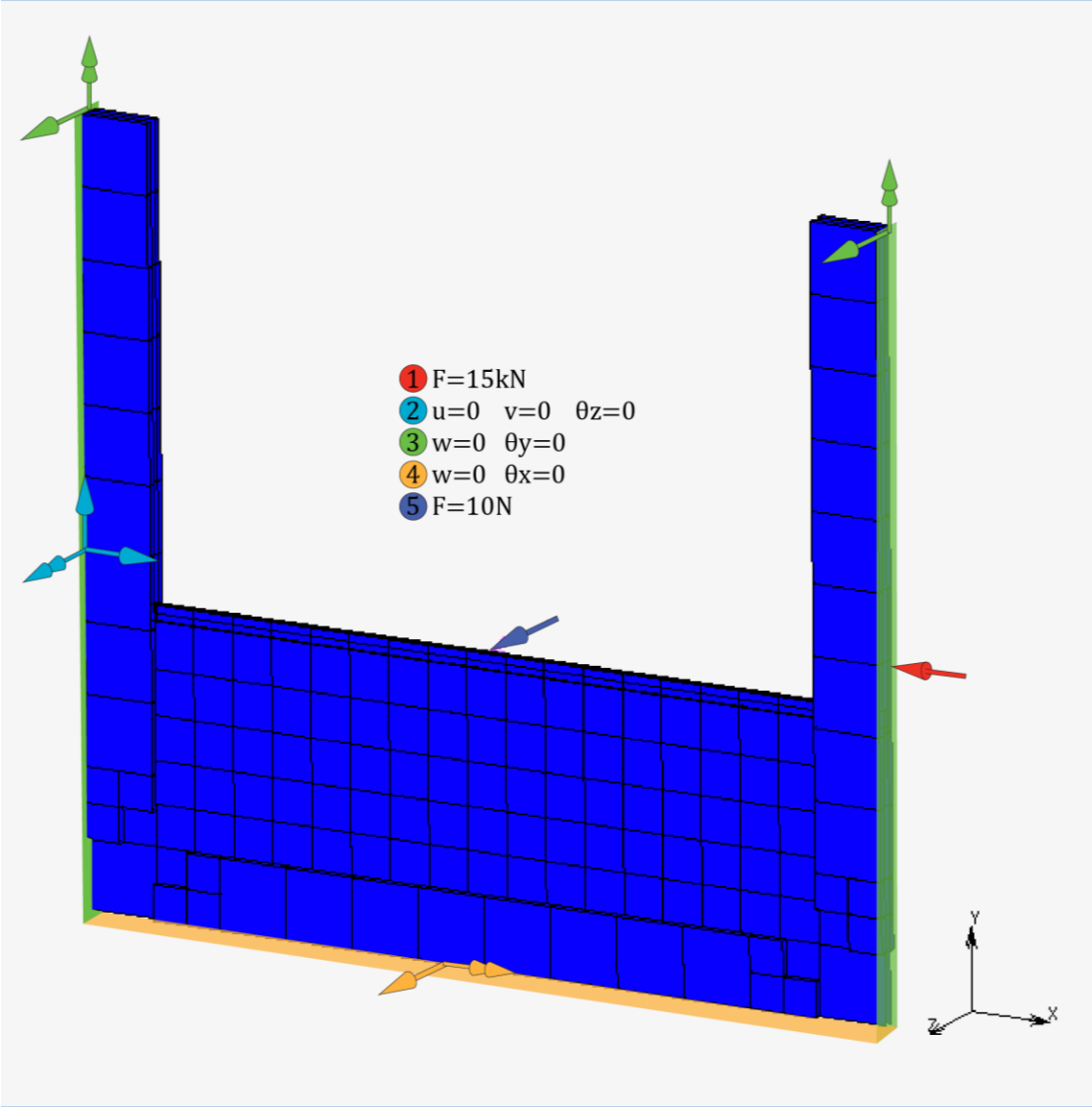

Figure 6.9 – Boundary conditions imposed on the FEA model on an arbitrary plate of aspect ratio a/b=3.

6.2 Mesh Refinement study

An important consideration is the effect of the mesh refinement on the convergence of the solution of the models. Figure 6.6 showed the base unmeshed model with a base aspect ratio of $a/b = 1$. As it was discussed in Chapter 5, the chosen aspect ratio for the experimental tests is $a/b = 3$ due to a trade-off between time taken during manufacturing and the maximum number of specimens obtainable from a single composite infusion. It is for this reason that the mesh refinement study is done on a resized base model of aspect ratio 3.

6.2.1 Linear Buckling Analysis Convergence Study

Two different element sizes are studied: Element size for facesheets and adhesive on the xy-plane and adhesive element through-thickness. Table 6.3 below provides the following information: The first column is the element grid (number of elements along a x number of elements along b) chosen for the facesheets and the general element size between parentheses. On the second column the adhesive through thickness is given, obtained by subdividing the solid adhesive elements with initial thickness of $0.6\ cm$ by 2, 3 and 4 respectively. The third and fourth columns give the total number of elements and nodes respectively. A general buckling load for each mesh size was obtained through a linear eigenvalue buckling load case, shown in the fifth column. While a linear eigenvalue buckling load case does not provide insight into the force-displacement relationship of the plate, it can output its bifurcation load (eigenvalue) as well as its eigenvector in the form of the modal displacement.

Element grid (general size)	Adhesive through-thickness	No. of Model Elements	No. of Model Nodes	Buckling Load	Difference
$10x3\ (5\ cm)$	$0.3\ cm$	176	827	$12.87\ kN$	–
$12x4\ (4\ cm)$	$0.3\ cm$	220	997	$12.43\ kN$	3.54%
$17x7\ (3\ cm)$	$0.3\ cm$	382	1580	$11.84\ kN$	4.98%
$25x10\ (2\ cm)$	$0.3\ cm$	676	2610	$11.70\ kN$	1.19%
$50x20\ (1\ cm)$	$0.3\ cm$	2370	8257	$11.25\ kN$	4%
$10x3\ (5\ cm)$	$0.2\ cm$	186	902	$12.47\ kN$	–
$12x4\ (4\ cm)$	$0.2\ cm$	232	1086	$12.01\ kN$	3.83%
$17x7\ (3\ cm)$	$0.2\ cm$	399	1704	$11.41\ kN$	5.25%
$25x10\ (2\ cm)$	$0.2\ cm$	701	2790	$11.24\ kN$	1.51%
$50x20\ (1\ cm)$	$0.2\ cm$	2420	8514	$10.97\ kN$	2.46%
$10x3\ (5\ cm)$	$0.15\ cm$	196	977	$12.13\ kN$	–
$12x4\ (4\ cm)$	$0.15\ cm$	244	1175	$11.72\ kN$	3.49%
$17x7\ (3\ cm)$	$0.15\ cm$	416	1828	$10.92\ kN$	7.32%
$25x10\ (2\ cm)$	$0.15\ cm$	726	2970	$10.82\ kN$	0.92%
$50x20\ (1\ cm)$	$0.15\ cm$	2470	8771	$10.8\ kN$	0.18%

Table 6.3 – Mesh refinement study for a variety of general element size, adhesive element thickness, node/element count and predicted buckling loads.

The last column of table 6.3 gives the respective differences in buckling load as the adhesive through-thickness is reduced. The buckling loads for all combinations of element size and adhesive thickness are plotted in figure 6.10a against the general element size and in figure 6.10b against the number of elements. Figure 6.10b shows that for an adhesive thickness of $0.3\ cm$ and $0.2\ cm$, the convergence is increasingly delayed when compared to the smallest adhesive thickness of $0.15\ cm$. This demonstrates the need for a fine mesh through the adhesive, for which reason, only an adhesive thickness of $0.15\ cm$ will be considered.

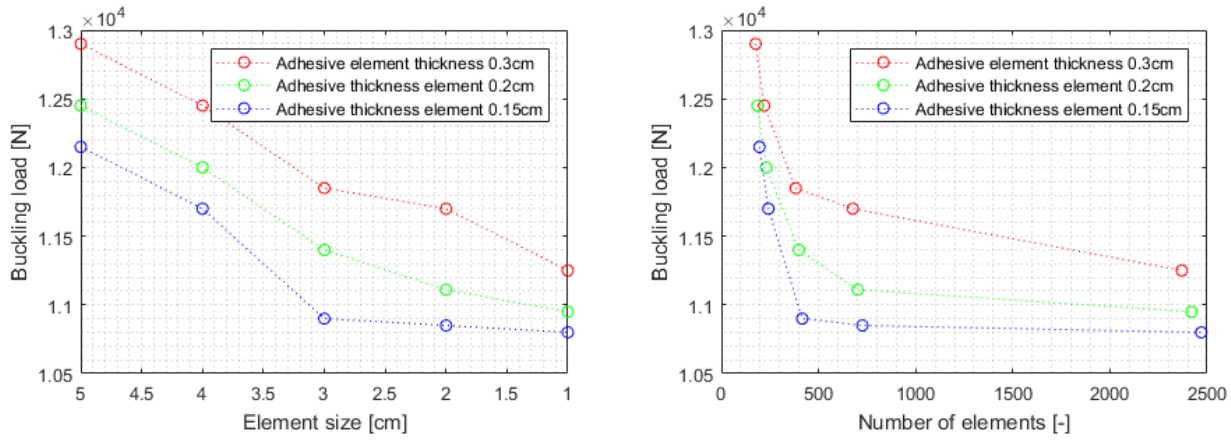

Figure 6.10 – Left a) Buckling load vs general element size. Right b) Buckling load vs element number count to show convergence.

Following the rule of thumb stating that convergence is reached when doubling the elements does not change the solution by more than 5%, the convergence as the general element size decreases is shown in table 6.4:

Element grid (general size)	Adhesive through-thickness	No. Of Model Elements	Element increase factor	Buckling load	Difference
$12x4\ (4\ cm)$	$0.15\ cm$	244	$\frac{416}{244} = 1.7$	$11.72\ kN$	7.32%
$17x7\ (3\ cm)$	$0.15\ cm$	416		$10.92\ kN$	
$17x7\ (3\ cm)$	$0.15\ cm$	416	$\frac{726}{416} = 1.75$	$10.92\ kN$	0.92%
$5x10\ (2\ cm)$	$0.15\ cm$	726		$10.82\ kN$	
$25x10\ (2\ cm)$	$0.15\ cm$	726	$\frac{2470}{726} = 3.4$	$10.82\ kN$	0.18%
$50x20\ (1\ cm)$	$0.15\ cm$	2470		$10.8\ kN$	

Table 6.4 – Mesh convergence for decreasing element size for a constant adhesive thickness of 0.15cm.

Decreasing the element size from $4\ cm$ to $3\ cm$ shows that there still exists a difference of roughly 7%. Even though the elements are not doubled and there exists a possibility that a difference of 5% may be reached if a finer mesh is imposed at the free-edge, the element size of $3\ cm$ will not be considered. Further reduction to a size of $2\ cm$ shows that a difference of less than 1% is reached without even doubling the elements. A final refinement down to a size of $1\ cm$ shows minimal improvements in convergence, down to a mere 0.18%.

6.2.2 Non-Linear Elastic Convergence Study

Additional to the linear buckling analysis, a non-linear static analysis was carried out for each mesh size from which a force-displacement curve could be extracted to have an improved visualization of the convergence. Figure 6.11 shows the position of node (147) on the corner of the plate from which

displacement is measured and the node where half of the load is introduced (298). Node 147 is chosen because it is the point where the free-end shortening (u-displacement) will attain its maximum.

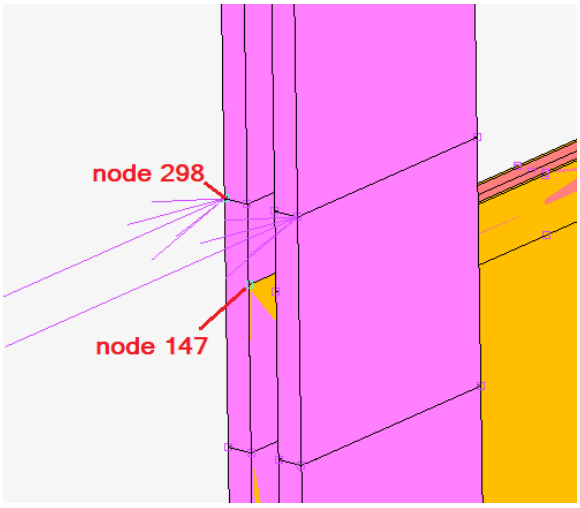

Figure 6.11 - Node 298 on steel clamp where half of the load is introduced. Node 147 at the corner of the plate that measures free-edge shortening.

In the non-linear load case, it is more complex to determine the buckling load of the structure as the simulation does not return the eigenvalue of the stiffness matrix. Instead, to illustrate the buckling point in a non-linear analysis more robustly than just a visual inspection, the reduction in stiffness is obtained from the load-displacement curve. This can be done by obtaining the tangent stiffness at every load increment of the curve by using equation 6.1 below. The tangent stiffness will not deviate much from the initial stiffness $E(1)$ as load increases prior to buckling, remaining under an arbitrary threshold ϵ. At a given point n the change of stiffness $\Delta E(n)$ (equation 6.2) will surpass the threshold, indicating that buckling was reached. For the purpose of the convergence study, the loads $N(n)$ that promote a reduction of stiffness $\Delta E(n)$ above a threshold of $\epsilon = 15\%$ are obtained.

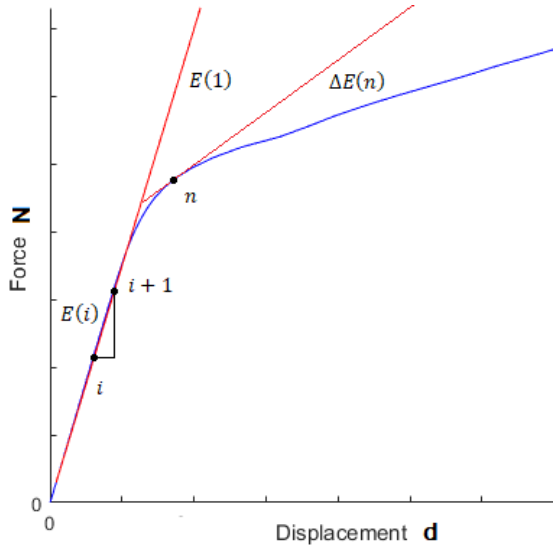

$$E(i) = \frac{N(i+1) - N(i)}{d(i+1) - d(i)} \qquad (5.1)$$

$$\Delta E(n) = \frac{E(n) - E(1)}{E(1)} x100 \qquad (5.2)$$

Figure 6.12 - Tangent stiffness of the FE model from non-linear elastic analysis to determine a standard point of loss of stiffness.

The load-displacement curves in figure 6.13(a-e) are shown for each respective general element size for varying adhesive elements through-thickness, whereas figure 6.13f shows the force-displacement of node 147 for all element sizes with an adhesive thickness of $0.15\ cm$ as it was chosen earlier in this section. Table 6.5 gives the loads where the loss of stiffness surpasses the chosen threshold, and the improvement in convergence given in % respective to the element size/adhesive thickness of the previous row:

Element grid (general size)	Adhesive through-thickness	$N(n)$	Difference
$10x3\ (5\ cm)$	$0.3\ cm$	$12.75\ kN$	–
$12x4\ (4\ cm)$	$0.3\ cm$	$12.3\ kN$	3.52%
$17x7\ (3\ cm)$	$0.3\ cm$	$11.85\ kN$	3.65%
$25x10\ (2\ cm)$	$0.3\ cm$	$11.55\ kN$	2.53%
$50x20\ (1\ cm)$	$0.3\ cm$	$11.25\ kN$	2.59%
$10x3\ (5\ cm)$	$0.2\ cm$	$12.3\ kN$	–
$12x4\ (4\ cm)$	$0.2\ cm$	$11.85\ kN$	3.66%
$17x7\ (3\ cm)$	$0.2\ cm$	$11.25\ kN$	5.06%
$25x10\ (2\ cm)$	$0.2\ cm$	$11.1\ kN$	1.33%
$50x20\ (1\ cm)$	$0.2\ cm$	$10.89\ kN$	1.89%
$10x3\ (5\ cm)$	$0.15\ cm$	$11.7\ kN$	–
$12x4\ (4\ cm)$	$0.15\ cm$	$11.25\ kN$	3.84%
$17x7\ (3\ cm)$	$0.15\ cm$	$10.8\ kN$	3.99%
$25x10\ (2\ cm)$	$0.15\ cm$	$10.65\ kN$	1.34%
$50x20\ (1\ cm)$	$0.15\ cm$	$10.62\ kN$	0.3%

Table 6.5 – Mesh convergence for decreasing element sizes with constant adhesive element thickness.

Similarly to the linear buckling convergence study, the difference in critical load as the mesh is refined is given in table 6.5 above.

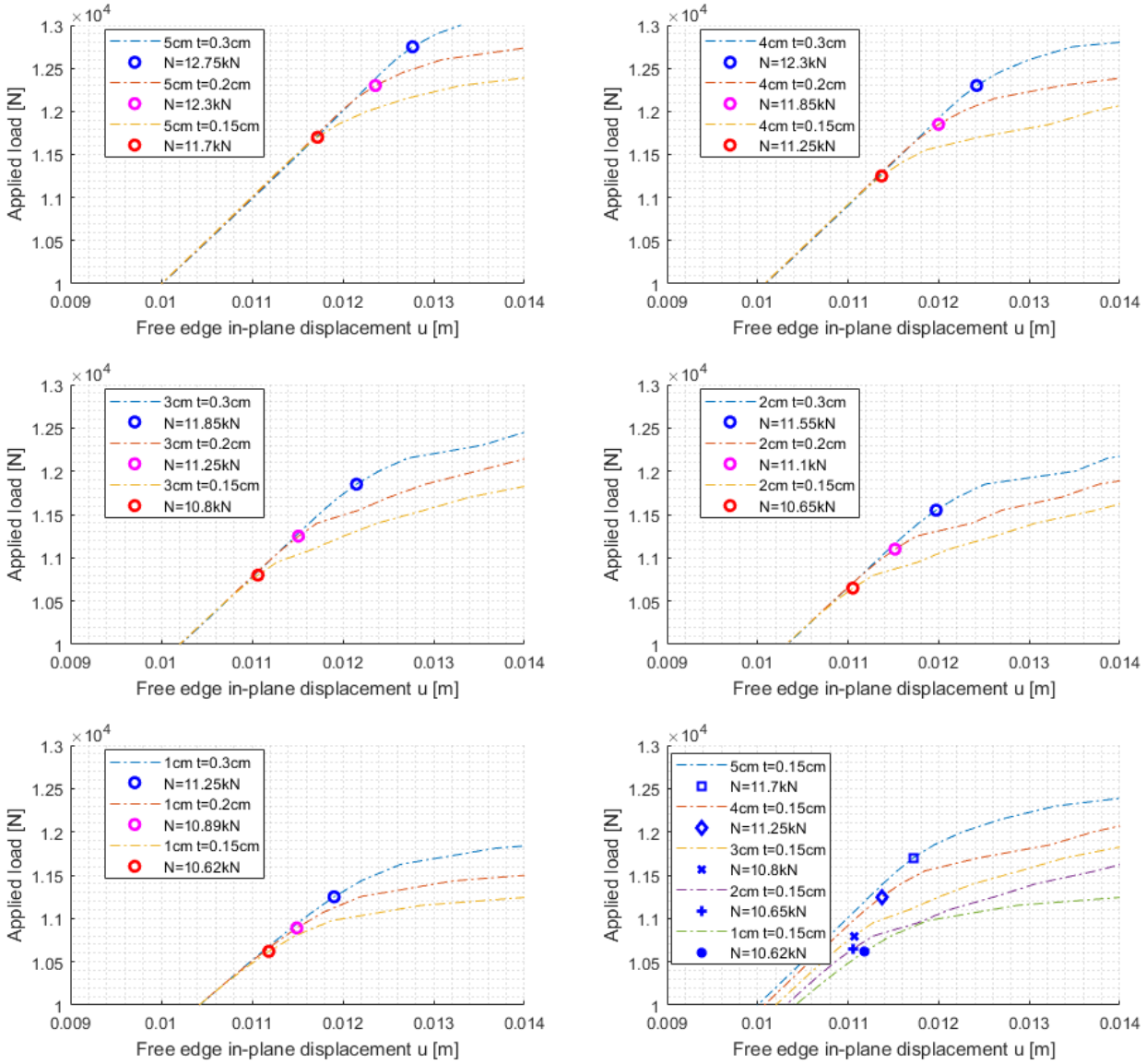

Figure 6.13 – Load-displacement curves of chosen refinement element sizes and thicknesses. Top left a) General element size 5 cm. Top right b) General element size 4 cm. Center left c) General element size 3 cm. Center right d) General element size 2 cm. Bottom left e) General element size 1 cm. Bottom right f) Load-displacement curve for all general element sizes (5 cm,4 cm, 3 cm, 2 cm, 1 cm) whilst keeping adhesive element thickness equal at 2mm.

Despite the fact that these results are dependent on the load increment size chosen for the analysis, the results seem to have converged in the vicinity of $N \approx 10.65 - 10.62\ kN$ for element sizes $2\ cm$ and $1\ cm$. The fact that the FE analysis is not done for overly complex structures yields a low node and element count even for the finest mesh combination of $1\ cm/0.15\ cm$ (figure 6.14). This mesh yields results within an acceptable time even for the more computationally intensive non-linear elastic analysis and thus that will be the mesh employed for the remainder of the research.

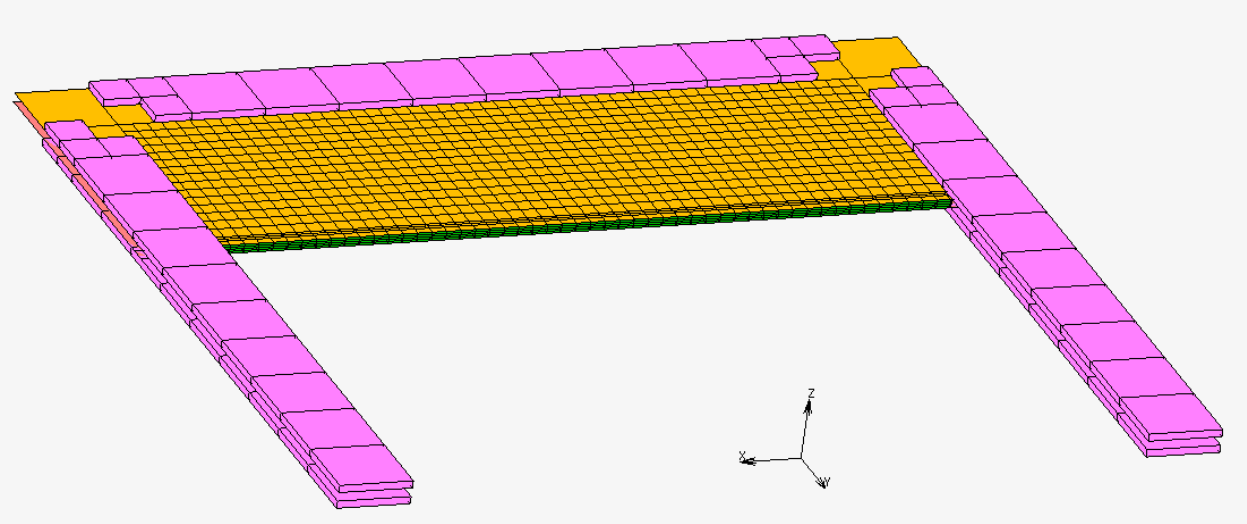

Figure 6.14 – Final refined mesh for the plate FE models.

6.3 Plate models

Since the scope of the research of the buckling plates spans various geometric dimensions, several FE plate models were created to carry out a parametric study of their effect on the buckling behavior. Firstly, simply supported straight plates with various aspect ratios were modelled to validate the semi-analytical solution for the same boundary conditions. The same was done for plates with clamped edges with the presence of the steel hinged clamp system designed in Chapter 5. Next, clamped plates with skew skew angles were modelled. Finally, twisted and prebent plates of the base model plate with aspect ratio 3 were made. These modelling variations are explained in the following subsections, and the results on the buckling loads and displacements are compared to the semi-analytical and experimental methods in Chapter 7.

6.3.1 Clamped, Straight (Unskewed) Plates

Varying the aspect ratio of straight plates was done to cover a realistic span of aspect ratios that could be tested experimentally in the custom designed clamp. As explained in Chapter 5, the maximum allowable plate length that could fit the compression machine is $0.5\ m$. As such, the width of the plate was varied to achieve 9 different aspect ratios. Dimensions respective to each aspect ratio are given in table 6.6 below.

	$AR = 1$	$AR = 1.5$	$AR = 2$	$AR = 2.5$	$AR = 3$	$AR = 3.5$	$AR = 4$	$AR = 4.5$	$AR = 5$
a	$0.5\ m$	$0.5\ m$	$0.5\ m$	$0.5\ m$	$0.5\ m$	$0.5\ m$	$0.5\ m$	$0.5\ m$	$0.5\ m$
b	$0.5\ m$	$0.33\ m$	$0.25\ m$	$0.2\ m$	$0.166\ m$	$0.142\ m$	$0.125\ m$	$0.111\ m$	$0.1\ m$

Table 6.6 – Aspect ratio range and specific plate length a and width b.

Refer to figure 6.6 for a visual representation of dimensions a and b. Note that only facesheets and adhesive were resized, unlike the clamps.

6.3.2 Simply Supported, Straight (Unskewed) Plates

Chapter 4 proposed a formulation for the plate buckling problem which can be solved for simply supported boundary conditions, or alternatively employing the concept of effective length. A first step to validate the semi-analytical model is to compare the results from the simply-supported solution to FE plates that possess the same boundary constraints. A re-definition of the boundary conditions from figure 6.9 is given below (figure 6.15) with the simply supported FE boundaries. Notice that the steel elements that simulated the experimental clamping system have been taken out, as these provide artificial bending stiffness to the model which would not be considered by the semi-analytical solution. The aspect ratios modelled are the same as those from table 6.6 for clamped boundaries.

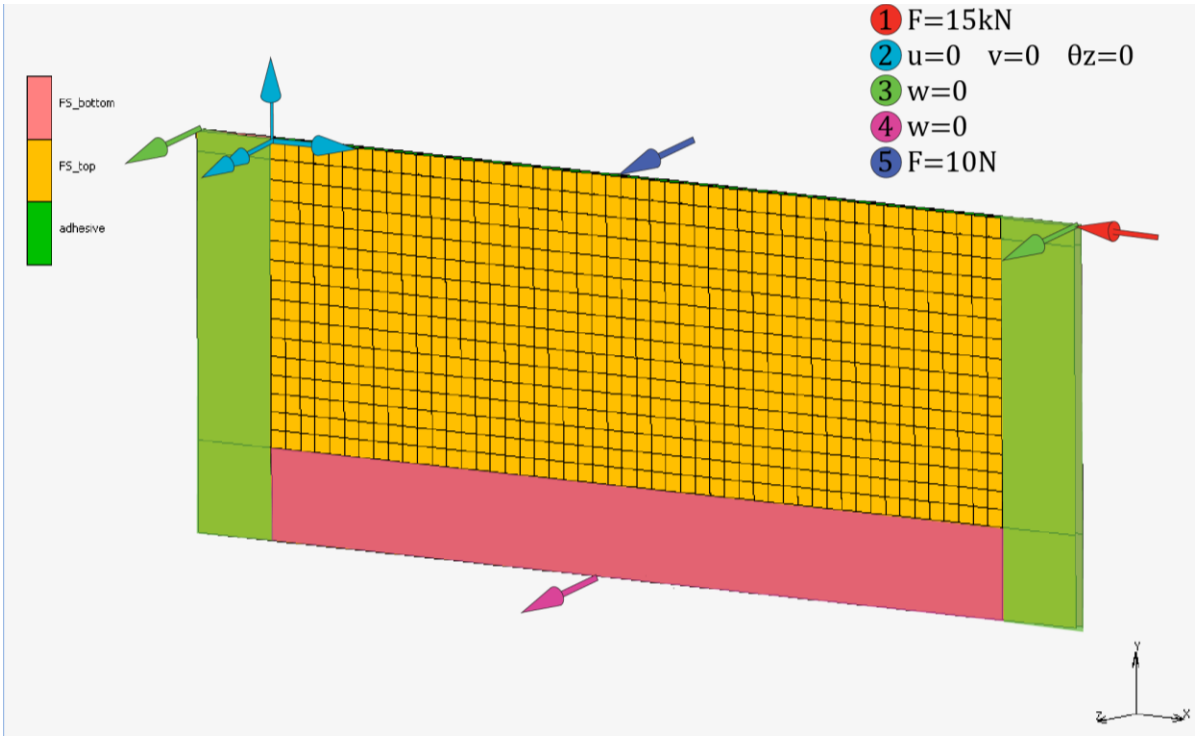

Figure 6.15 - Simply supported boundary conditions of FE (un-skewed) FE models without the presence of clamps.

6.3.3 Skewed plates

Skew angles of $\Psi = 5°$ and $\Psi = 10°$ were imposed on the five plates with aspect ratio 1,2,3,4 and 5 in the same way that it was proposed in Chapter 3. A visual representation of the skew on the FE models is given below in figure 6.16.

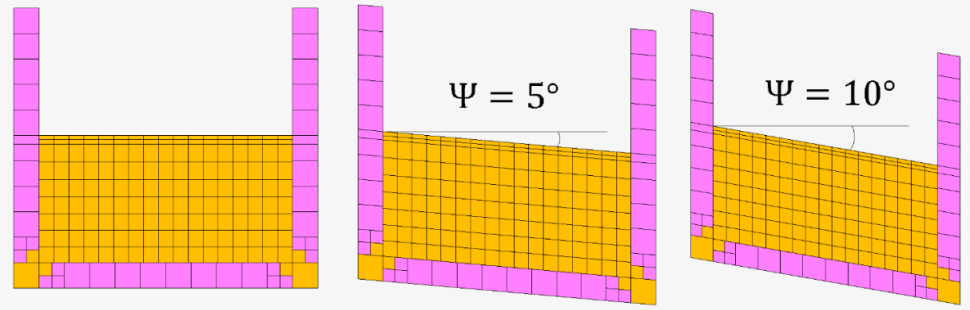

Figure 6.16 -Depiction of skew angle imposed on FE models; only shown for aspect ratio 2.

6.3.4 Twist as corner imperfections

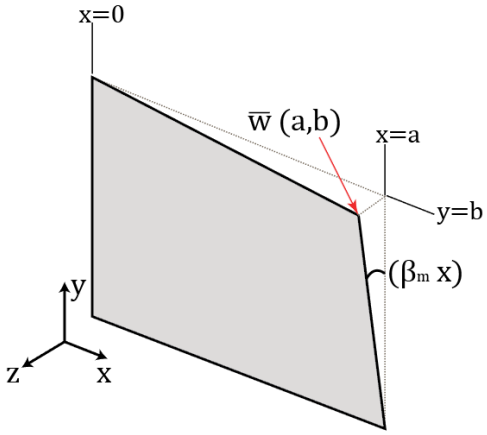

Figure 6.17 – Twisted plate displacement according to the plate's frame of reference.

Once more, referring to Chapter 2 and the inclusion of the twist as an initial imperfection, the plate will be undergoing an out-of-plane rotation over an angle β_m at the bottom right corner (coordinates $x = a, y = 0$) such that a displacement field $\overline{w}(x, y)$ can be imposed with the form:

$$\overline{w}(x, y) = y \sin(\beta_m x) \tag{3.37}$$

6.3.5 Pre-bent imperfection

During the experimental testing, the first design of the clamping system had insufficiently stiff materials and the clamp opposite to the free edge of the plate also began to buckle. On releasing the specimen, it was noticed that it had undergone plastic deformation and did not spring back to the initial shape. This brought up the opportunity to design an additional FE model with a pre-bent shape. Inspecting the free edge of the pre-bent specimen it was determined that the maximum amplitude of the initial displacement was around 3mm, observable in figure 6.18 where the top facesheet of the plate surpasses the straight red line from clamp to clamp. This displacement was then also imposed on the FE model of $AR = 3$; figure 6.19 shows the pre-bent of the FE model, where clamps have been hidden to improve visibility.

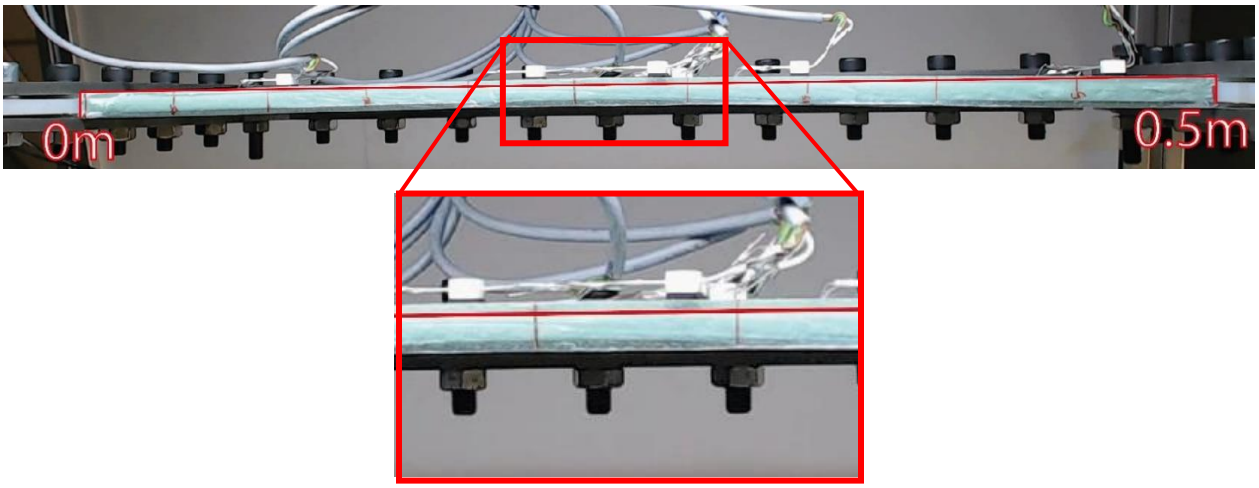

Figure 6.18 - Free-edge pre-bend due to plastic deformation of experimental specimen with a maximum amplitude of roughly 3mm.

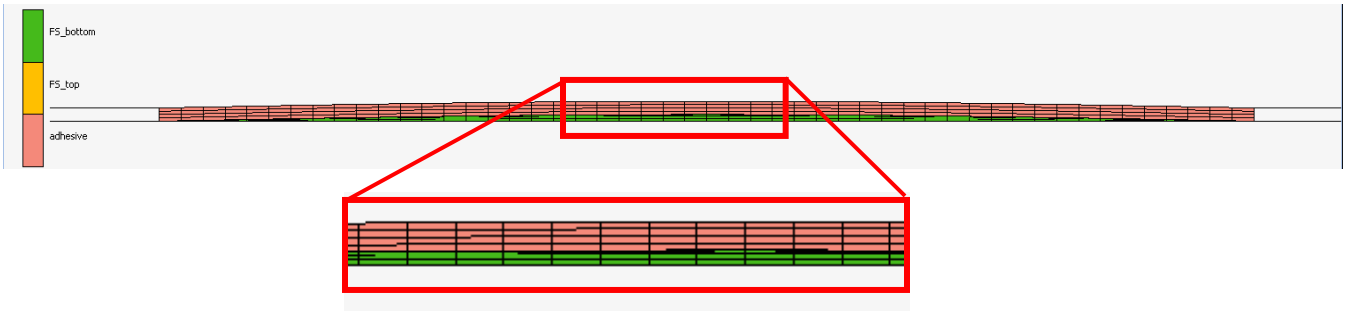

Figure 6.19 - Free-edge pre-bend imposed on FE model with a maximum amplitude of 3mm.

Chapter 7 – Results

The results from the three methods (semi-analytical, numerical and experimental) are presented within this Chapter. However, the loading conditions on each method differed: the semi-analytical tool yields a critical distributed load along the sliding edges of the plate. On the other hand, the numerical and experimental methods buckled under a point load applied on the steel clamp at a variable distance from the hinge, dependent on the aspect ratio chosen. An approach to transfer the loading to a single point corner load is given so that a direct comparison can be made among the results.

Subsequently, the results for the semi-analytical and numerical sections are presented. The expected buckling loads vs. aspect ratio of the semi-analytical model are given and plotted against the numerical ones for both the simply-supported and clamped cases. A section for the effects of both initial imperfections (twist and pre-bend) demonstrates the similarities and differences between the semi-analytical and numerical approaches. Next, the effects of the skew angle obtained from the FE models are presented.

Finally, the experimental results for the force-displacement curves and buckling loads are given and compared to the numerical results. The joint-fixity of the experimental set-up is discussed through the load-displacement and strain plots. Strain gauge data from the experiments is also compared against strain data extracted from nodes of the FE models both giving insight into the pre-buckling strains and edgewise moment loading that the plates experience.

7.1 Load Transfer to Single Point Corner Load

In order to provide an acceptable comparison of the results for all three methods, the loading conditions for the semi-analytical, numerical and experimental sections must be brought in-line with each other.

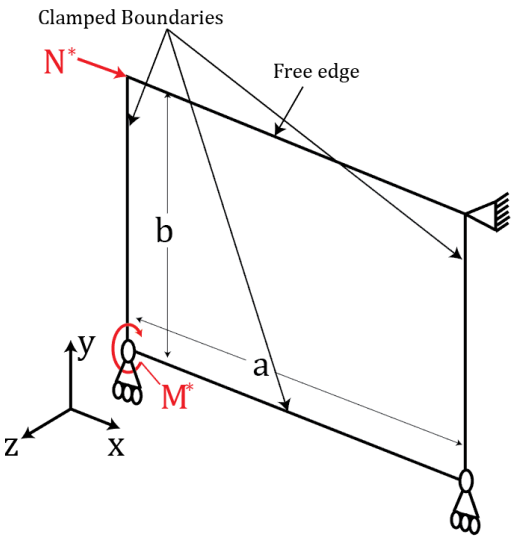

Figure 7.1 - Loading and boundary conditions of idealized case for comparison of buckling loads N.*

An idealized case where the point of application of the load N^* is at the corner of the plate with coordinates $x = 0, y = b$ inducing a moment M^* is shown in figure 7.1.

$$M^* = N^* b \tag{7.1}$$

The results from the semi-analytical and numerical models as well as the experimental tests will be related back to this ideal case such that a comparison of the buckling loads can be made.

7.1.1 Semi-Analytical

Firstly, the semi-analytical model buckling load solution is given in terms of a distributed load along the sliding edges N_{s-a} in $[N/m]$, inducing a buckling moment M_{s-a} at each hinge. Equation 7.2a gives the buckling moment derived from the fact that a distributed load exerts a moment acting at the mid-point or centroid of the distribution, therefore acting with a moment arm of $b/2$. Figure 7.2 demonstrates that the plate is buckling under two moments M_{s-a}, each located at the hinges. However, since facesheets were modelled individually, two additional moments M_{s-a} are located on the other plate not pictured in figure 7.2. This amounts to a total buckling moment of $4M_{s-a}$.

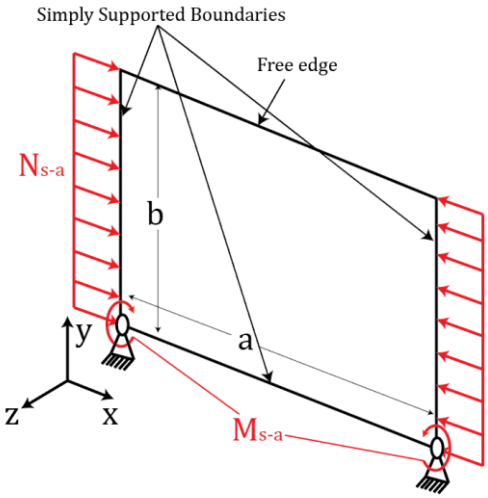

Figure 7.2 – Loading conditions of semi-analytical model.

$$M_{s-a} = N_{s-a} b \cdot \frac{b}{2} = \frac{N_{s-a}\, b^2}{2} \tag{7.2a}$$

Equating the four contributions of the distributed loads on the buckling moment from the semi-analytical model to the idealized case from figure 7.1 and solving for the corner point load yields the correction factor 7.2b:

$$M^* = 4M_{s-a} \rightarrow N^* b = 4\frac{N_{s-a}\, b^2}{2}$$

$$N^* = 2N_{s-a} b \tag{7.2b}$$

7.1.2 Numerical & Experimental

For both the numerical models and the experimental set-up, the load was not introduced directly at the plate's corner of the free edge. Instead, the load was applied on the steel clamp at a variable distance c. The load on the FE models was applied at the node of the clamp closest to the free edge as it was shown in figures 6.9 and 6.11, and now in figure 7.3.

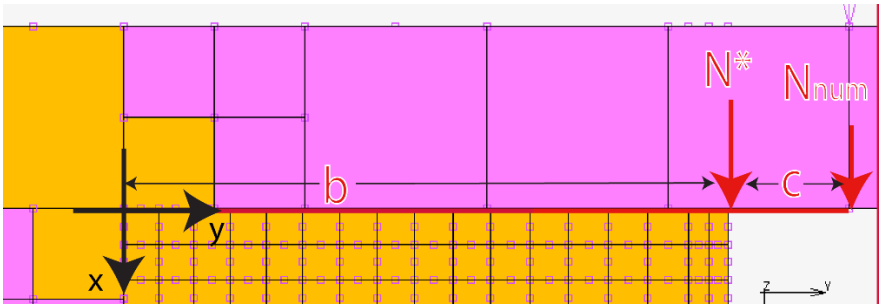

Figure 7.3 – Load N_{num} application node at distance $(b + c)$ from plate's origin.

Figure 7.4 shows the same scenario but for the experimental tests. In order to ensure a tight clamp during experimentation, the overhead hinge could not be placed at the point closest to the plate's corner. All four screws along the plate's edge shown in figure 7.4 had to be tightened to ensure proper load introduction.

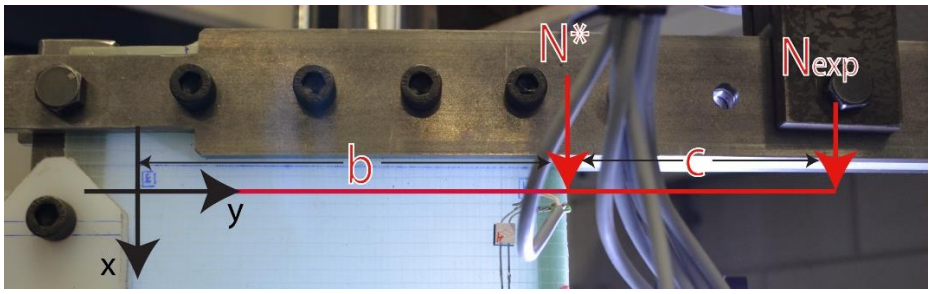

Figure 7.4 - Test load application N_{exp} and arm length (b+c) for experimental set-up.

Table 7.1 gives the distance c from all aspect ratios of the FE models as well as the experimental set-up.

	FE									Exp
AR	1	1.5	2	2.5	3	3.5	4	4.5	5	3
$c\ [cm]$	0	1.67	0	0	3.33	0.71	2.5	3.8	0	10

Table 7.1 – Load application distance c from plate's free edge corner from FE and experimental set-up.

Both cases can be presented with figure 7.5 below. The buckling moments M_{num} and M_{exp} can simply be expressed as a factor of the load by the arm length $(b + c)$.

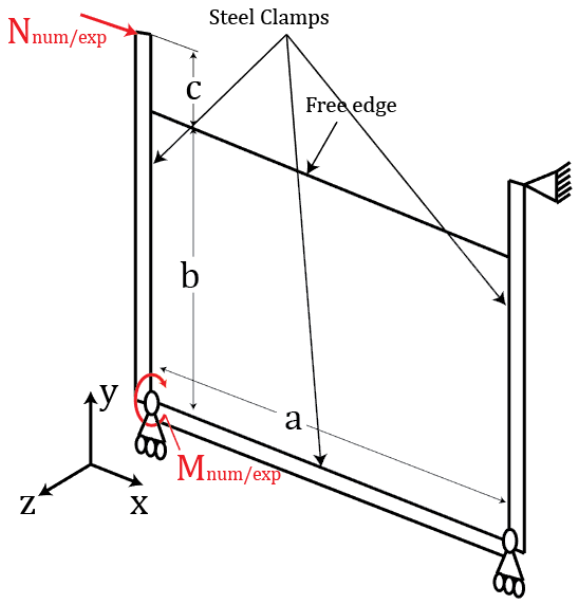

Figure 7.5 – Loading conditions of FE & experimental tests.

$$M_{num} = N_{num} \cdot (b + c) \quad (7.3a)$$

$$M_{exp} = N_{exp} \cdot (b + c) \quad (7.4a)$$

Once again, equating the numerical and experimental buckling moments to the idealized case of figure 7.1 yields the load correction factor:

$$M^* = M_{num} \rightarrow N^* = N_{num} \frac{(b+c)}{b} \quad (7.3b)$$

$$M^* = M_{exp} \rightarrow N^* = N_{exp} \frac{(b+c)}{b} \quad (7.4b)$$

7.2 Analytical vs Numerical

7.2.1 Preliminary Comparison: Simply Supported Cases

As a starting point for the comparison of the results, the solution of the simply supported MSC Marc models, where the steel clamps are not present (figure 6.15), are plotted against the results of the simply supported plates (without applying the effective length factors) from the semi-analytical model. Section 6.3.1 showed the simply supported boundary conditions imposed on the FE models which are equal to the initial semi-analytical solution. It is important to bring back the question whether the solution of the semi-analytical model must consider the presence of the adhesive when calculating the buckling loads or not, as it was discussed at the end of Chapter 4. Figure 7.6 shows that the buckling loads from the FE models fall within the range of results of the unbonded semi-analytical results, between $N^* = 0.4x10^4 - 2x10^4\ N$. Therefore, it can be determined that the adhesive does not have a major effect in the determination of buckling loads.

Figure 7.6 also shows the accuracy of the determined buckling loads: results for low aspect ratios $AR \leq 2$ fall within 18% of each other. The semi-analytical model becomes slightly more accurate as aspect ratio increases, reducing the discrepancy to under 10% as given by table 7.2. Note that to obtain the FE solutions, the load was applied precisely at the corner of the plate (since the clamps were deleted from

the model), reflecting the idealized case from figure 7.1 and thus not needing a correction factor dependent on c.

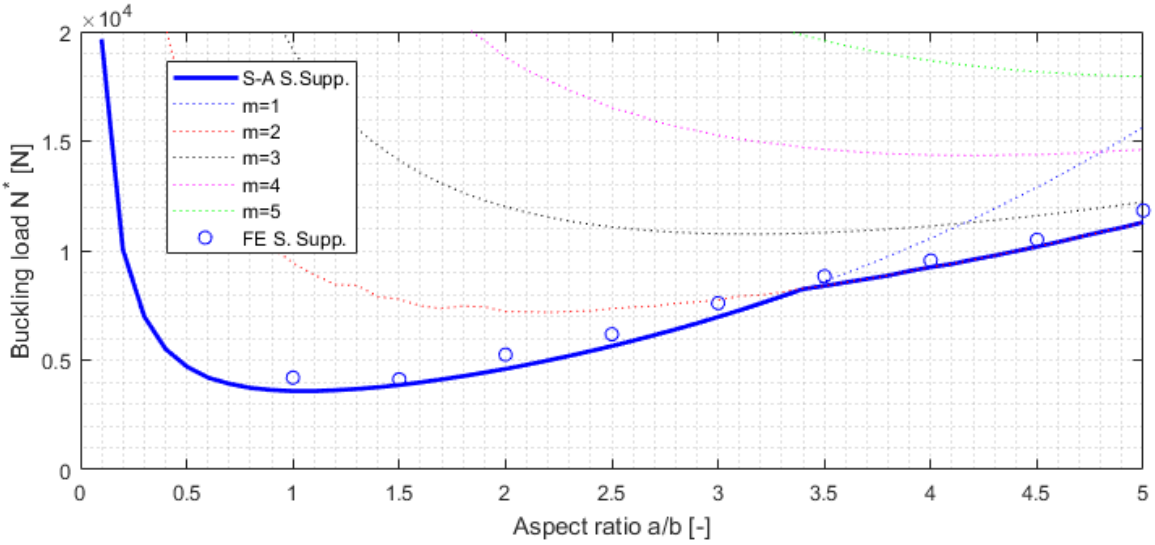

Figure 7.6 – Semi-analytical vs numerical buckling loads and modes for the simply supported case.

Aspect Ratio	1	1.5	2	2.5	3	3.5	4	4.5	5
N* FE [N]	**4,200**	**4,130**	**5,250**	**6,180**	**7,600**	**8,830**	**9,510**	**10,500**	**11,830**
N* S-A S.S. [N]	3,585	3,860	4,598	5,640	6,970	8,383	9,244	10,180	11,290
Error S-A [%]	17.15%	6.99%	14.18%	9.57%	9.03%	5.33%	2.87%	3.14%	4.78%

Table 7.2 – Buckling loads of simply supported case for plates solved semi-analytically and numerically.

7.2.2 Semi-analytical Results after Effective Length Factor vs. Clamped FE Models

Once the correction factor is applied to the results of the semi-analytical model, the critical buckling load paths are plotted for varying aspect ratios and buckling modes. From the eigenvalue analysis in chapter 4.5, the minimum value is plotted in a dashed blue line for the simply supported boundary conditions after inclusion of the effective lengths $K_a = 0.65$ and $K_b = 1.2$ (section 3.2.1) for the plate dimensions a and b respectively. The plot given in figure 7.7 gives insight into the expected critical buckling load and buckling mode that the plate will undergo depending on its dimensioning. Table 7.3 gives the comparison and error percentage between the numerical and semi-analytical model.

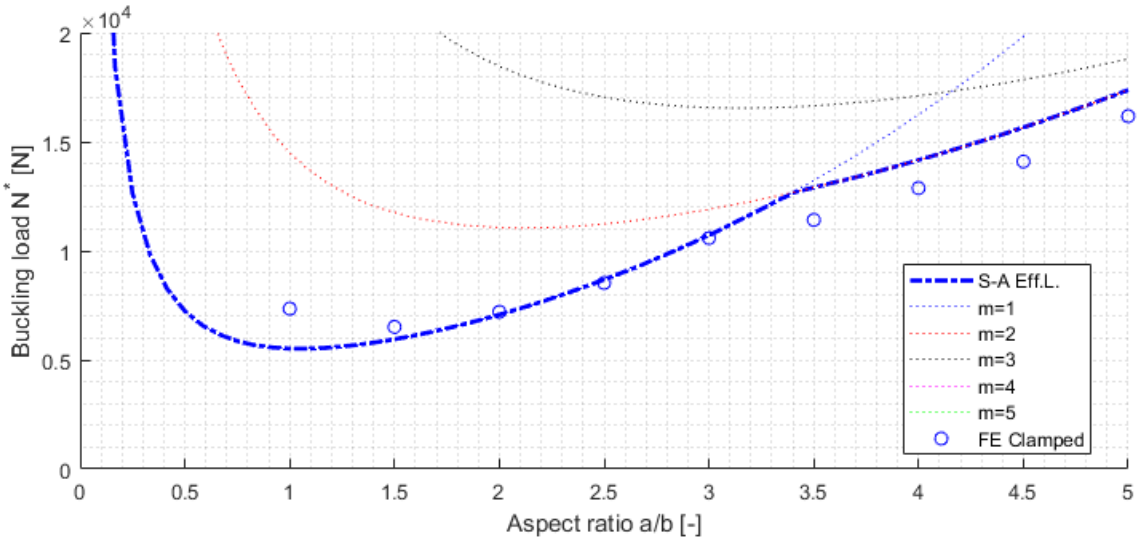

Figure 7.7 - Semi-Analytical vs Numerical Load-Aspect ratio plot.

Aspect Ratio	1	1.5	2	2.5	3	3.5	4	4.5	5
N* FE [N]	**7,350**	**6,500**	**7,210**	**8,540**	**10,620**	**11,420**	**12,900**	**14,100**	**16,150**
N* S-A Eff. L. [N]	5,519	5,948	7,079	8,678	10,720	12,900	14,160	15,660	17,370
Error Eff. L. [%]	**33.17%**	**9.28%**	**1.85%**	**−1.59%**	**−0.93%**	**−11.4%**	**−8.89%**	**−9.96%**	**−7.02%**

Table 7.3 – Buckling loads of effective length semi-analytical results and clamped FE models.

Table 7.3 shows the differences in buckling loads between the semi-analytical and numerical solutions. Compared to the simply supported case, the effective length semi-analytical solution yields larger variance between the results, underestimating the buckling loads for aspect ratios below 2 and overestimating them up to a difference of 11.4% between aspect ratios 2 to 5. The semi-analytical solution may be overestimating the results overall, especially when considering that the effect of the adhesive line is not considered. A suggestion to determine more precisely the accuracy of the semi-analytical solution is to obtain the buckling loads for the numerical models without the adhesive and carrying out the same comparison.

The semi-analytical solution also provides insight into the buckling mode shape of the plates: Figures 7.6 and 7.7 show that for plates with aspect ratio ranging from infinitely wide ($AR \approx 0$) up until $AR = 3.4$ it will show one half-sine buckling wave $m = 1$ once the load reaches the buckling load. An aspect ratio $AR \geq 3.4$ will buckle on mode 2, after which any aspect ratio around 6 is expected to buckle with three half-sine waves. This behavior remains the same from the simply supported case to the effective length solution for the same aspect ratios. Appendix H shows the buckling modes obtained from

the FE models, where, for all aspect ratios except 3 only the first solution was obtained. Aspect ratio 3 yielded the first and second modes quite close to each other and thus both are shown.

To corroborate the mode in which the FE models buckled, a line of nodes on the free edge of the plates is plotted against the out-of-plane displacement at specific load increments: $1.1x, 1.25x$ and $1.5x$ of the buckling load N^* is given in order to allow the buckling wave to develop (plotting at N^* exactly yields infinitesimally small displacements).

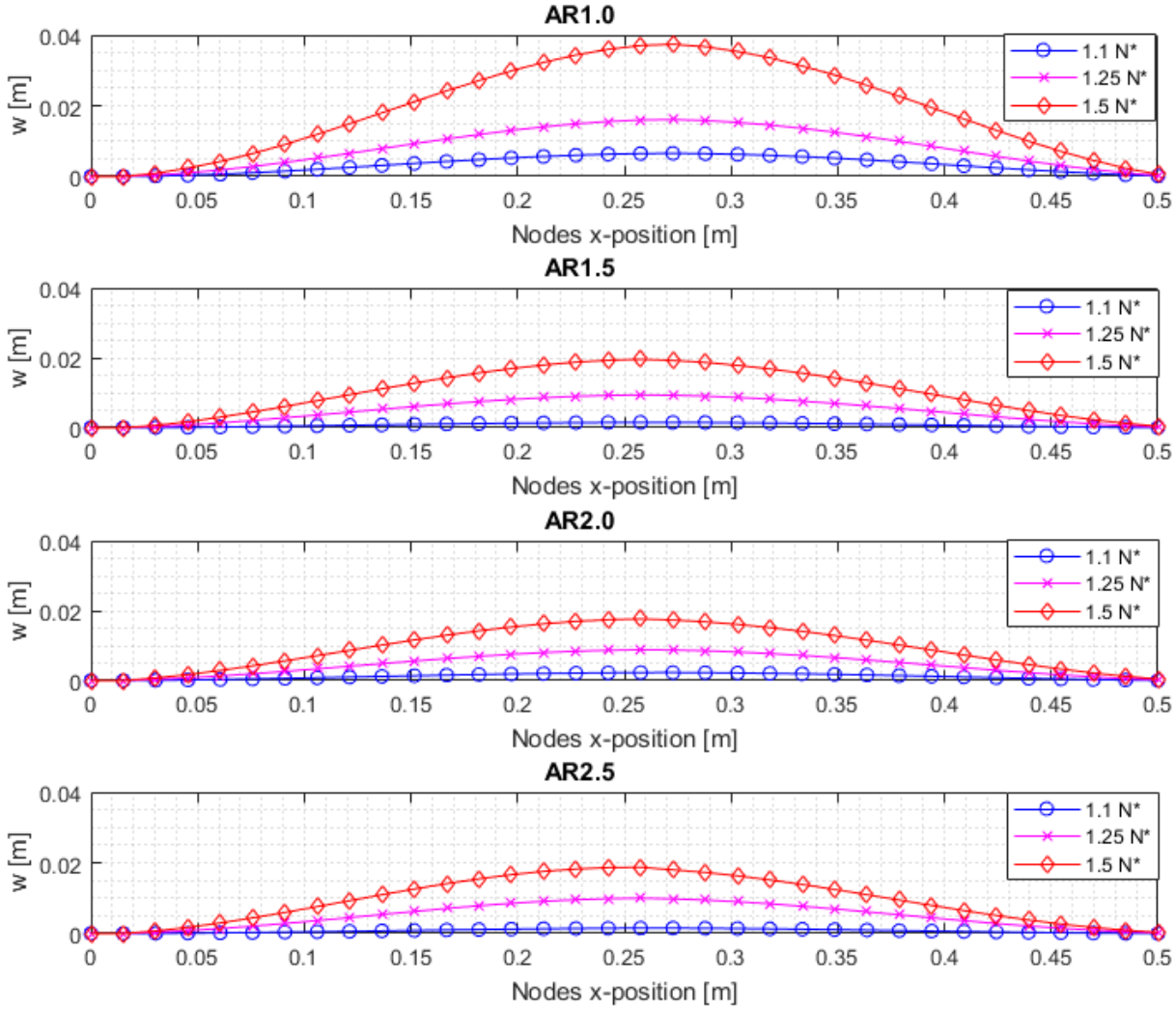

Figure 7.8 - Out-of-plane displacement of the free-edge nodes from AR=1, AR=1.5, AR=2 and AR=2.5 unskewed FE models.

It is observable in figure 7.8 that the buckling mode for all aspect ratios up to $AR = 2.5$ is one half-sine wave for all the prescribed load increments. Obtaining the out-of-plane displacements for the remaining aspect ratios yields the plots in figure 7.9. Aspect ratios 3.5 and 4 show the second buckling mode. Aspect ratios 4.5 and 5 already display the third buckling mode for all load increments. Finally, a

special case can be observed at aspect ratio 3 where the buckling wave for the load increment $1.1N^*$ is not very well developed. It appears to be buckling on mode 1 with the wave being pushed towards the left. However at the load increment of $1.25N^*$, the second half-sine wave seems to have developed on the right side.

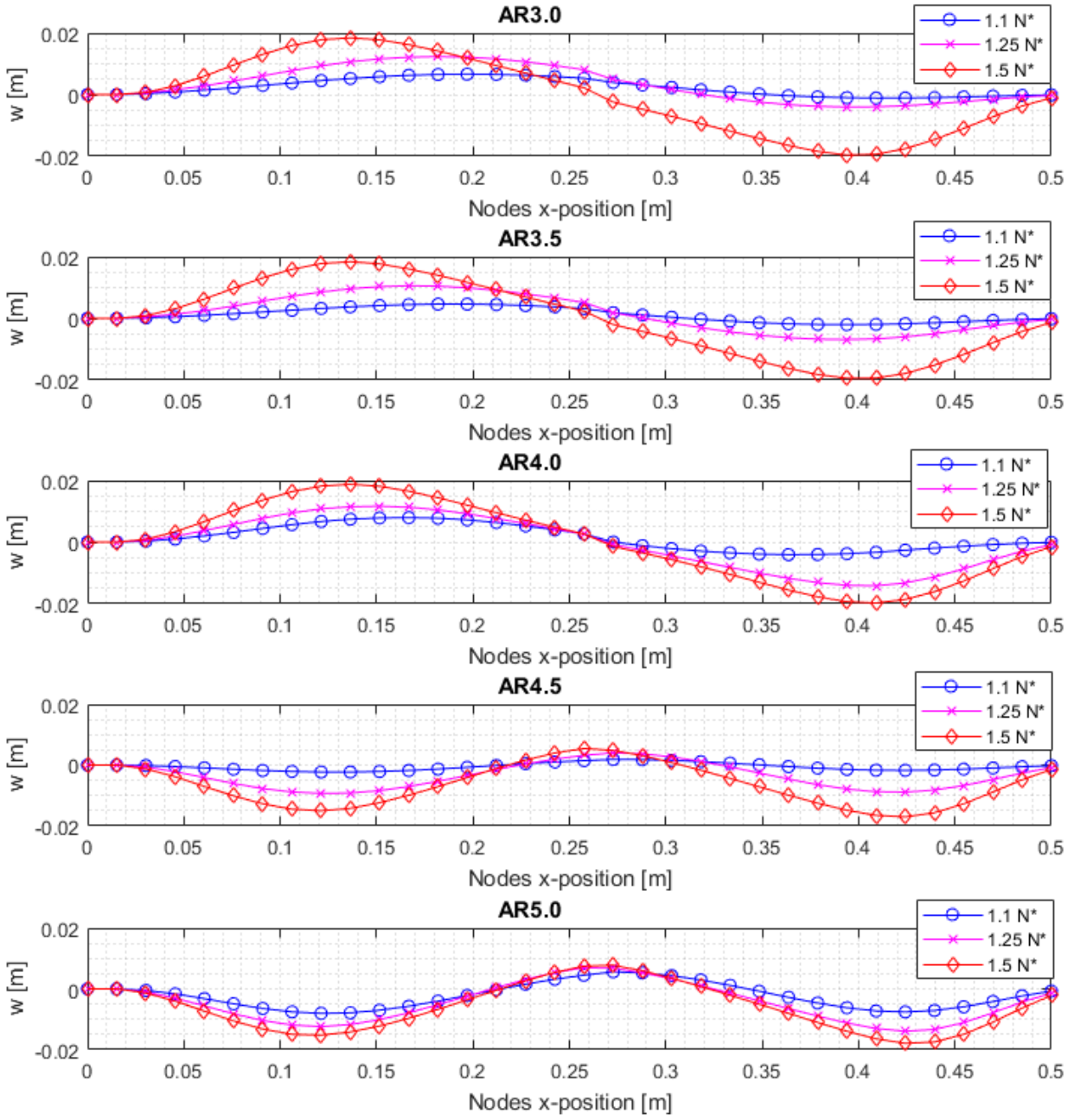

Figure 7.9 - Out-of-plane displacement of the free-edge nodes from AR=3.5, AR=4, AR=4.5 and AR=5 unskewed FE models.

An isolated plot for the buckling shapes of aspect ratio 3 is given in figure 7.10, where the reference line of zero out-of-plane displacement $w = 0$ is given. Evidently, the load increment N^* already began to develop the second buckling mode and by $1.5N^*$ it is nearly symmetrical.

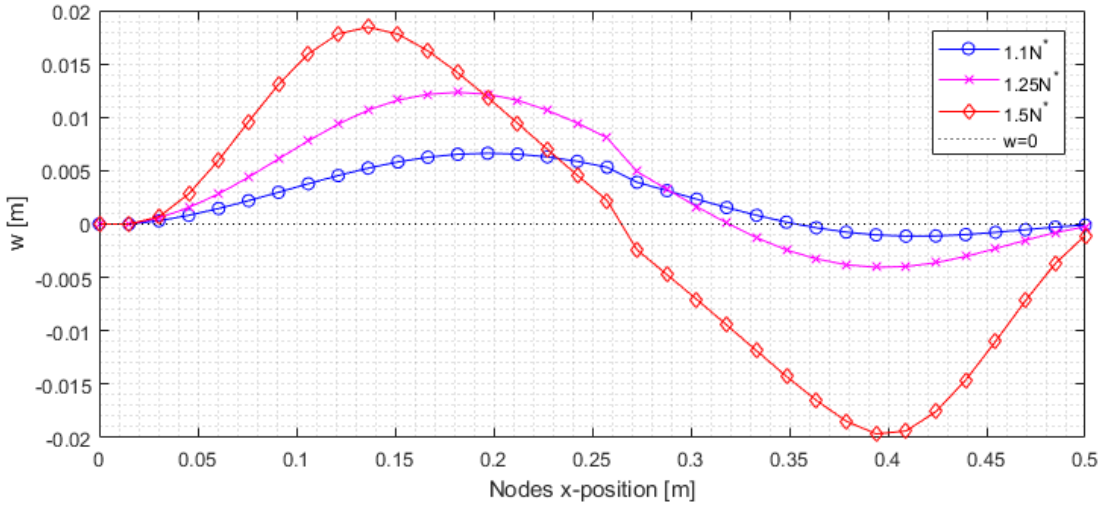

Figure 7.10 - Out-of-plane displacement of the free-edge nodes from the AR=3 with load increments where mode transition occurs.

Plotting the load increment $1.1N^*$ at aspect ratio 3 as well as $1.25N^*$ (figure 7.11) demonstrates that even for the semi-analytical model, the transition into the second mode does occur within such range. While these may seem like satisfactory results, further study must be carried out with other material/configurations to corroborate that the predictions are still compliant with the FE results.

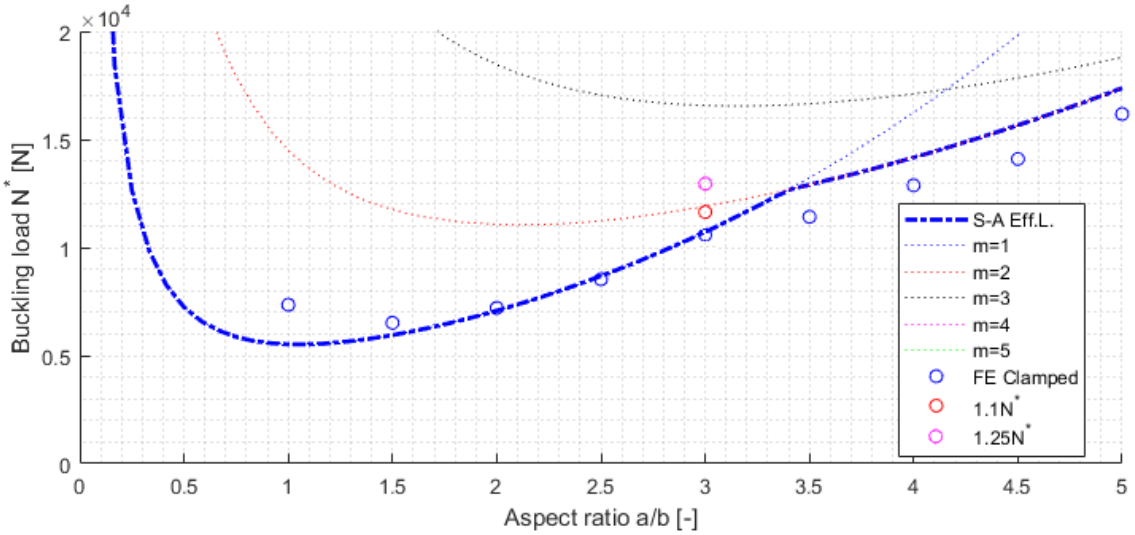

Figure 7.11 – Mode transition for plate of $AR = 3$ between mode 1 and mode 2 at $1.1N^*$ and $1.25N^*$.

Adding a color-coded overlay of the buckling modes that the FE models showed in figure 7.12 demonstrates the accuracy of transition between mode 1 and 2 as aspect ratio is in the vicinity of 3. On the other hand, the transition into the third mode is not as close, appearing for the semi-analytical results after $AR = 5$ but between 4 and 4.5 for the FE models. It follows logically then that the mode curves should have a steeper upwards slope as aspect ratio increases, whilst the buckling load predictions could be lower.

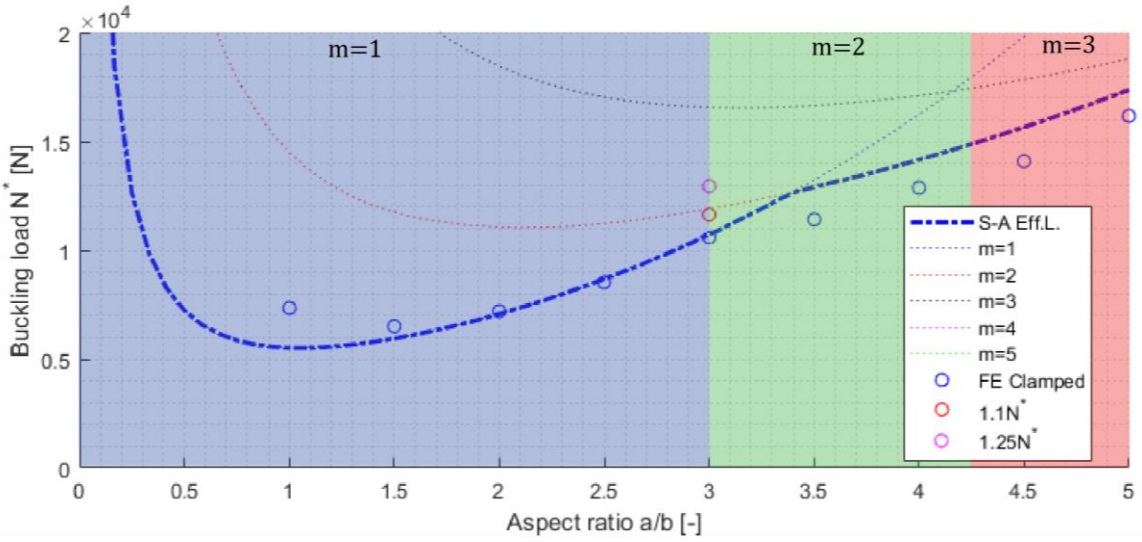

Figure 7.12 - Mode transition of FE models in comparison to S-A mode curves.

7.2.3 Twist Modelled as an Initial imperfection $\bar{w}(x, y)$

Modelling the loss of load-bearing capacity of the structure due to an initial imperfection requires evaluating the out-of-plane displacement $w(x, y)$ with the output amplitude coefficient w_0 from the semi-analytical tool at any given point of the plate. The resulting displacement can then be compared with output node data from the FE models.

For the twisted plate, it is known that the boundary of the plate at $y = b$ will not undergo any more out-of-plane deflection aside from the initial twist (figure 7.13). Therefore, a position along the free edge close to the corner is taken, and the out-of-plane displacement is plotted in figure 7.14 for both the semi-analytical (equation 4.31b/7.5) and numerical models.

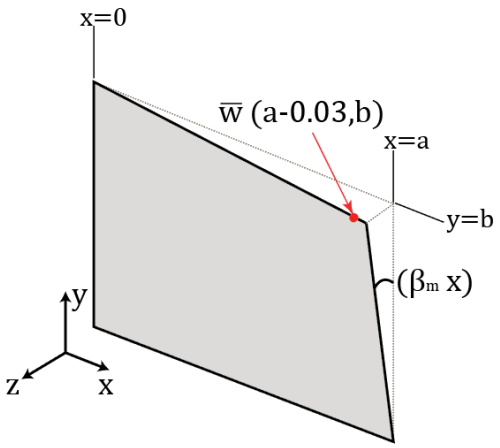

$$w(a-0.03,b) = w_0 \sin\left(\frac{2\pi(a-0.03)}{a}\right)\sin(\lambda\pi)$$

$$w(a-0.03,b) = -\sin(0.03a)\sin(\lambda\pi) \tag{7.5}$$

Figure 7.13 - Twisted plate and point of comparison for imperfection modelling between S-A and FE.

The first observable effect of twist on the plot lines is the loss of carrying capacity of both models induced by such small angle deflections. Although the out-of-plane displacements remain small, the point of instability shows a decrement from the un-twisted (blue lines) at the buckling load $N^* = 10{,}620N$ down to around $N^* \approx 8{,}000\ N$ for a twist of $\beta = 5°$. Both models behave quite similarly in this aspect. One evident downside is that semi-analytical tool overestimates the stiffness prior to the buckling loads. During post-buckling, the FE results show a more erratic behavior stemming from the numerical nature of the model, whereas the semi-analytical either overestimates the deflections (for $\beta = 0°, 1°, 2°$ and 3°) and underestimates them for $\beta = 4°$ and $5°$.

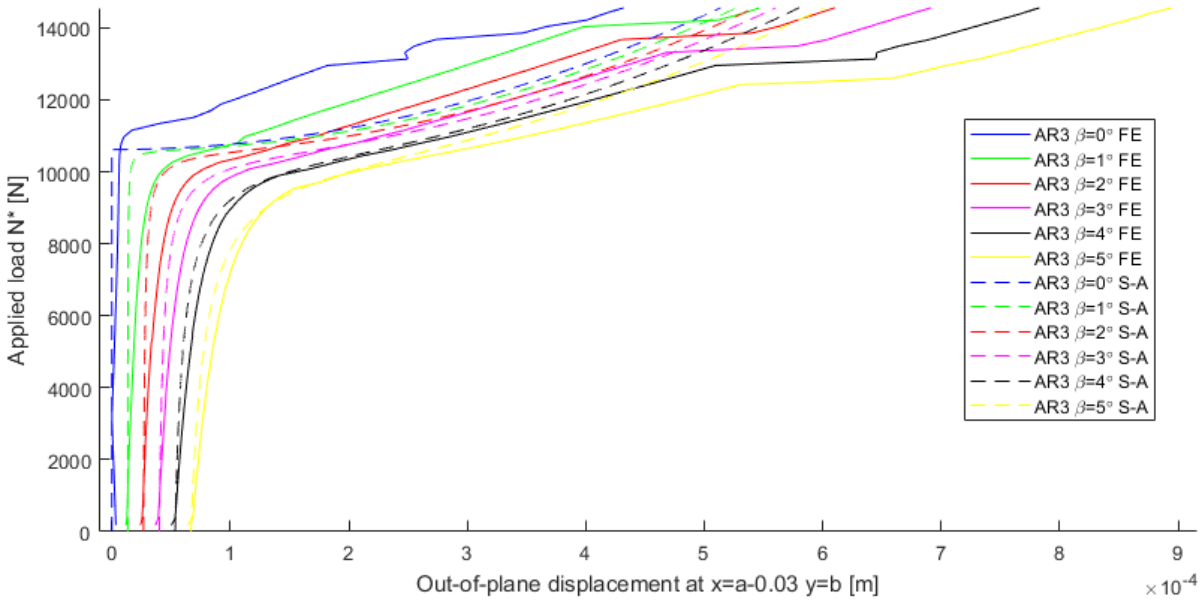

Figure 7.14 - Effect of plate twist as an initial imperfection on the plate for a plate of AR=3, unskewed for semi-analytical and FE models.

These results are highly sensitive to the choice of point for evaluation of the displacement field equation as well as the buckling mode that the plate presents. Looking at the results from the previous section where it was determined that a plate of aspect ratio 3 is very close to the transition from mode 1 to mode 2 made this, in hindsight, a poor choice for aspect ratio. It would be better to model the imperfection on a plate with an aspect ratio that does not transition into another mode, such that the mid-point of the free edge could be plotted, and larger values of out-of-plane displacements are reached. Additionally, accurately modelling the post-buckling behavior with the semi-analytical tool requires more advanced methods that are not covered in this research. Regardless of this, the compliance between the results of the buckling loads are quite satisfactory.

7.2.4 Pre-bend Modelled as an initial imperfection $\bar{w}(x, y)$

Modelling the pre-bend of the plate induced by plastic deformation from a buckling test in the semi-analytical and FE models was done using the artificial displacement field given by equation 4.41, repeated below for clarity:

$$\bar{w}(x, y) = w_{ini} \sin\left(\frac{\pi x}{a}\right) \sin\left(\frac{\lambda \pi y}{b}\right) \qquad (4.41/7.6)$$

An initial pre-bend coefficient $w_{ini} = 0.003\, m$ is chosen, consistent with the experimental deformed plate (figure 6.18). In contrast to the previous section for the twist as an imperfection, the maximum out-of-plane displacement from the FE free edge is plotted (instead of a specific point on the plate). This is done because of the dependency on the buckling mode is lost as the pre-bend (which has a mode 1 shape) promotes only that mode during buckling. This simplification makes it easier to compare with the output displacement coefficient w_0 from the S-A model. Results from both models are plotted against each other in figure 7.15. This figure demonstrates the loss of load carrying capacity of the FE models from a perfectly flat plate (blue circled line) to an initial pre-bend with maximum initial amplitude w_{ini} of merely $3\, mm$ (red crossed line). This comparison shows that such a slight pre-bend accelerates buckling for considerably low loads.

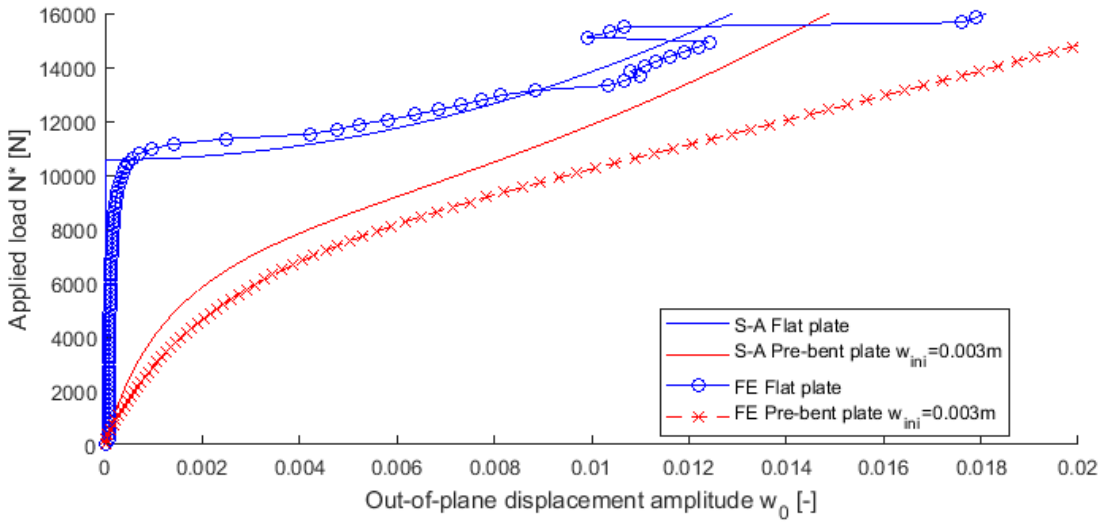

Figure 7.15 - Effect of plate pre-bend as an initial imperfection on the plate for a plate of AR=3, unskewed for semi-analytical and FE models.

The semi-analytical results are plotted for both a perfectly flat plate and the pre-bent plate. While the stability lines for the flat plates show surprisingly good compliance (where the erratic behavior between $12\ kN$ and $15\ kN$ is due to the mode transition), the semi-analytical results for the pre-bent case show a stiffer response all throughout the load increments. Therefore, the semi-analytical results should be taken with care as in experiments, where the structure will be more imperfect than the FE results, the structure will possess a lower load-bearing capacity. The effect of the pre-bend from the FE analysis is compared with the experimental results in the following section.

7.3 Numerical vs Experimental

A comparison is now made between the numerical and experimental results, specifically the load-displacement curves of a plate of aspect ratio 3. While the semi-analytical model provides an initial expectation for the behavior of the plate in regards of buckling loads and out-of-plane displacements, it assumes a perfectly sinusoidal buckling shape for the solution. This assumption leads to incomparable pre- and post-buckling force displacement curves. On the other hand, a numerical model approach, while more computationally intensive and requiring more preparation, yields more reliable information on whether the experimental set-up is properly designed and how it can be further improved.

The first experimental test was made with coupon TEB03. The blue solid line in figure 7.16 below shows the force-displacement curve for this test: observe that while the buckling load reaches around $10{,}589\ N$ (compared to the $10{,}620\ N$ of the FE analysis), much of the load-carrying capacity of the system is lost in the first load steps of post-buckling. In the initial clamp design and as discussed in chapter 5.2.1,

two out of the three elements from the clamp opposite of the free edge (GroupID 2 in appendix E) were made of nylon. These nylon pieces and the single clamp element made of steel were insufficiently stiff for the free-edge buckling test, as they also began to buckle. Figure 7.17 shows a picture taken of the buckling from the posterior clamp with nylon pieces. For the subsequent tests, the two exterior nylon pieces were replaced with steel ones.

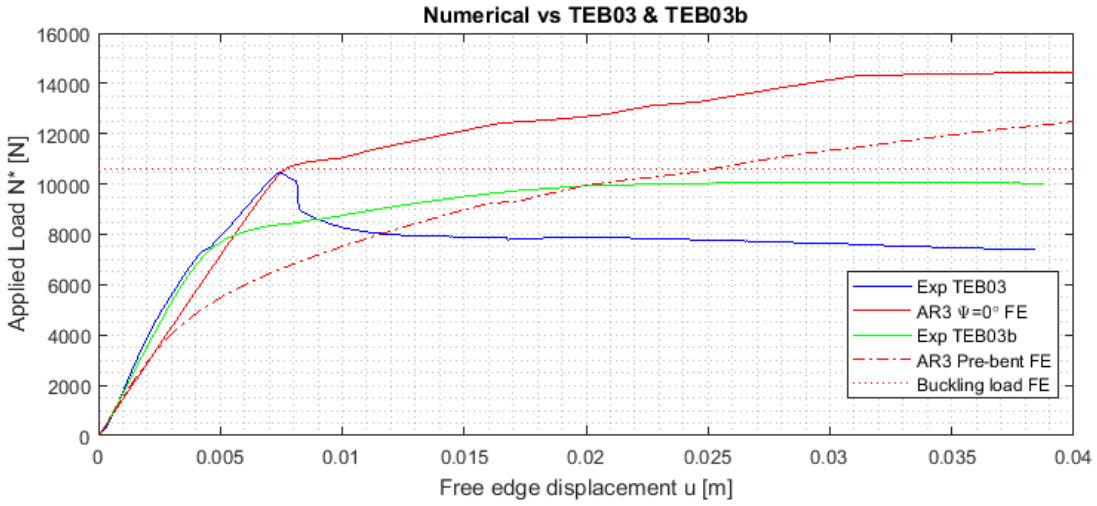

Figure 7.16 – First and second tests done on TEB03. Experimental vs. FE force-displacement.

Figure 7.17 - Posterior clamp buckling due to insufficient stiffness of nylon pieces.

Following the release of the overhead of the compression machine, coupon TEB03 had undergone plastic deformation, resulting in a slight pre-bend with a half-sine wave shape with a maximum amplitude of $3\ mm$ around the mid-point of the free edge. Figure 6.18 from the argumentation of the pre-bend shape for the FE modelling is shown below once again (7.18).

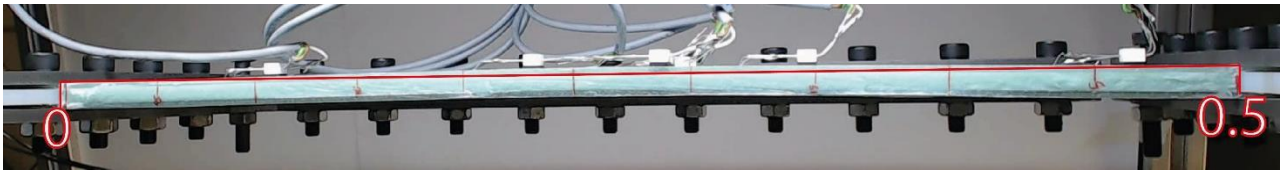

Figure 6.18/7.18 - Free-edge pre-bend due to plastic deformation of experimental specimen with a maximum amplitude of roughly 3mm.

A second test was done for TEB03, renamed to TEB03b from now on (green solid line). This second test for the specimen was done with the full steel posterior clamp. Results from this second test showed a reduced buckling load of about 20%, buckling at about $8{,}000\ N$, while the post buckling load-carrying capacity was increased. Looking at the experimental test, the buckling of the posterior clamp appears to be solved by the inclusion of the full-steel pieces (figure 7.19).

Figure 7.19 - Testing of TEB03b with a redesigned full-steel posterior clamp.

Comparing the experimental results (green line) from the pre-bent specimen to those of the pre-bent FE model (dashed red line) in figure 7.15 show that the pre-buckling stiffness of TEB03b is higher than what the MSC Marc model anticipated. On the other hand, the post-buckling behavior did not reach as high loads as the FE model. The remaining two experimental tests provide more insight as to why this happened.

TEB01 showed an improved result due to the improved clamp, shown in figure 7.20: Upon reaching the buckling point at $10{,}531\ N$ (just 0.82% off from the FE model), the panels still possessed a post-buckling load-carrying capacity that reached a maximum of $11{,}250\ N$. At that point, a new weak point was found at the hinged corners, where an out-of-plane twist commenced for the posterior clamp.

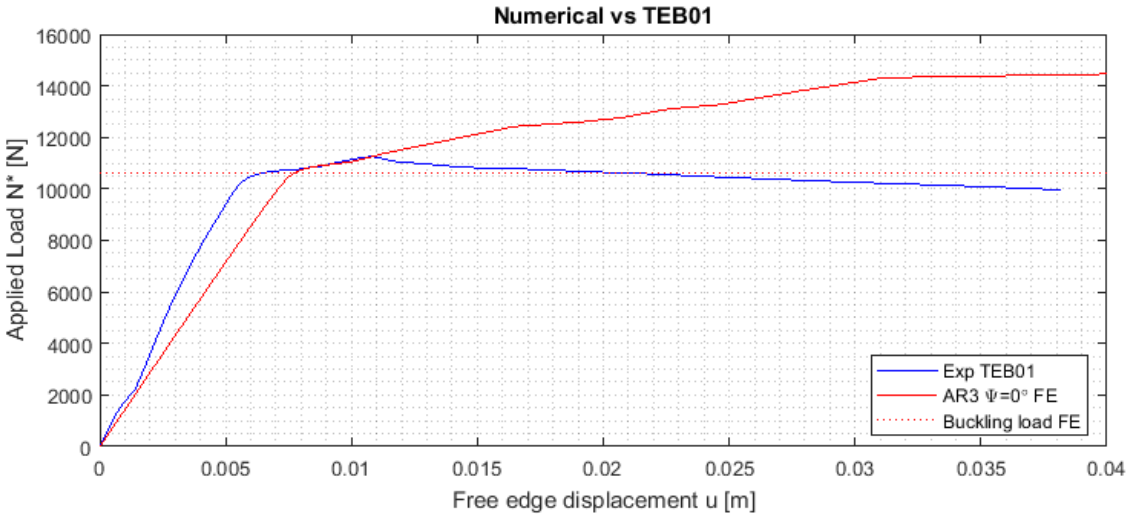

Figure 7.20 – TEB01 Experimental vs FE force-displacement.

Notice in figure 7.21 that the underside of the posterior clamp is slightly visible (highlighted in red) despite the fact that the camera was positioned perpendicular to the flatness of the plate, and the right sliding clamp is slightly twisted upwards. As such, the posterior clamp did not fulfill its endeavor of fully clamping the plate by allowing an out-of-plane rotation along the y-direction of the plate $w_y(x, 0)$.

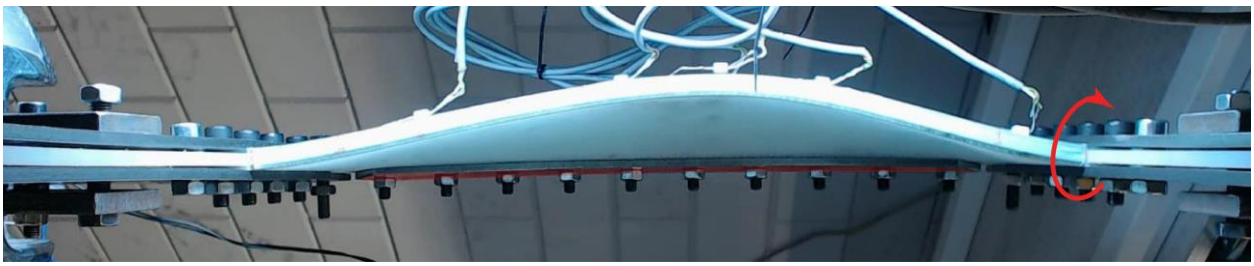

Figure 7.21 - TEB01 Test upon which twisting of the hinged corners was found.

The last specimen to be tested (TEB02) in figure 7.22 demonstrated a buckling load slightly higher than the previous two at around $11{,}062\ N$. Its maximum post-buckling load prior to twisting of the posterior clamp reached $11{,}070\ N$. Preventing the buckling of the plate to induce a twist on the corner sections of the clamp would require a full redesign of the clamps. Instead, a suggestion is to model the non-linear elastic FE models by including a release of the rotational constraints of the steel clamps at the time where the buckling load is reached.

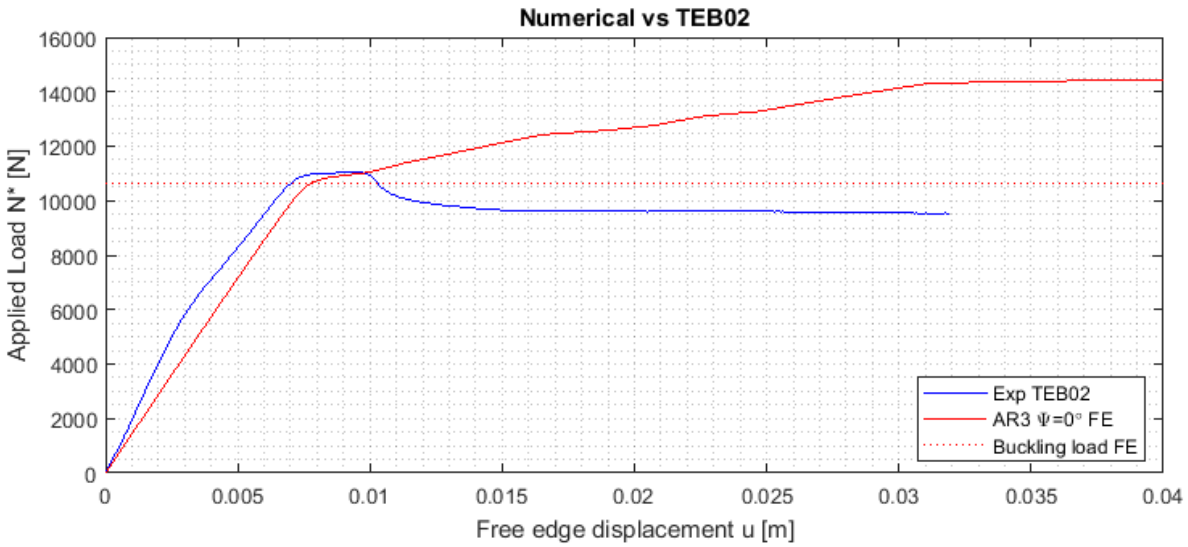

Figure 7.22 – TEB02 Experimental vs FE force-displacement.

Table 7.4 provides a comparison and error percentages from the results of the experimental tests and numerical models for the critical buckling load N^*.

	FE Model	TEB01	TEB02	TEB03
N^* $[N]$	$10{,}620\ N$	$10{,}531\ N$	$11{,}062\ N$	$10{,}589\ N$
$Error$ [%]	N/A	0.82%	4.09%	0.29%

Table 7.4 – Comparison of critical buckling load N^* and error percentages between numerical FE model and experimental tests.

One final aspect to point out in regards of the load-displacement experimental results is the apparent increased stiffness during pre-buckling. This behavior can be observed in figures 7.16, 7.20 and 7.22 on the steeper slope of the experimental specimens with relation to the predicted curve of the FE models. This indicates that the movement of the clamping system may have been restricted in some degree. There is an expected cause for this at the connection of the clamping system with the compression machine, which will be discussed in the following chapter.

7.4 Skew Angle

As the skew angle induced by a reduction of chord length in a wind turbine blade was another point of interest of the research, the results obtained from the FE models are presented. Unfortunately, the semi-analytical model had the shortcoming that some coupling and non-linear terms vanished due to the choice of orthogonal displacement fields. This made it impossible to include the skew angle into the model. Points for improvements regarding this issue will be discussed in Chapter 8. Nevertheless, having shown the reliability of the finite element models in comparison with the experimental results in obtaining an accurate buckling load with a margin of error below 5%, the buckling loads for all FE models with skew angles of $\Psi = 5°$ and $\Psi = 10°$ are plotted in the $N^* - AR$ graph given in figure 7.23.

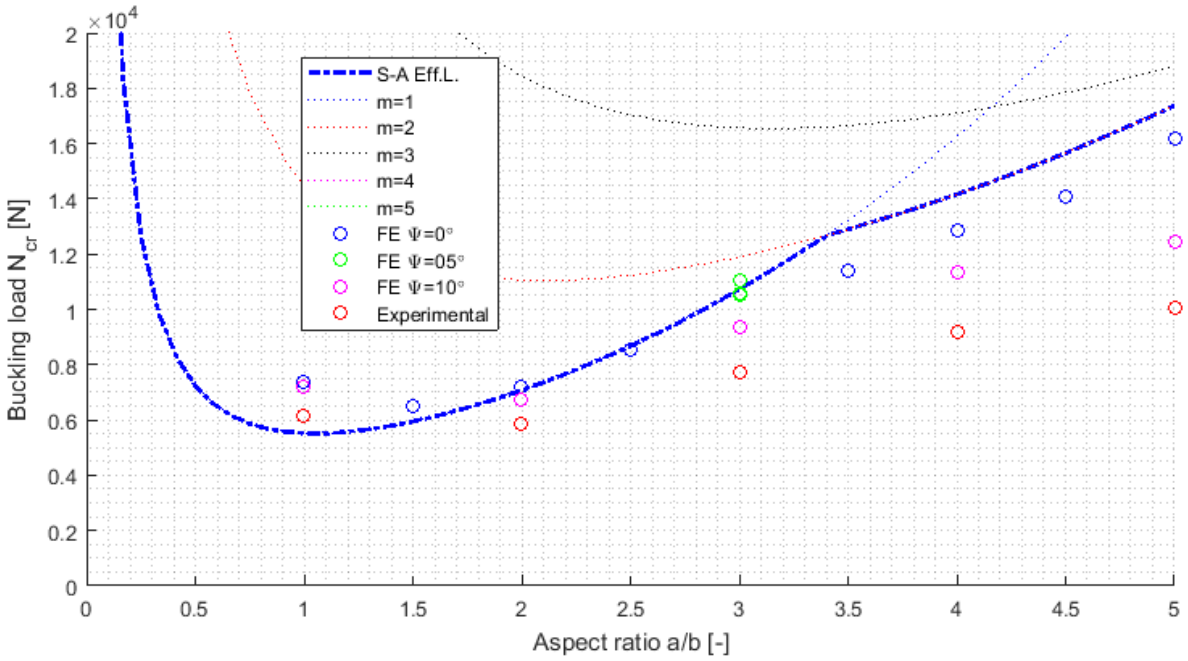

Figure 7.23 - Effect of skew angle on reduction of critical buckling load N.*

It is readily observable that the skew has a major effect in the reduction of load-carrying capacity of a plate. The buckling loads for the different aspect ratios of plates with $\Psi = 5°$ is shown in magenta colored circles, whereas $\Psi = 10°$ is given in red circles. The reduction of buckling load N^* for these models in relation to the unskewed plates is given in table 7.5:

Aspect Ratio	1	2	3	4	5
$N^*\ \Psi = 0°$	7,350	7,210	10,620	12,900	16,150
$N^*\ \Psi = 5°$	7,200	6,750	9,358	11,340	12,450
$\boldsymbol{N^*}$ **reduction** [%]	$\mathbf{-2.04\%}$	$\mathbf{-6.38\%}$	$\mathbf{-11.88\%}$	$\mathbf{-12.09\%}$	$\mathbf{-22.91\%}$
$N^*\ \Psi = 10°$	6,150	5,850	7,739	9,180	10,050
$\boldsymbol{N^*}$ **reduction** [%]	$\mathbf{-16.32\%}$	$\mathbf{-18.86\%}$	$\mathbf{-27.12\%}$	$\mathbf{-28.83\%}$	$\mathbf{-37.77\%}$

Table 7.5 – Losses in critical buckling load N^* due to skew angle for varying aspect ratios obtained from FE models.

Table 7.5 shows that there is a direct relation between the negative effect of a specific skew angle and the slenderness of the plate: higher aspect ratios (and therefore lower plate width b) become increasingly susceptible to buckling at lower loads.

7.5 Strain gauge measurements

Buckling loads and displacements are not the only point of interest of the research. Strains provide insight into the degree of accuracy of the models. Strain measurements are given for the two lines of strain gauges: Firstly, strain gauges 1-4 which were placed on a line parallel to the free edge just $2.5\ cm$ to the side, measuring the strains along the x-axis of the frame of reference of the plate. Secondly, strain

gauges 5-8 which were located along the midline of the plate's length $x = a/2$ and also aligned with the x-axis of the plate's coordinate system.

Prior to experimental testing it was impossible to determine the direction of the buckling wave: The plate could buckle towards either of the facesheets. Fortunately, and for the ease of comparison of the results, every plate buckled towards the plate with the strain gauges adhered to it. Below in figure 7.24, the free edge of the plate is shown with the position of each gauge. Figure 7.25 shows the microstrains following the buckling wave along the free-edge of the plate.

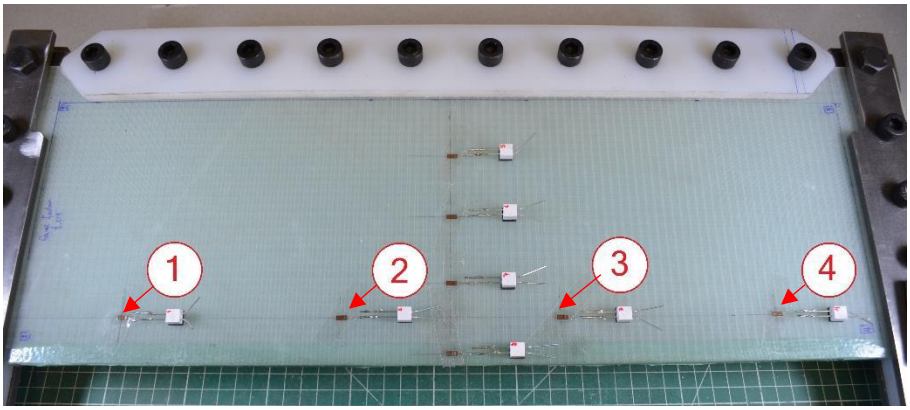

Figure 7.24 - Positions of strain gauges 1,2,3 and 4 parallel to the free edge of the plate measuring microstrains in the x-direction (length) of the plate.

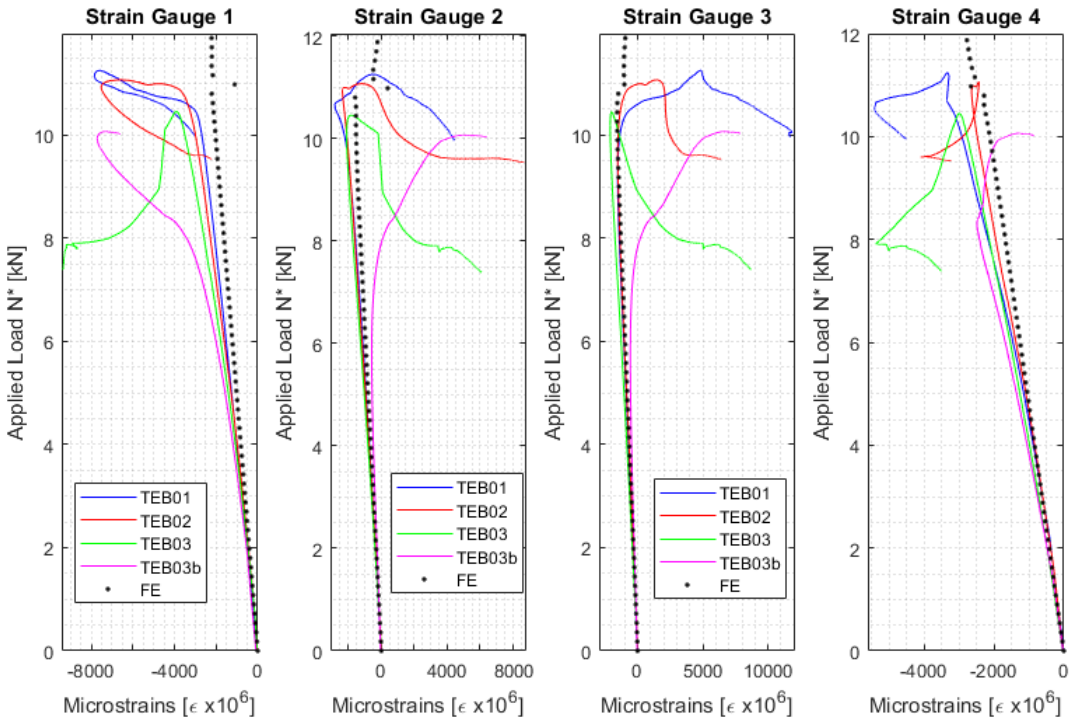

Figure 7.25 – Strain gauges 1, 2, 3 and 4 microstrain data ε_{xx} plotted vs Applied Load N^*.

The x-direction component of the strain ε_{xx} was measured and plotted in figure 7.25. A change from negative to positive microstrains demonstrates the change from compression to tension on the plates surface. Looking at the data from strain gauges 1 and 4 these remain purely in compression and therefore on the outer edges of the buckling wave. Every test showed very similar stiffness as appreciated on the slope of the curves prior to reaching the buckling load N^*. Two major differences are appreciated on tests TEB03 and TEB03b, stemming from reasons which have been discussed in section 7.2 due to an insufficiently stiff clamp and a pre-bent plate respectively. Figure 7.24 includes strain data from extracted from the FE model from nodes located at the same location that the experimental strain gauges were placed. The FE strains are surprisingly close to the experimental data up to the buckling load. Data from the FE model was cut off at higher loads since it was already shown that post-buckling behavior is not consistent between both models. Moreover, the experimental results do not reach higher loads for comparison, as the overhead displacement from the compression machine did not need to exert more force to keep progressing.

The position of strain gauges 5,6,7 and 8 is shown once more in figure 7.26 below in a clearer view than that from figure 5.12.

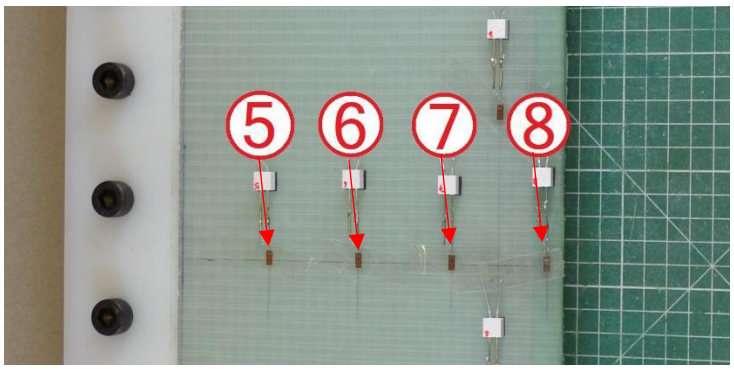

Figure 7.26 - Positions of strain gauges 5,6,7 and 8 along the width b of the plate situated at the mid-length of the plate a/2 measuring microstrains in the x-direction.

Additionally, for comparison between the FE and experimental tests, the longitudinal strains ε_{xx} along the line of nodes on the mid-length of the plate $a/2$ was extracted. These nodes were evenly spaced with a distance of $0.5\ cm$ between each other, observable in figure 7.27 below.

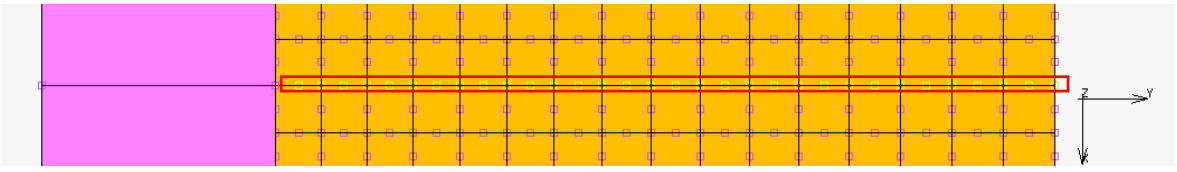

Figure 7.27 - Node position on FE model from which strain components along the x-direction ε_{xx} were extracted.

Figure 7.28, 7.29 and 7.30 show a comparison between the in-plane strains along the x-direction ε_{xx} for the FE models in dotted lines and the experimental tests in solid lines. Three different load increments are given during pre-buckling, at $0.5N^*$, $0.75N^*$ and at the buckling load N^* in blue, magenta and red colors respectively.

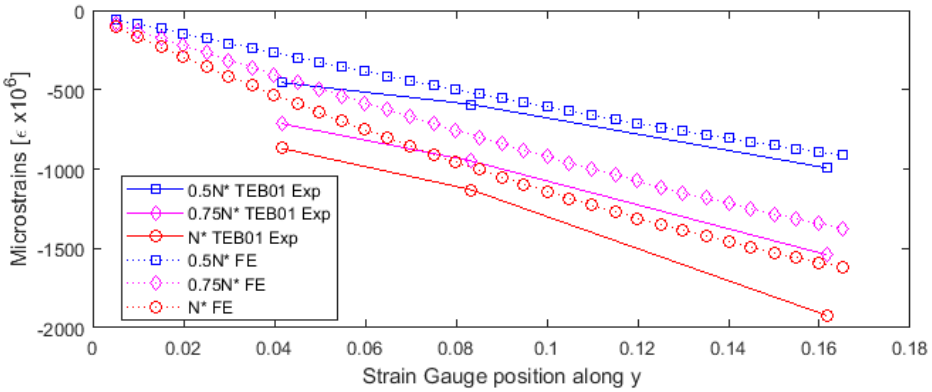

Figure 7.28 – TEB01 in-plane compression strains ε_{xx} compared to the FE model results along the plate's width.

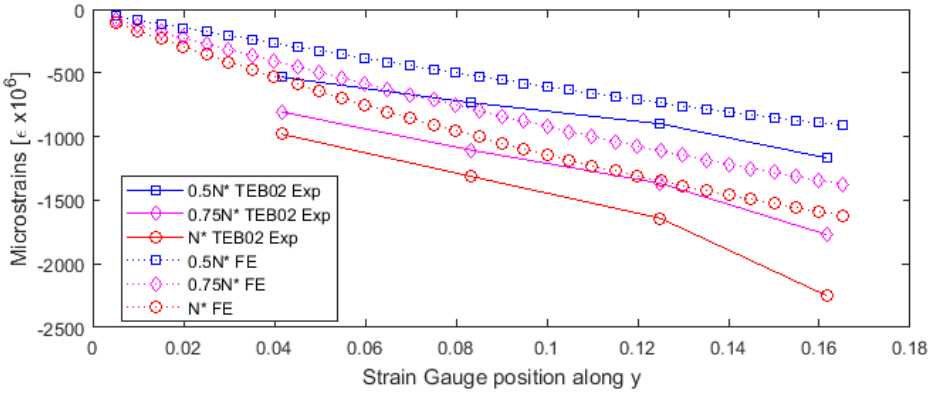

Figure 7.29 – TEB02 in-plane compression strains ε_{xx} compared to the FE model results along the plate's width.

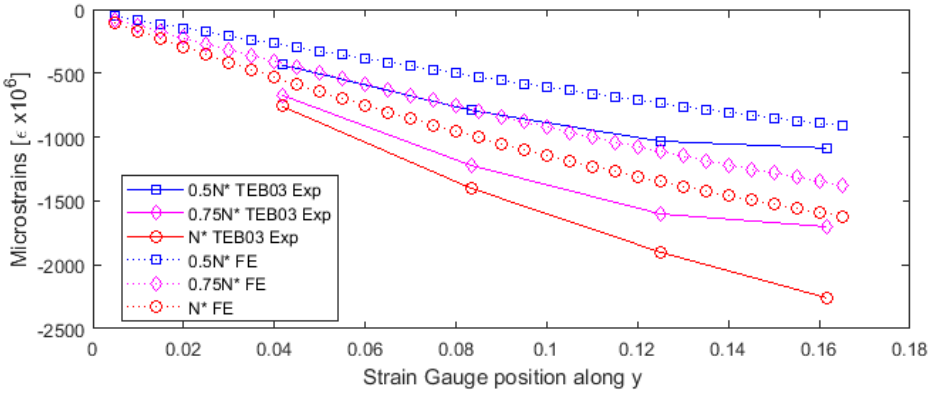

Figure 7.30 – TEB03 in-plane compression strains ε_{xx} compared to the FE model results along the plate's width.

The differences between the experimental and numerical methods in figures 7.28,7.29 and 7.30 show that strains are developing at an accelerated rate in the experiments. These differences are comparable to the strain differences from FE and the experimental tests from figure 7.25 at the specified load increments. From this, one may expect that the experiments may fail earlier than the prediction from FE models once debonding is reached, due to the dependency of this failure mode on the strains. Nevertheless, this is rather inconclusive as the experimental set-up was unable to reach debonding.

Figure 7.31 demonstrate the evolution of the strains from the experimental tests as the machine's overhead displacement increased. Similarly to figure 7.25, a transition from negative to positive microstrains depict the transition from the facesheet being purely in compression to tension due to the bending of the plate induced by the buckling wave. Noting that for the first (under-stiffened) clamp design during testing of TEB03, the buckling of the posterior clamp can be visualized on the transition from negative to positive strains of the green line on strain gauge 5.

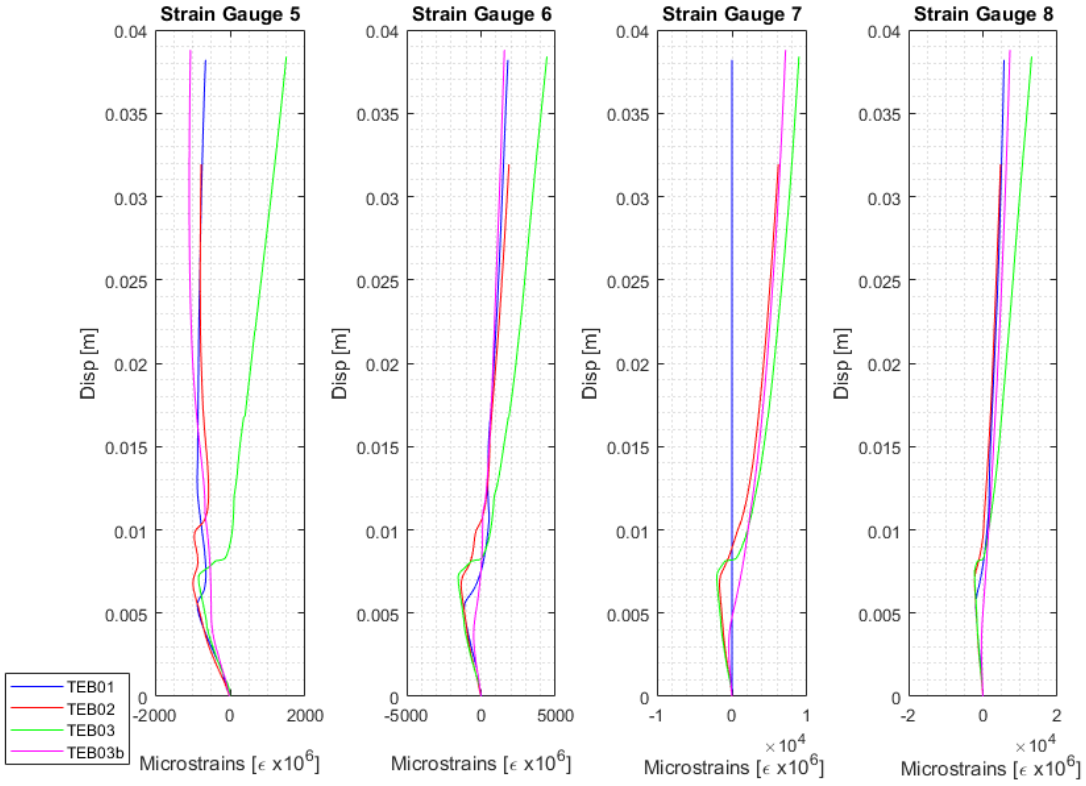

Figure 7.31 – Strain-displacement plots for strain gauges 5,6,7 and 8 for all 4 experimental tests.

The fact that the strain remains negative for TEB01, TEB02 and TEB03b for strain gauge 5, tests on which the posterior clamp pieces made of nylon were replaced by steel shows that the desired constraint preventing an out-of-plane deflection was successful, as the plate remained purely in

compression close to the clamp. Strain gauge 6 already shows a change from negative to positive strains demonstrating the development of the buckling wave at the mid-width $b/2$, increasing in amplitude as it progresses towards strain gauge 8 at the free-edge. However as mentioned before, rotation of the posterior clamp showed that proper implementation of the desired boundary conditions was not fully possible. A point that requires attention regarding the clamp design are the hinged corners: since this section connects only one of the three pieces from the posterior clamp (figure 7.32), twisting of the posterior section happened during post-buckling, leading to major loss of stiffness. An idea of adding a couple of extra coupling steel pieces between the hinge and the posterior pieces may prevent this twisting, allowing for the loading to keep increasing during compression and ideally leading to delamination/debonding at the free edge.

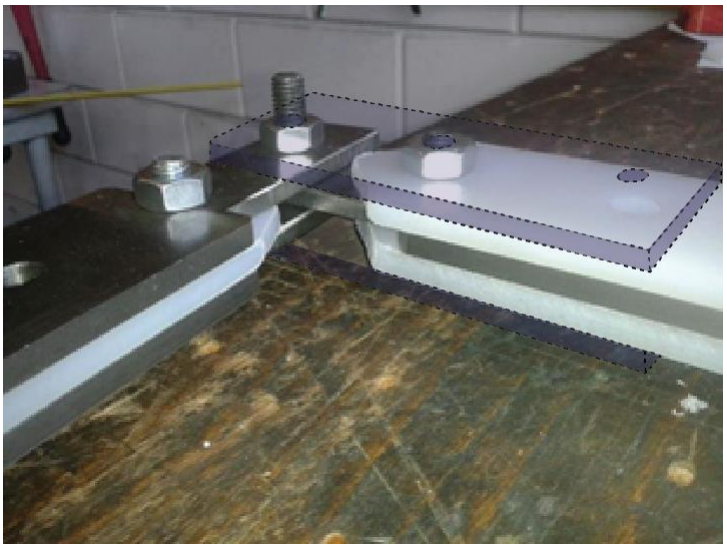

Figure 7.32 - Hinged corner of the clamping system (before replacement of nylon pieces) which showed twisting during post-buckling, along with possible pieces for reinforcement.

Chapter 8 – Discussion: Strengths & Shortcomings.

The general approach used within this research was to design a test set-up at the element and detail level of a trailing edge specimen that could be employed in future occasions. Experiments at this level can be employed to test for new material combinations, concepts or modifications and the custom clamp is indeed effective in this regard: There is flexibility in testing panels of varying dimensions, materials and skew angles. The project was made such that two analysis methods would lead to comparable results to the experiments in order to have a sturdy foundation of the research.

The semi-analytical model was capable of predicting the buckling loads for various aspect ratios within an acceptable margin of error (discussed in the following subsection), as well as roughly predicting the effect that deformations would have on the plate. Although it would be interesting to compare the results from the semi-analytical method to literature from other authors, the boundary conditions (sliding in-plane and free edge) and the coupling between in-plane and out-of-plane displacements through Von Karman's relations are quite specific to this project. After much research done on existing plate models that encompassed these aspects none could be found, to the author's best knowledge. This is another reason why this research aimed at aligning the results from the semi-analytical model with the other two, more reliable methods.

In the areas where the semi-analytical model did not perform well, FE analysis was employed to fill the gaps. Along with delivering the buckling loads with better precision for the chosen aspect ratio when compared to the experimental tests, the pre-buckling and post-buckling behavior could be determined with a non-linear elastic analysis. Preliminary results for the skew angle could be obtained, and even though these could not be validated with experimental tests, the resulting trend in reduction of load-bearing were expected.

Finally, the custom clamp system seemed to perform as desired during pre-buckling and up to loads immediately after buckling. Later post-buckling stages could not be compared due to complete loss of stiffness of the structure and several improvements are suggested.

All things considered, the three methods seemed to form a cohesive basis for the element and detail test of the trailing edge. There is still, however, ample room for improvements at every step of the process which will be discussed in this chapter.

8.1 Semi-analytical model

8.1.1 Buckling Loads and Modes

The performance of the semi-analytical model showed an acceptable accuracy in comparison to the FE results when calculating the buckling loads. For the simply supported case it predicted the buckling loads in a range of error between $3\% - 17\%$. Once the effective length correction factors were applied and the results compared to the clamped FE buckling loads, the range of error of the results was between $1\% - 33\%$. Variance in error was larger and results were less conservative at higher aspect ratios. This illustrates the inaccuracies that the assumptions made for the semi-analytical model cause on the results: Buckling modes do not always adopt symmetric sinusoidal shapes that the solution of the displacement fields assume. Additionally, the solution of the model through the effective length correction factors was employed as a "shortcut" to idealize clamped boundary conditions. This assumption may induce larger deviations from the actual buckling loads than if the semi-analytical model employed actual clamped boundary conditions. Implementation of such clamped boundary conditions in the derivation of the stability and equilibrium equations may lead to more reliable results.

Additionally, the assumption that the presence of the adhesive does not have a major effect on the buckling loads may be another source of loss of accuracy in the results, even though the presence of the adhesive is only in $1/15^{th}$ of the plate's width b as it was established in Chapter 3. A parametric study of the effect of the adhesive line at the free edge may be carried out by obtaining the buckling loads of FE plates with and without the adhesive. Alternatively, a penalty method for the difference in stiffness in the unbonded and bonded regions could be applied. This method applies an artificial penalty for the solution of a problem if a constrain is violated. As the presence of the adhesive may act as a partial constraint at the very free edge of the plate, an iteration loop is implemented in the solution of the model until convergence is reached.

Lastly, the buckling modes predicted by the semi-analytical model were only reliable up to the transition between the first and second modes when compared to the FE analysis modes. The semi-analytical tool lost accuracy in this regard rapidly as aspect ratio increased.

8.1.2 Imperfection Modelling

The imperfection modelling results given by the semi-analytical tool also showed close compliance with the results to those from the FE models when comparing the out-of-plane displacements at the free edge. Although quantification of these results is difficult, observation of the effect of the imperfections on the buckling behavior of the plates from figures 7.14 and 7.15 demonstrate that the prediction of the out-of-plane displacement coefficients w_0 align with FE predictions. Unfortunately, the S-A model cannot include mode transition in its predictions, which have a rather large effect on the displacement coefficient values. This means that the current state of the semi-analytical model can only provide insight into the buckling loads, and not the post-buckling behavior of plates that have a transition in modes. Furthermore, the results from the pre-bent plate solution show that the S-A model overestimated the stiffness of the plate. As such, one must consider those unconservative results with care.

8.1.3 Skew angle

The semi-analytical model was unable to estimate the reduction in buckling loads due to the choice of solution for the displacement fields. While the choice of displacement fields as orthogonal trigonometric functions has the upside of simplifying the integration of the total potential energy equation, this orthogonality also drives stretching-shearing and bending-twisting terms to disappear. Solutions to the displacement fields compliant with the boundary conditions can be provided as non-trigonometric polynomials, which should not pose the issue of disappearing terms due to orthogonality.

All things considered, the semi-analytical model works well as a quick-and-easy tool to obtain a rough estimation of the buckling loads (within 30% confidence), which is useful when testing and optimizing different lay-up combinations and fiber orientations for the composite plates. However, there is much room for improvement. As far as the accuracy of the semi-analytical model goes, it is highly encouraged to improve it based on more advanced theory and previous plate models. Modelling curved composite shells is possible by including a curvature term [37] on the midplane strain relations below, where R is the respective radius of curvature:

$$\varepsilon_x^0 = u_x + \frac{1}{2}w_x^2 - \frac{w}{R} \quad \text{or} \quad \varepsilon_y^0 = v_y + \frac{1}{2}w_y^2 - \frac{w}{R} \tag{8.1}$$

8.2 Experimental Test Set-up

After the nylon pieces from the posterior clamp were remade with steel, the experimental test seemed to reflect well the predictions of the FE models up to early post-buckling loads. During pre-buckling, the experimental tests showed slightly higher pre-buckling stiffness as mentioned regarding

figures 7.16, 7.20 and 7.22. It was found that the connecting pieces from the sliding edges to the compression machine (figure 8.1) did not allow free rotation as the load was applying, artificially stiffening the system. These pieces must be fixed prior to carrying out future experimental tests.

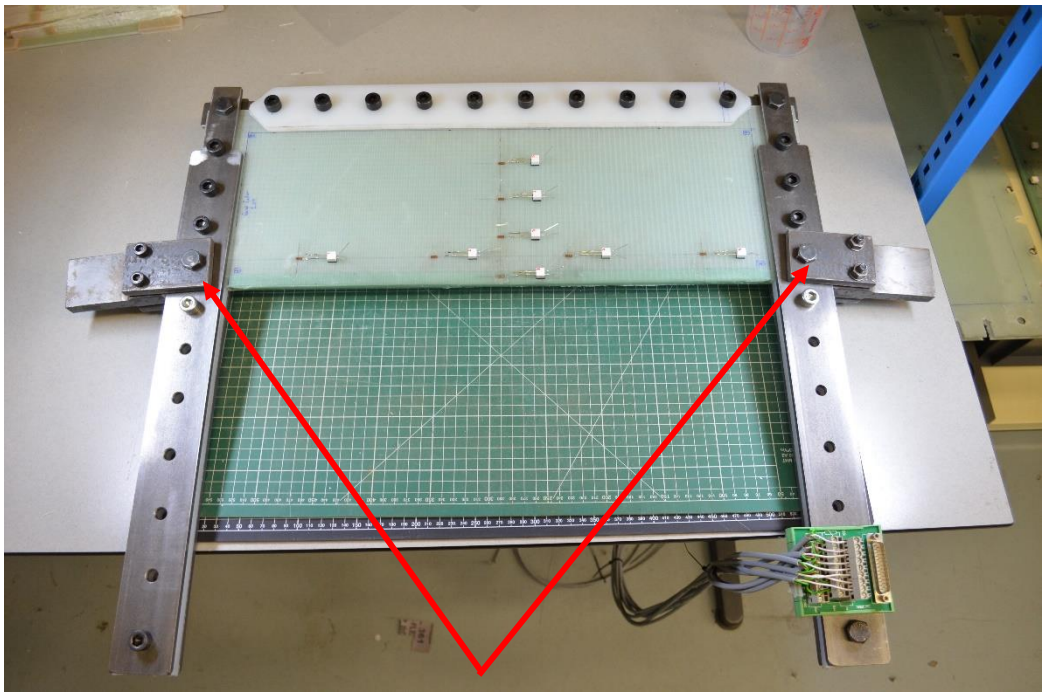

Figure 8.1 - Connection pieces from clamp system to compression machine that prevented free rotation during load application.

Unfortunately, higher post-buckling loads could not be compared due to loss of stiffness of the clamping system as a whole. Improved hinge sections of the clamp are required in order to keep a controlled test, especially if one of the end goals of the set-up is to reach debonding of the plates.

Adding to the previous point regarding debonding, despite the large buckling displacements of the plate it was surprising that no failure happened in the plate. The simplification of the trailing edge as parallel bonded plates played a major role in the lack of failure, as the whole specimen buckled globally. Local buckling of each plate separately reflects a more realistic cause for failure at the trailing edge. This may be induced by some factors such as pre-existent delaminations/debonded areas, as well as due to the opening angle between the composite panels. Including either (or both) of these factors in future studies is highly encouraged. Adding imperfectly bonded zones during bonding of the plates can be done and tested readily with the current clamping system. The opening angle between plates, on the other hand, would require more work. In actual blades, buckling at the trailing edge will differ between the pressure side and suction side panels in a way that the angle between them leading down to the adhesive joint may decrease or increase, leading to high stress concentrations on the adhesive, shearing, and early

crack initiation. While inclusion of this aspect is not possible with conventional methods for semi-analytical modelling to obtain a closed-form solution, it can easily be included in the FE analysis. With little modifications to the custom clamps, angled bonded panels may also be tested. This would require the mid pieces of the sliding clamps (groupID 3 from appendix E) to be changed to wedge shaped (triangular) pieces and realignment of the drilled holes for fastening.

A point of interest regarding the custom clamp is the ability of it to allocate skewed (and even trapezoidal) plates allowing for further variations of the parameters of the specimens. In fact, it is encouraged to manufacture and test a variety of skewed plated such that the results obtained from FE for skew angles $\Psi = 5°$ and $\Psi = 10°$ may be validated. From there on, a further study could be carried out by manufacturing plates with different skew angles to corroborate the FE model results and obtain more information for the plot of skew angle vs. loss in load-carrying capacity.

Finally, the second test from specimen TEB03 showed that each plate lost some structural integrity just after one buckling test. It would be interesting to carry out fatigue tests for a variety of specimens in order to test the response of the specimens to dynamic loading conditions and the loss of structural integrity/degradation stemming from these.

Chapter 9 – Conclusions & Future Work

9.1 Conclusions

The process of design and testing of wind turbine blades currently covers tests done at three different levels: Coupons, full-scale test and more recently, sub-component tests. Each of these tests have their advantages and limitations: coupon tests require a larger number of tests, but the complexity and costs are the lowest. On the other hand, sub-component and full-scale tests are highly complex, time consuming and expensive. Furthermore, while coupons provide statistical data on the mechanical properties of the materials, sub-component and full-scale tests include realistic loading conditions and magnitudes such that the blade and its components can be certified according to the established standards.

Tests at the elements & details at an intermediate level offer an acceptable trade-off, reducing complexity and costs while limiting themselves to the fulfillment of specific purposes. Developing a custom trailing edge experimental set-up and specimens was made to streamline a method of testing the effects that geometric and material properties may have on trailing edge buckling. The process spanned three main sections:

1) Developing a semi-analytical model using classical laminated plate theory and the principle of minimum potential energy in order to pave the understanding of the multitude of factors from which load bearing of a trailing edge adhesive joint depends.
2) Modelling in a Finite Element Analysis tool (MSC Marc Mentat) the clamping system and a variety of plates with varying dimensions (length a, width b), skew angle Ψ, twist β and a pre-bent deformation. These models served as the middle ground between the theoretical basis established by the semi-analytical model and the experimental tests.
3) Experimental tests that validated the results from the FE analysis and provided insight into the existent flaws of joint fixity of the clamps preventing from the desired performance.

Despite the fact that the results obtained from this research fell within a very narrow scope of criteria, the wide selection of methods employed (semi-analytical, numerical and experimental) and the agreement of critical buckling loads, pre-buckling behavior and proper implementation of boundary conditions demonstrate a solid foundation of the study. As such, the first general iteration of the element

& detail test can be considered to have satisfactory results and provided insight into what steps to take to improve in a future iteration of the research.

9.2 Future Work

Room for improvement of this research is vast and areas upon which this study can be improved are suggested:

1. A sturdier semi-analytical tool:
    1.1. An alternate solution to the displacement fields that do not have vanishing terms due to orthogonality. It was found that these are inappropriate solutions when dealing with coupling of displacement fields. Employing multi-term solutions, algebraic polynomials or hyperbolic trigonometric functions may complicate the derivation but improve the accuracy of the model.
    1.2. A comparison should be drawn out between the effective-length corrected simple supports and clamped boundary conditions.
    1.3. Ensure proper coupling of in-plane and out-of-plane displacement terms, which will ensure increasingly accurate results of the amplitude coefficients u_0, v_0 and w_0.
2. Current manufacturing/bonding practices:
    2.1. This study was made by ensuring the highest quality of the bond possible with available methods to ensure alignment of conditions between the FE and experimental methods. Current industry practices do not generally ensure the highest bonding quality possible. Inclusion of unbonded regions, air bubbles, uneven bondline during specimen manufacturing gives the possibility to capture more information regarding early failure due to these imperfections.
3. Improvement of current joint-fixity:
    3.1. By enforcing the hinged corners and preventing twisting of the posterior clamp, the post-buckling stage of the test can lead the specimen into debonding failure. At that point, the test set-up will be ready to evaluate different manufacturing defects on the composite plates or bond-line, or test out new material combinations/alignment.
4. Testing of various aspect ratios and skew angles:
    4.1. The clamp was designed in a way that it may allocate plates from any aspect ratios between $AR = 1$ to $AR = 5$. In addition, the hinged corners can accommodate skewed plates with a high range of angles. It was found that for the SSP34m blade, realistic skew angles that may be found on the blade are between $3.6°$ and $6.6°$
5. Inclusion of opening angle between composite panels in FE and experimental tests:

5.1. Re-design of GroupID 3 elements from the clamp (mid pieces of the sliding edges) as wedges. These can be then employed both in the manufacturing of the bonded panels as a spacer as well as the mid-piece of the sliding clamps.

Appendix A – Material properties

Biax 12 Type E Glass fiber	
E_{11}	26,000 MPa
E_{22}	26,000 MPa
E_{33}	13,190 MPa
μ_{12}	0.15
μ_{23}	0.15
μ_{31}	0.08
G_{12}	13535 MPa
G_{23}	3535 MPa
G_{31}	3535 MPa

Bonding paste Epikote/Epikure	
E	880 MPa
μ	0.35

Appendix B – SSP34m Blade thickness, chord length and chord distribution

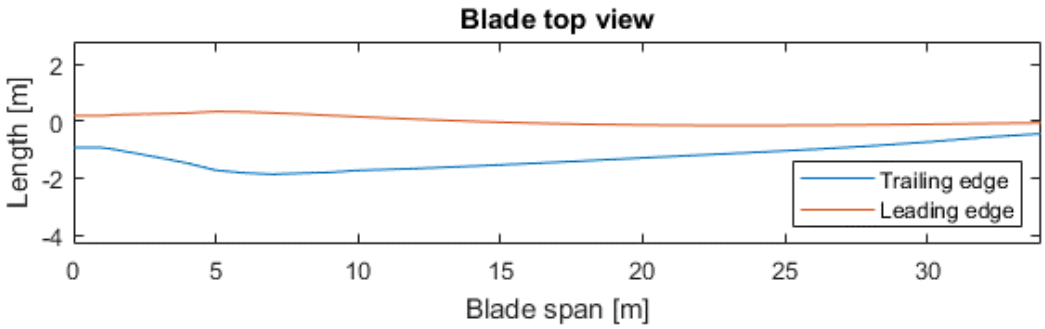

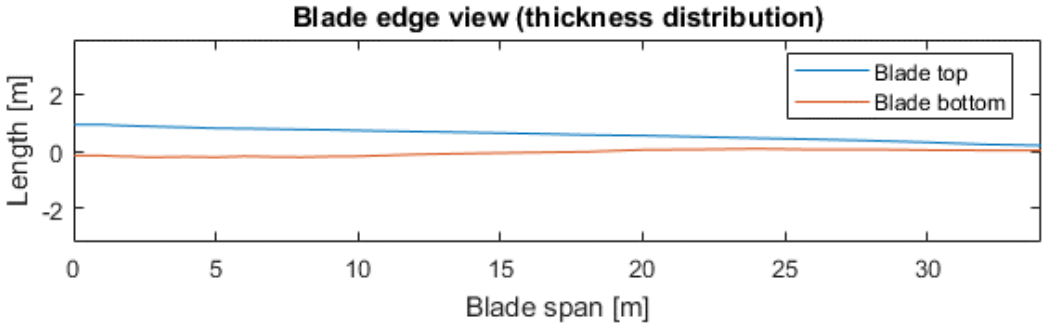

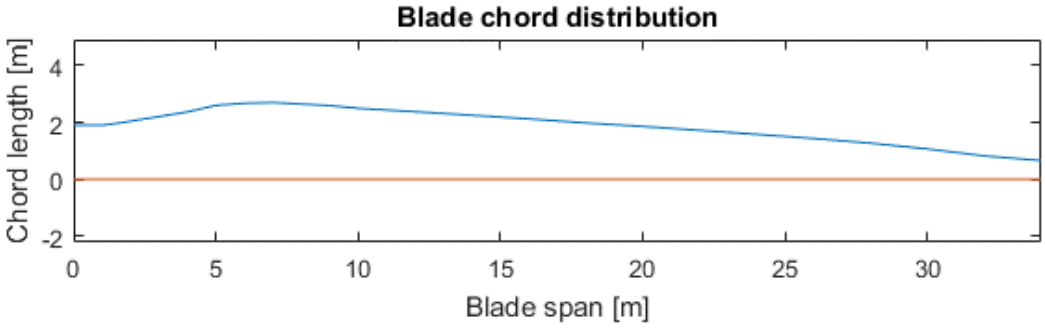

Appendix C – Potential Energy Equation term integration

In-Plane strain energy term integrations:

(A11 term)	
$\iint_A u_x^2\,dA = \frac{u_0^2 M^2 ab}{4}$	$\iint_A u_x w_x^2\,dA = \frac{u_0 w_0^2 M^3}{4}\left[\frac{2(1-\cos(\lambda\pi n))}{MN_\lambda}\right]$
$\iint_A \frac{w_x^4}{4}dA = \frac{w_0^4 M^4 ab}{256}\left[9 - \frac{12\sin(2\lambda\pi n)}{2\lambda\pi n} + \frac{3\sin(4\lambda\pi n)}{4\lambda\pi n}\right]$	
(A22 term)	
$\iint_A v_y^2\,dA = \frac{v_0^2 N_\lambda^2 ab}{4}$	$\iint_A v_y w_y^2\,dA = \frac{v_0 w_0^2 N_\lambda^3}{4}\left[\frac{2(\cos(\lambda\pi n)-1)}{MN_\lambda}\right]$
$\iint_A \frac{w_y^4}{4}dA = \frac{w_0^4 N_\lambda^4 ab}{256}\left[9 + \frac{12\sin(2\lambda\pi n)}{2\lambda\pi n} + \frac{3\sin(4\lambda\pi n)}{4\lambda\pi n}\right]$	
(A66 term)	
$\iint_A u_y^2\,dA = \frac{u_0^2 N_\lambda^2 ab}{4}$	$\iint_A v_x^2\,dA = \frac{v_0^2 M^2 ab}{4}$
$\iint_A w_x^2 w_y^2\,dA = \frac{w_0^4 M^2 N_\lambda^2 ab}{64}\left[1 - \frac{\sin(4\lambda\pi n)}{4\lambda\pi n}\right]$	$\iint_A 2u_y v_x\,dA = \frac{u_0 v_0 M N_\lambda ab}{2}$
$\iint_A 2u_y w_x w_y\,dA = \frac{u_0 w_0^2 M N_\lambda^2}{2}\left[\frac{2(1-\cos(\lambda\pi n))}{MN_\lambda}\right]$	$\iint_A 2v_x w_x w_y\,dA = \frac{v_0 w_0^2 M^2 N_\lambda}{2}\left[\frac{2(1-\cos(\lambda\pi n))}{MN_\lambda}\right]$
(A12 term)	
$\iint_A u_x v_y\,dA = 0$	$\frac{1}{2}\iint_A u_x w_y^2\,dA = \frac{u_0 w_0^2 M N_\lambda^2}{8}\left[\frac{2(\cos(\lambda\pi n)-1)}{MN_\lambda}\right]$
$\frac{1}{2}\iint_A v_y w_x^2\,dA = \frac{v_0 w_0^2 M^2 N_\lambda}{8}\left[\frac{2(\cos(\lambda\pi n)-1)}{MN_\lambda}\right]$	$\frac{1}{4}\iint_A w_x^2 w_y^2\,dA = \frac{w_0^4 M^2 N_\lambda^2 ab}{256}\left[1 - \frac{\sin(4\lambda\pi n)}{4\lambda\pi n}\right]$
(A16 term)	
$\iint_A u_x u_y\,dA = 0$	$\iint_A u_x v_x\,dA = 0$
$\iint_A u_x w_x w_y\,dA = 0$	$\frac{1}{2}\iint_A u_y w_x^2\,dA = \frac{u_0 w_0^2 M^2 N_\lambda}{8}\left[\frac{2(1-\cos(\lambda\pi n))}{MN_\lambda}\right]$
$\frac{1}{2}\iint_A v_x w_x^2\,dA = 0$	$\frac{1}{2}\iint_A w_x^3 w_y\,dA = 0$
(A26 term)	
$\iint_A v_y u_y\,dA = 0$	$\iint_A v_x v_y\,dA = 0$
$\iint_A v_y w_x w_y\,dA = 0$	$\frac{1}{2}\iint_A u_y w_y^2\,dA = 0$
$\frac{1}{2}\iint_A v_x w_y^2\,dA = 0$	$\frac{1}{2} w_x w_y^3 dA = 0$

Out-of-plane (curvature) strain energy terms:

(D11 term)	(D22 term)
$\iint_A w_{xx}^2\,dA = \frac{w_0^2 M^4 ab}{4}$	$\iint_A w_{yy}^2\,dA = \frac{w_0^2 N_\lambda^4 ab}{4}$
(D12 term)	**(D66 term)**
$\iint_A 2w_{xx}w_{yy}\,dA = 2\frac{w_0^2 M^2 N_\lambda^2 ab}{4}$	$\iint_A (2w_{xy})^2\,dA = 4\frac{w_0^2 M^2 N_\lambda^2 ab}{4}$
(D16 term)	**(D26 term)**
$\iint_A 2w_{xx}w_{xy}\,dA = 0$	$\iint_A 2w_{yy}w_{xy}\,dA = 0$

External Work terms

Nx term

$\iint_A (w_x)^2\,dA = \frac{w_0^2 M^2 ab}{4}$	

$$\Pi = \frac{1}{2}\left[A_{11}\left\{\frac{u_0^2 M^2 ab}{4} + \frac{u_0 w_0^2 M^3}{4}\left[\frac{2(1-\cos(\lambda\pi n))}{MN_\lambda}\right] + \frac{w_0^4 M^4 ab}{256}\left[9 - \frac{12\sin(2\lambda\pi n)}{2\lambda\pi n} + \frac{3\sin(4\lambda\pi n)}{4\lambda\pi n}\right]\right\}\right.$$
$$+2A_{12}\left\{\frac{u_0 w_0^2 M N_\lambda^2}{8}\left[\frac{2(\cos(\lambda\pi n)-1)}{MN_\lambda}\right] + \frac{v_0 w_0^2 M^2 N_\lambda}{8}\left[\frac{2(\cos(\lambda\pi n)-1)}{MN_\lambda}\right] + \frac{w_0^4 M^2 N_\lambda^2 ab}{256}\left[1 - \frac{\sin(4\lambda\pi n)}{4\lambda\pi n}\right]\right\}$$
$$+2A_{16}\left\{\frac{u_0 w_0^2 M^2 N_\lambda}{8}\left[\frac{2(1-\cos(\lambda\pi n))}{MN_\lambda}\right]\right\}$$
$$+A_{22}\left\{\frac{v_0^2 N_\lambda^2 ab}{4} + \frac{v_0 w_0^2 N_\lambda^3}{4}\left[\frac{2(\cos(\lambda\pi n)-1)}{MN_\lambda}\right] + \frac{w_0^4 N_\lambda^4 ab}{256}\left[9 + \frac{12\sin(2\lambda\pi n)}{2\lambda\pi n} + \frac{3\sin(4\lambda\pi n)}{4\lambda\pi n}\right]\right\}$$
$$+A_{66}\left\{\frac{u_0^2 N_\lambda^2 ab}{4} + \frac{v_0^2 M^2 ab}{4} + \frac{w_0^4 M^2 N_\lambda^2 ab}{64}\left[1 - \frac{\sin(4\lambda\pi n)}{4\lambda\pi n}\right] + \frac{u_0 v_0 M N_\lambda ab}{2}\right.$$
$$\left.+\frac{u_0 w_0^2 M N_\lambda^2}{2}\left[\frac{2(1-\cos(\lambda\pi n))}{MN_\lambda}\right] + \frac{v_0 w_0^2 M^2 N_\lambda}{2}\left[\frac{2(1-\cos(\lambda\pi n))}{MN_\lambda}\right]\right\}$$
$$\left.+D_{11}\left\{\frac{w_0^2 M^4 ab}{4}\right\} + 2(D_{12}+2D_{66})\left\{\frac{w_0^2 M^2 N_\lambda^2 ab}{4}\right\} + D_{22}\left\{\frac{w_0^2 N_\lambda^4 ab}{4}\right\}\right]$$
$$-\frac{1}{2}\left[N_x\left\{\frac{w_0^2 M^2 ab}{4}\right\}\right]$$

A term pertaining to the free edge coefficient λ shows up in various points throughout the derivation, which will be shown as Λ from now onwards, which is only present when 'm' is an even number, and equal to zero otherwise (due to orthogonality properties of the displacement fields during integration):

$$\Lambda = \left[\frac{2(1-\cos(\lambda\pi n))}{MN_\lambda}\right]$$

Appendix D – Potential Energy C_{xx} terms for sliding Edges

$$C_{11} = \left[\frac{A_{11}M^2ab}{2} + \frac{A_{66}N_\lambda^2 ab}{2}\right]$$

$$C_{12} = \left[\frac{A_{66}MN_\lambda ab}{2}\right]$$

$$C_{13} = \left[\frac{A_{11}M^3}{4} - \frac{A_{12}MN_\lambda^2}{4} + \frac{A_{16}M^2N_\lambda}{4} + \frac{A_{66}MN_\lambda^2}{2}\right]\Lambda$$

$$C_{21} = \left[\frac{A_{66}MN_\lambda ab}{2}\right]$$

$$C_{22} = \left[\frac{A_{22}N_\lambda^2 ab}{2} + \frac{A_{66}M^2ab}{2}\right]$$

$$C_{23} = \left[\frac{A_{66}M^2N_\lambda}{2} - \frac{A_{22}N_\lambda^3}{4} - \frac{A_{12}M^2N_\lambda}{4}\right]\Lambda$$

$$C_{31} = \left[\frac{A_{11}M^3}{2} - \frac{A_{12}MN_\lambda^2}{2} - \frac{A_{16}M^2N_\lambda}{2} + A_{66}M^2N_\lambda\right]\Lambda$$

$$C_{32} = \left[A_{66}M^2N_\lambda - \frac{A_{12}M^2N_\lambda}{2} - \frac{A_{22}N_\lambda^3}{2}\right]\Lambda$$

$$C_{33} = \left[\frac{A_{11}M^4ab}{64}\left(9 - \frac{12\sin(2\lambda\pi n)}{2\lambda\pi n} + \frac{3\sin(4\lambda\pi n)}{4\lambda\pi n}\right) + \frac{(A_{12}+A_{66})M^2N_\lambda^2 ab}{16}\left(1 - \frac{\sin(4\lambda\pi n)}{4\lambda\pi n}\right) + \frac{A_{22}N_\lambda^4 ab}{64}\left(9 + \frac{12\sin(2\lambda\pi n)}{2\lambda\pi n} + \frac{3\sin(4\lambda\pi n)}{4\lambda\pi n}\right)\right]$$

$$C_{34} = \left[\frac{D_{11}M^4ab}{2} + 2(D_{12}+2D_{66})M^2N_\lambda^2 ab + \frac{D_{22}N_\lambda^4 ab}{2}\right]$$

$$C_{35} = \left[\frac{M^2ab}{2}\right]$$

$$C_{41} = -0.5749\, w_0\beta_m mb^2\left[\frac{\sin(\beta_m a - m\pi)}{(\beta_m a - m\pi)} + \frac{\sin(\beta_m a + m\pi)}{(\beta_m a + m\pi)}\right] \; for\ twist$$

$$C_{41} = 2.9386\, w_{ini}w_0\left(\frac{b}{a}\right) \; for\ m = 1\ for\ prebent\ plate$$

Appendix E – Clamp Design

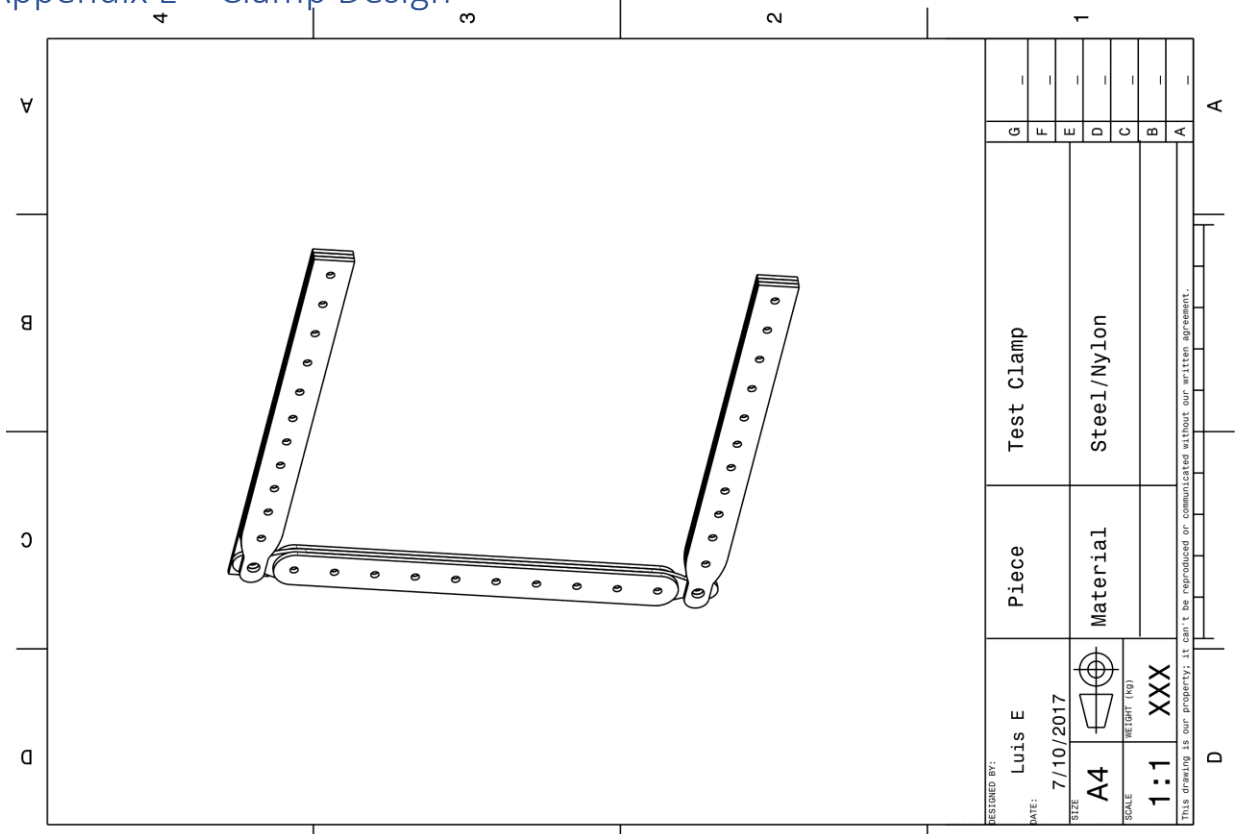

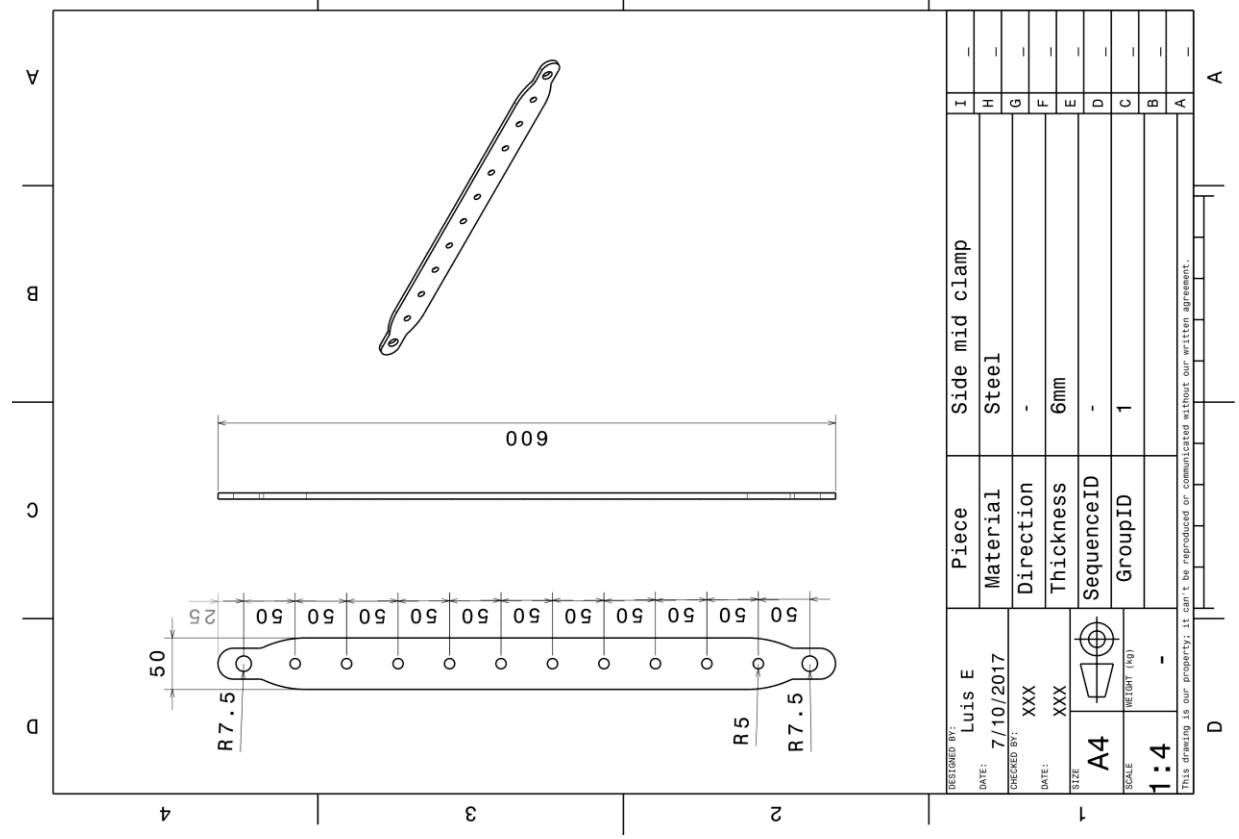

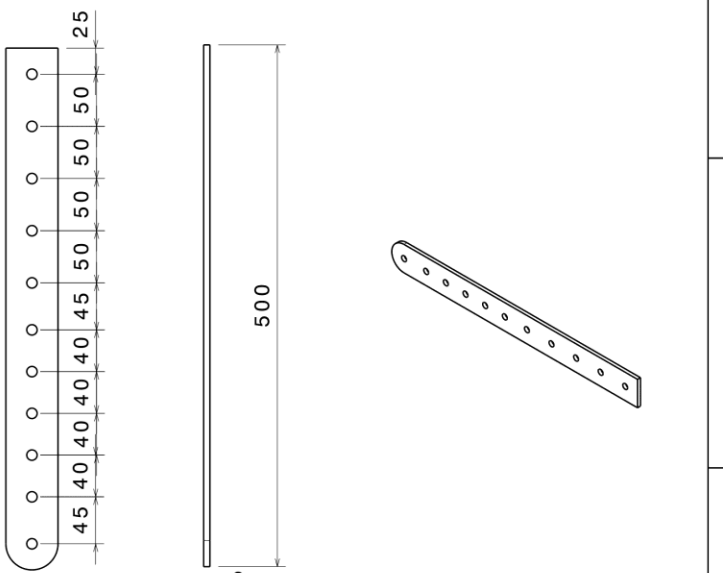

DESIGNED BY: Luis E	Piece	Edge mid clamp	I _
DATE: 7/10/2017	Material	Nylon	H _
CHECKED BY: XXX	Direction	-	G _
DATE: XXX	Thickness	6mm	F _
SIZE A4	SequenceID	-	E _
SCALE 1:4	GroupID	3	D _
WEIGHT (kg) XXX			C _
			B _
			A _

This drawing is our property; it can't be reproduced or communicated without our written agreement.

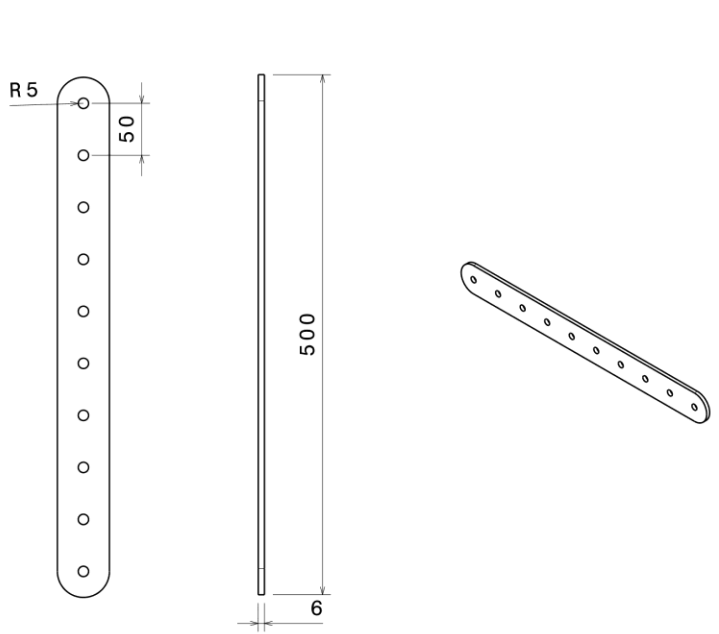

DESIGNED BY: Luis E	Piece	Side left/right	I _
DATE: 7/10/2017	Material	Nylon	H _
CHECKED BY: XXX	Direction	-	G _
DATE: XXX	Thickness	6mm	F _
SIZE A4	SequenceID	-	E _
SCALE 1:4	GroupID	2	D _
WEIGHT (kg) XXX			C _
			B _
			A _

This drawing is our property; it can't be reproduced or communicated without our written agreement.

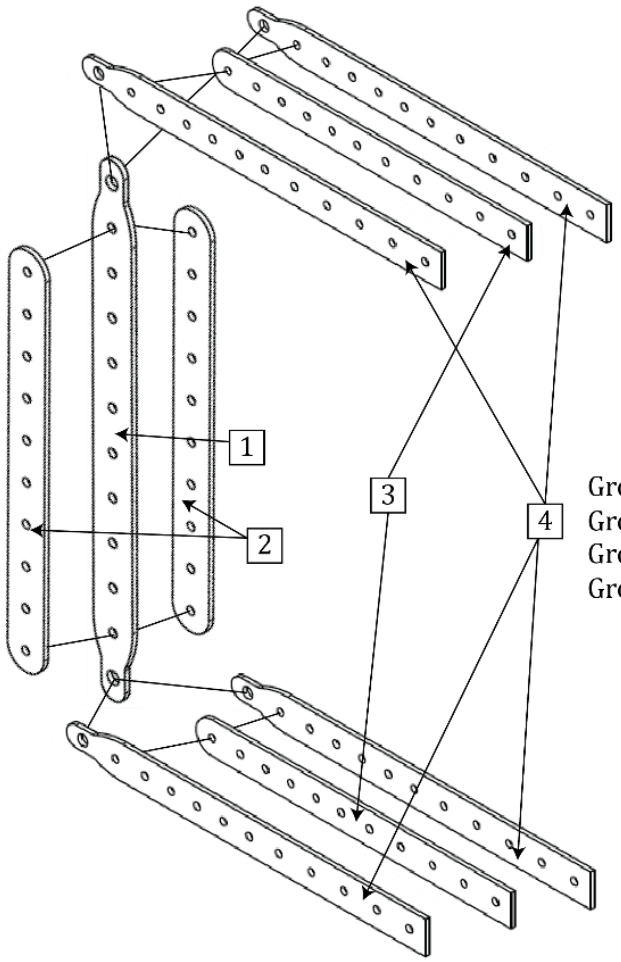

GroupID 1 - Steel
GroupID 2 - Nylon
GroupID 3 - Nylon
GroupID 4 - Steel

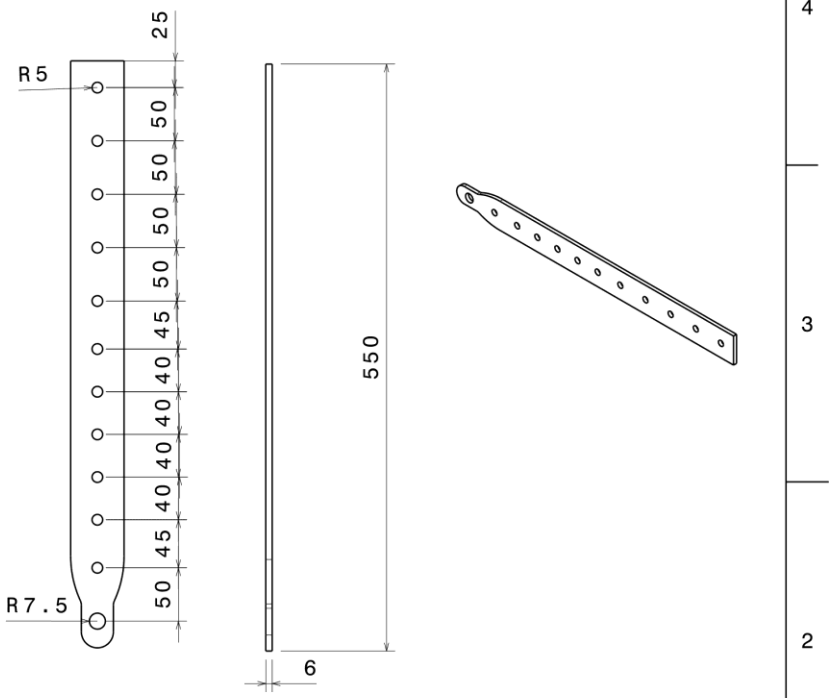

DESIGNED BY: Luis E	Piece	Edge left/right	I _
DATE: 7/10/2017	Material	Steel	H _
CHECKED BY: XXX	Direction	-	G _
DATE: XXX	Thickness	6mm	F _
SIZE A4	SequenceID	-	E _
	GroupID	4	D _
SCALE 1:4	WEIGHT (kg) XXX		C _
			B _
			A _

Appendix F – Experimental Specimens Measured Dimensions

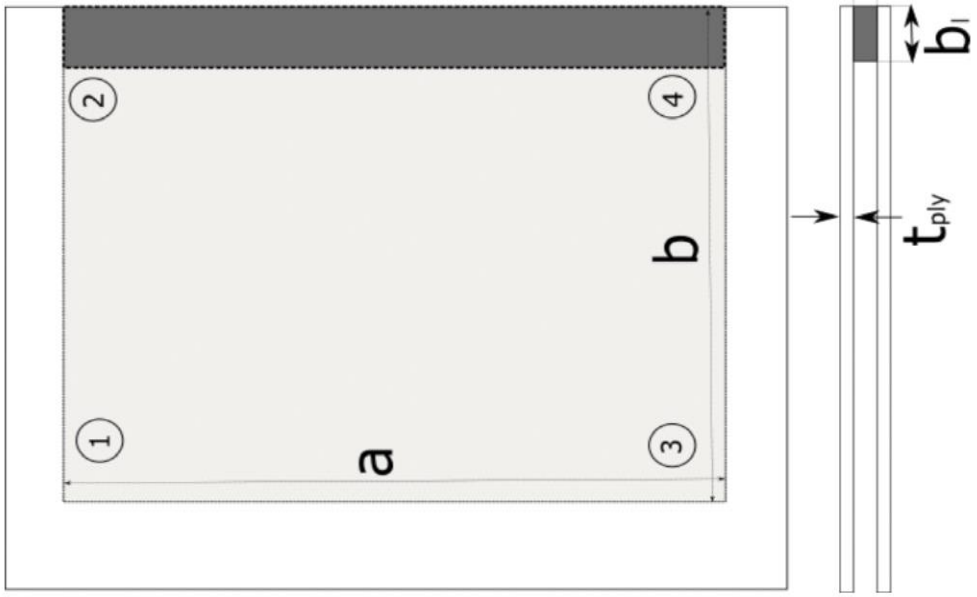

	a		b		b_l		b_t		t_{ply} left panel				t_{ply} right panel			
Specimen	1-3	2-4	1-2	3-4	2	4	2	4	1	2	3	4	1	2	3	4
TEB01	49.9	50.0	16.6	16.5	1.219	1.214	0.654	0.665	0.285	0.281	0.278	0.281	0.28	0.28	0.285	0.283
TEB02	49.8	49.7	16.5	16.5	1.238	1.582	0.705	0.697	0.276	0.273	0.265	0.278	0.275	0.272	0.277	0.272
TEB03	49.7	49.8	16.6	16.5	1.272	1.205	0.693	0.697	0.27	0.27	0.262	0.26	0.266	0.264	0.261	0.267

Appendix G – Plotted raw data

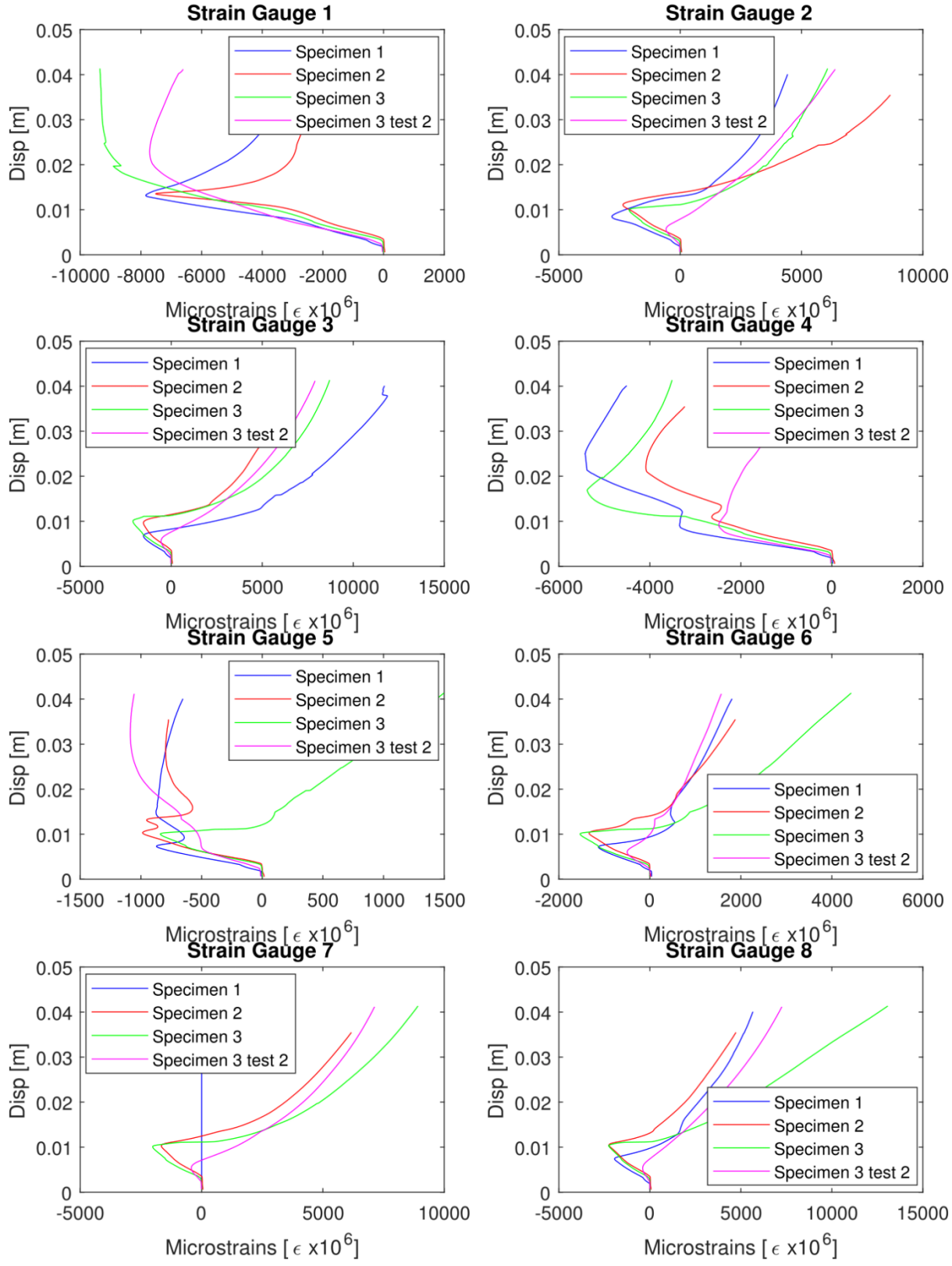

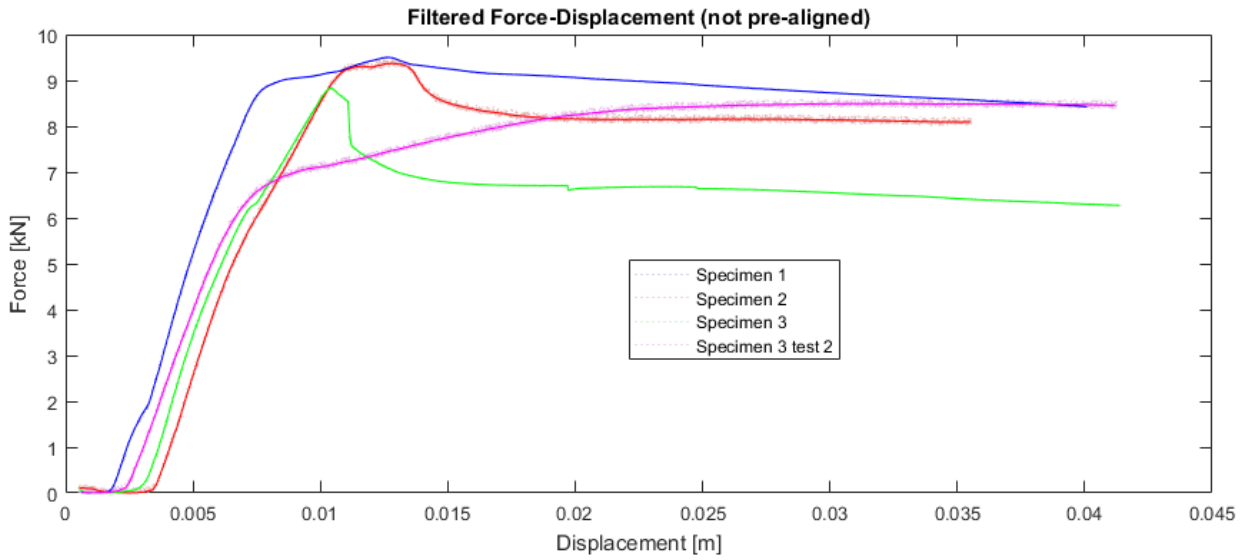
Filtered Force-Displacement (not pre-aligned)
Force [kN]
Displacement [m]
Specimen 1
Specimen 2
Specimen 3
Specimen 3 test 2
0
1
2
3
4
5
6
7
8
9
10
0
0.005
0.01
0.015
0.02
0.025
0.03
0.035
0.04
0.045

Appendix H – Buckling Modes of FE models.

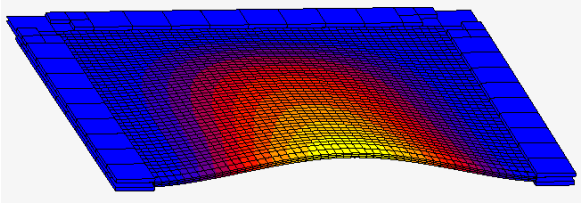

$AR = 1\ m = 1\ N^* = 7{,}350kN$

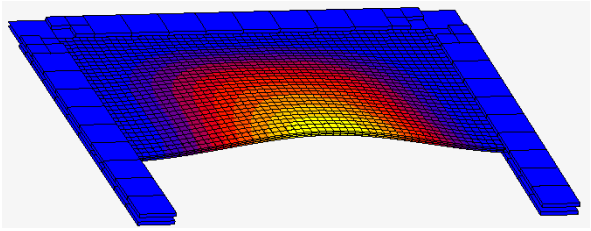

$AR = 1.5\ m = 1\ N^* = 6{,}500kN$

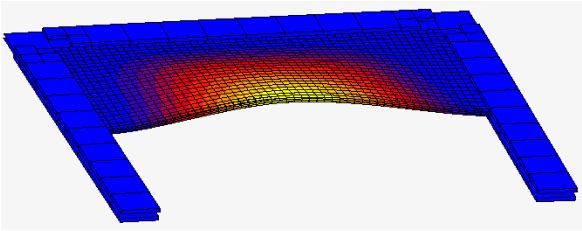

$AR = 2\ m = 1\ N^* = 7{,}210$

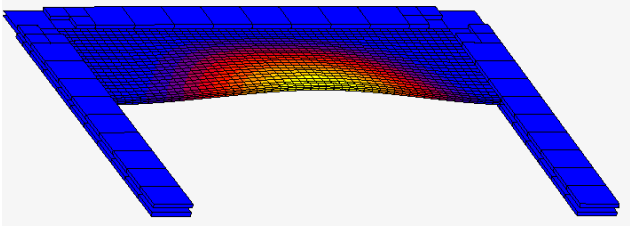

$AR = 2.5\ m = 1\ N^* = 8{,}540kN$

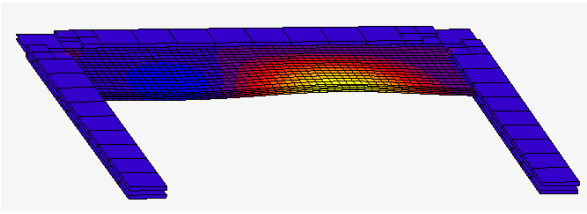

$AR = 3\ m = 1\ N^* = 10{,}620kN$

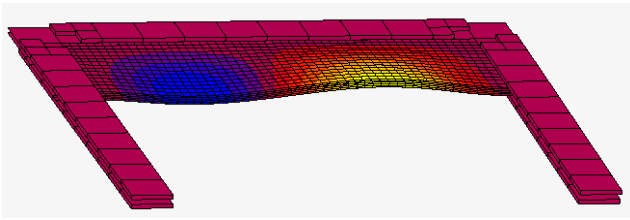

$AR = 3\ m = 2\ N^* = kN$

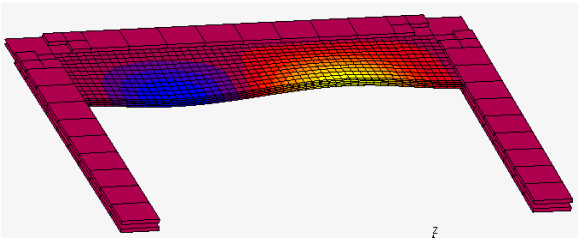

$AR = 3.5\ m = 2\ N^* = 11{,}420kN$

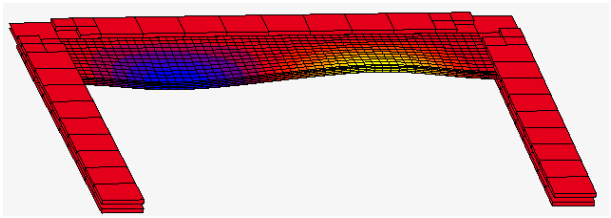

$AR = 4\ m = 2\ N^* = 12{,}900kN$

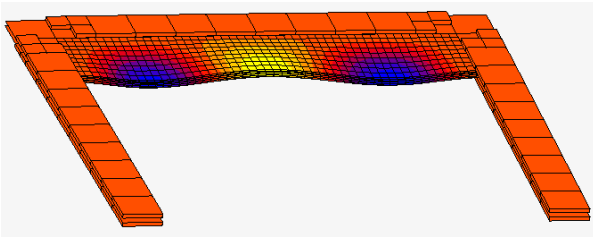

$AR = 4.5\ m = 3\ N^* = 14{,}100kN$

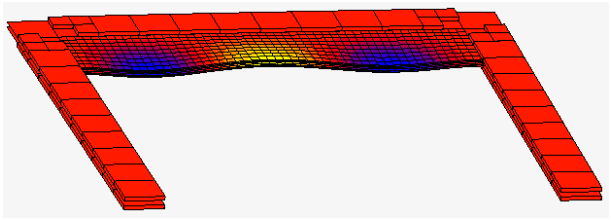

$AR = 5\ m = 3\ N^* = 16{,}150kN$

MATLAB Code – Semi-analytical Model (not exhaustive)

```
%%%%%%%%%%%%%%%% plate_model_main.m
clear all
close all
clc

%%%%%%%%%%%%%%%%%%%%%%%%%%%%%%%%%%%%%%%%%%%%
%% MOTHER FILE --- Plate model RRM       %%
%% By. Luis Espinosa                     %%
%% EWEM Thesis          6-12-2017        %%
%%%%%%%%%%%%%%%%%%%%%%%%%%%%%%%%%%%%%%%%%%%%

%% Read material database input file and import table

[mat_num,mat_txt]=xlsread('material_db.xlsx');

%% Read plate dimension input file and import table

[pl_num,pl_txt]=xlsread('plate_dim.xlsx');

case_tot=size(pl_num,1);

for Dom=1:case_tot %Domain: cases specified on input file plate_dim

    clearvars -except pl_num pl_txt mat_num mat_txt case_tot Dom Ncr_ar_ss
Ncr_ar_eff

    Psi=pl_num(Dom,10);

    run('material_stiffness2.m')

    ARmax=pl_num(Dom,7);
    AR_=(0.1:0.1:ARmax)';

    for ar=1:length(AR_)
        run('ar_dim.m')
        run('improved_rrSS.m')
        Ncr_ar_ss(ar,Dom)=min(N_cr_ss(ar,:));
    end
xlswrite('Wout ssAR5',[N,w_out_s])
    for ar=1:length(AR_)
        run('ar_dim2.m')
        run('improved_rrEFF.m')
        Ncr_ar_eff(ar,Dom)=min(N_cr_eff(ar,:));
    end
xlswrite('Wout efAR5',[N,w_out_ef])

end
```

```
%%%%%%%%%%%%%%%%%%%%%%%%%%%%%%%%%%%%%%%%%%%%%%%%
%% material_stiffness2.m                        %%
%% By. Luis Espinosa                            %%
%% EWEM Thesis           5-01-2017              %%
%%%%%%%%%%%%%%%%%%%%%%%%%%%%%%%%%%%%%%%%%%%%%%%%

% %% Read material database input file and import table
%
% [mat_num,mat_txt]=xlsread('material_db.xlsx');
%
% %% Read plate dimension input file and import table
%
% [pl_num,pl_txt]=xlsread('plate_dim.xlsx');

%% Build mat_prop matrix
mat_tab=mat_txt(:,1);

mat_fs=string(char(pl_txt(1+Dom,1)));

mat_c=string(char(pl_txt(1+Dom,3)));

fs_row=find(ismember(mat_tab,mat_fs))-1;
c_row=find(ismember(mat_tab,mat_c))-1;

% Build matrix with columns as follows:
%|   (i,1)   |   (i,2)   |   (i,3)   |   (i,4)   |   (i,5)   |   (i,6)   |
%     Exx         Eyy         Ezz         Gxy         Gyz         Gzx
%|   (i,7)   |   (i,8)   |   (i,9)   |   (i,10)  |   (i,11)  |   (i,12)  |
%     muxy        muyz        muzx      sig_t_xx   sig_t_yy    sig_t_zz
%|   (i,13)  |   (i,14)  |   (i,15)  |   (i,16)  |   (i,17)  |   (i,18)  |
%  sig_c_xx    sig_c_yy    sig_c_zz     tau_xy      tau_yz      tau_zx
%|   (i,19)  |   (i,20)  |
%    Vol.W         h

mat_prop(1,:)=mat_num(fs_row,:);
mat_prop(2,:)=mat_num(c_row,:);

mat_prop(:,end+1)=[pl_num(Dom,1);pl_num(Dom,3)];

%% Calculation of material stiffness

for i=1:2

    muyx=mat_prop(i,2)/mat_prop(i,1)*mat_prop(i,7);
    muzy=mat_prop(i,3)/mat_prop(i,2)*mat_prop(i,8);
    muxz=mat_prop(i,1)/mat_prop(i,3)*mat_prop(i,9);

    detm=(1-mat_prop(i,7)*muyx-mat_prop(i,8)*muzy-mat_prop(i,9)*muxz-
2*muyx*muzy*muxz)/(mat_prop(i,1)*mat_prop(i,2)*mat_prop(i,3));

    Q11=(1-mat_prop(i,8)*muzy)/(mat_prop(i,2)*mat_prop(i,3)*detm);

Q12=(muyx+mat_prop(i,8)*mat_prop(i,9))/(mat_prop(i,2)*mat_prop(i,3)*detm);
```

```
    Q13=(mat_prop(i,9)+muyx*muzy)/(mat_prop(i,2)*mat_prop(i,3)*detm);

    Q22=(1-mat_prop(i,9)*muxz)/(mat_prop(i,1)*mat_prop(i,3)*detm);

Q23=(muzy+mat_prop(i,7)*mat_prop(i,9))/(mat_prop(i,1)*mat_prop(i,3)*detm);

    Q33=(1-mat_prop(i,7)*muyx)/(mat_prop(i,2)*mat_prop(i,3)*detm);

    Q44=(mat_prop(i,5));
    Q55=(mat_prop(i,6));
    Q66=(mat_prop(i,4));

    Q_mat(:,:,i)=[Q11 Q12 Q13 0 0 0;
                  Q12 Q22 Q23 0 0 0;
                  Q13 Q23 Q33 0 0 0;
                   0   0   0  Q44 0 0;
                   0   0   0   0 Q55 0;
                   0   0   0   0  0 Q66];

    Q_mat3(:,:,i)=[Q11 Q12 0;
                   Q12 Q22 0;
                   0   0   Q66];

    S_mat(:,:,i)=inv(Q_mat(:,:,i));

    if mat_prop(i,2)==0
        Q_mat(:,:,i)=zeros(6);
        Q_mat3(:,:,i)=zeros(3);
    end

    %% Rotation matrix

R_mat=[cosd(Psi)^2 sind(Psi)^2 2*cosd(Psi)*sind(Psi);
         sind(Psi)^2 cosd(Psi)^2 -2*cosd(Psi)*sind(Psi);
         -cosd(Psi)*sind(Psi) cosd(Psi)*sind(Psi) cosd(Psi)^2-sind(Psi)^2];

M_mat(:,:,i)=R_mat*Q_mat3(:,:,i)*R_mat';

end

%% Calculation of ply thickness and k-th ply interfaces Zk[lower upper]

T_pl=0;
mat=[1;2;1];
for k=1:3
    T_pl=T_pl+(mat_prop(mat(k,1),20));
end

Zk=[-T_pl/2,-T_pl/2+mat_prop(1,20);
    -T_pl/2+mat_prop(1,20),-T_pl/2+mat_prop(1,20)+mat_prop(2,20);
    -T_pl/2+mat_prop(1,20)+mat_prop(2,20),-
T_pl/2+mat_prop(1,20)*2+mat_prop(2,20)];

z_ply=[Zk(1,1);Zk(2,1);Zk(2,2);Zk(3,2)];
```

```
%% Calculation of ABD matrix and abd (not assuming symmetric nor balanced
plate)

    A=0;
    B=0;
    D=0;

for i=1:length(Zk)
    A=A+(M_mat(:,:,mat(i,1))*(Zk(i,2)-Zk(i,1)));
    B=B+1/2*(M_mat(:,:,mat(i,1))*(Zk(i,2)^2-Zk(i,1)^2));
    D=D+1/3*(M_mat(:,:,mat(i,1))*(Zk(i,2)^3-Zk(i,1)^3));
end

A1=[A(1,1) A(1,2) A(1,3);
   A(2,1) A(2,2) A(2,3);
   A(3,1) A(3,2) A(3,3)];
B=[B(1,1) B(1,2) B(1,3);
   B(2,1) B(2,2) B(2,3);
   B(3,1) B(3,2) B(3,3)];
D=[D(1,1) D(1,2) D(1,3);
   D(2,1) D(2,2) D(2,3);
   D(3,1) D(3,2) D(3,3)];

ABD=[A1 B; B D];

alp=inv(A1)+inv(A1)*B*inv(D-B*inv(A1)-B)*B*inv(A1);
beta=-A1*B*inv(D-B*inv(A1)*B);
delta=inv(D-B*inv(A1)*B);

abd=[alp beta; beta delta];

%%%%%%%%%%%%%%%%%%%%%%%%%%%%%%%%%%%%%%%%%%%%%%%%
%% ar_dim.m                                     %%
%% By. Luis Espinosa                            %%
%% EWEM Thesis           5-01-2017              %%
%%%%%%%%%%%%%%%%%%%%%%%%%%%%%%%%%%%%%%%%%%%%%%%%

c=pl_num(Dom,4);
a=pl_num(Dom,5);
bpm=pl_num(Dom,6);   % for better automatization, input twist dist and r/R
and have MATLAB calculate the betapm at such point.

a_n=pl_num(Dom,8);
b_n=pl_num(Dom,9);
Psi=pl_num(Dom,10);  % for better automatization, input chord distribution in
plate_dim.xlsx and have MATLAB calulate psi according to a & c-dist

b=a/AR_(ar);      %% may not be optimal position to calculate

x=linspace(0,a,a_n)';
y=linspace(0,b,b_n)';
```

```
%%%%%%%%%%%%%%%%%%%%%%%%%%%%%%%%%%%%%%%%%%%%%%%%
%% improved_rrSS.m --- Plate model RRM   %%
%% By. Luis Espinosa                     %%
%% EWEM Thesis          6-12-2017        %%
%%%%%%%%%%%%%%%%%%%%%%%%%%%%%%%%%%%%%%%%%%%%%%%%
clear w q_ite
mMax=5;       %maximum mode to solve for
nMax=1;       %width-wise mode n=1
lamb=5/12;    %lambda value for free edge
Beta=bpm*pi/180; %twist value to radians

A11=A1(1,1);
A12=A1(1,2);
A22=A1(2,2);
A16=A1(1,3);
A26=A1(2,3);
A66=A(3,3);
D11=D(1,1);
D12=D(1,2);
D22=D(2,2);
D16=D(1,3);
D26=D(2,3);
D66=D(3,3);

for m=1:mMax

    M=m*pi/a;             %M factor for stability equation coefficients
    Nlamb=lamb*pi/b;      %N_lambda factor for stability equation
coefficients;


    if m==1 || m==3 || m==5 || m==7        %\Lambda factor from certain terms
dependent on m
        LAMB=0;
    elseif m==2 || m==4 || m==6 || m==8
        LAMB=(2*(1-cos(lamb*pi)/(M*Nlamb)));
    end


    C12=[A66*M*Nlamb*a*b/2];
    C13=[A11*M^3/4-A12*M*Nlamb^2/4+A16*M^2*Nlamb/4+A66*M*Nlamb^2/2]*LAMB;

    C21=[A66*M*Nlamb*a*b/2];
    C22=[A22*Nlamb^2*a*b/2+A66*M^2*a*b/2];
    C23=[A66*M^2*Nlamb/2-A22*Nlamb^3/4-A12*M^2*Nlamb/4]*LAMB;

    C31=[A11*M^3/2-A12*M*Nlamb^2/2-A16*M^2*Nlamb/2+A66*M^2*Nlamb]*LAMB;
    C32=[A66*M^2*Nlamb-A12*M^2*Nlamb/2-A22*Nlamb^3/2]*LAMB;
    C33a=[A11*M^4*a*b/64*(9-
12*sin(2*lamb*pi)/(2*lamb*pi)+3*sin(4*lamb*pi)/(4*lamb*pi))];
    C33b=[(A12+A66)*M^2*Nlamb^2*a*b/16*(1-sin(4*lamb*pi)/(4*lamb*pi))];

C33c=[A22*Nlamb^4*a*b/64*(9+12*sin(2*lamb*pi)/(2*lamb*pi)+3*sin(4*lamb*pi)/(4
*lamb*pi))];
```

```
    C33=C33a+C33b+C33c;

    C34=[D11*M^4*a*b/2+2*(D12+2*D66)*M^2*Nlamb^2*a*b+D22*Nlamb^4*a*b/2];
    C35=[M^2*a*b/2];

    C41=0;

    eps=1e-7;                           %Error threshold for Newton-Raphson

    N=linspace(0,3e5,2e4)';             %Load increments to be solved for
(NOTE: code behaves erratically if load increments are not small enough or
N(end) is not high enough.
    q=0;                                %reset load increment number q

    for q=1:length(N)
        ite=1;                          %set iteration number to 1
        wq=1;                           %initial w_0(q) coefficient
prediction
        wq1=0;                          %w_0(q+1)
        check=1;                        %initial error value

        while check>=eps                %iteration loop while error is above
threshold

            C11=[A11*M^2*a*b/2+A66*Nlamb^2*a*b/2-0*N(q)*M^2*a*b/4];
            K1=-(C12*(C21*C13)/C11-C23)/(C11*(C22-C21*C12/C11))-C13/C11;
            K2=(C21*C13/C11-C23)/(C22-C21*C12/C11);
            K3=(C34-N(q)*C35);
            wq1=wq-
((C31*K1+C32*K2+C33)*wq^3+K3*wq+C41)/(3*(C31*K1+C32*K2+C33)*wq^2+K3);
%Newton-Raphson w_0(q+1)=w_0(q)-f(w_0(q))/f'(w_0(q))

            check=abs(wq1-wq);          %error between w_0(q) and w_0(q+1)

            if check<eps || check==0    %Capture no. of iterations and w_0
when convergence is reached
                w(q)=wq1;
                q_ite(q)=ite;
            end
            wq=wq1;                     %update w_0(q) value
            ite=ite+1;                  %increase iteration number
        end

    end

    w_out(:,ar)=w;                      %capturing w_0 values for integer
aspect ratios. NOTE: dependent on chosen length of aspect ratio vector, may
break code if changed.
        if ar==10
            w_out_s(:,1)=w;
        elseif ar==20
            w_out_s(:,2)=w;
        elseif ar==30
            w_out_s(:,3)=w;
        elseif ar==40
```

```
            w_out_s(:,4)=w;
        elseif ar==50
            w_out_s(:,5)=w;
        else
        end

        for q=1:length(w)-1
            Ndiff(q)=(w(q+1)-w(q))/w(end);
        end

        Npos=min(find(Ndiff==max(Ndiff)));  %Find minimum value of N_cr for
all modes

        N_cr_ss(ar,m)=2*N(Npos)*b;          %Apply correction factor from
chapter 6 (2*Nsa*b)
        M_buck(ar,1)=m;                     %capture buckling mode for each
aspect ratio

end


%%%%%%%%%%%%%%%%%%%%%%%%%%%%%%%%%%%%%%%%%%%%%%%%
%% ar_dim2.m (effective length)          %%
%% By. Luis Espinosa                     %%
%% EWEM Thesis          5-01-2017        %%
%%%%%%%%%%%%%%%%%%%%%%%%%%%%%%%%%%%%%%%%%%%%%%%%

c=pl_num(Dom,4);
a=pl_num(Dom,5)*0.65;
bpm=pl_num(Dom,6);   % for better automatization, input twist dist and r/R
and have MATLAB calculate the betapm at such point.

a_n=pl_num(Dom,8);
b_n=pl_num(Dom,9);
Psi=pl_num(Dom,10);  % for better automatization, input chord distribution in
plate_dim.xlsx and have MATLAB calulate psi according to a & c-dist

b=a/AR_(ar)*1.2;      %% may not be optimal position to calculate

x=linspace(0,a,a_n)';
y=linspace(0,b,b_n)';


%%%%%%%%%%%%%%%%%%%%%%%%%%%%%%%%%%%%%%%%%%%%%%%%
%% improved_rrEFF.m --- Plate model RRM  %%
%% By. Luis Espinosa                     %%
%% EWEM Thesis          6-12-2017        %%
%%%%%%%%%%%%%%%%%%%%%%%%%%%%%%%%%%%%%%%%%%%%%%%%

clear w q_ite
mMax=5;
nMax=1;
lamb=5/12;
Beta=bpm*pi/180;
```

```
A11=A1(1,1);
A12=A1(1,2);
A22=A1(2,2);
A16=A1(1,3);
A26=A1(2,3);
A66=A(3,3);
D11=D(1,1);
D12=D(1,2);
D22=D(2,2);
D16=D(1,3);
D26=D(2,3);
D66=D(3,3);

for m=1:mMax

    M=m*pi/a;
    Nlamb=lamb*pi/b;

    if m==1 || m==3 || m==5 || m==7
        LAMB=0;
    elseif m==2 || m==4 || m==6 || m==8
        LAMB=(2*(1-cos(lamb*pi)/(M*Nlamb)));
    end



    C12=[A66*M*Nlamb*a*b/2];
    C13=[A11*M^3/4-A12*M*Nlamb^2/4+A16*M^2*Nlamb/4+A66*M*Nlamb^2/2]*LAMB;

    C21=[A66*M*Nlamb*a*b/2];
    C22=[A22*Nlamb^2*a*b/2+A66*M^2*a*b/2];
    C23=[A66*M^2*Nlamb/2-A22*Nlamb^3/4-A12*M^2*Nlamb/4]*LAMB;

    C31=[A11*M^3/2-A12*M*Nlamb^2/2-A16*M^2*Nlamb/2+A66*M^2*Nlamb]*LAMB;
    C32=[A66*M^2*Nlamb-A12*M^2*Nlamb/2-A22*Nlamb^3/2]*LAMB;
    C33a=[A11*M^4*a*b/64*(9-
12*sin(2*lamb*pi)/(2*lamb*pi)+3*sin(4*lamb*pi)/(4*lamb*pi))];
    C33b=[(A12+A66)*M^2*Nlamb^2*a*b/16*(1-sin(4*lamb*pi)/(4*lamb*pi))];

C33c=[A22*Nlamb^4*a*b/64*(9+12*sin(2*lamb*pi)/(2*lamb*pi)+3*sin(4*lamb*pi)/(4
*lamb*pi))];

    C33=C33a+C33b+C33c;

    C34=[D11*M^4*a*b/2+2*(D12+2*D66)*M^2*Nlamb^2*a*b+D22*Nlamb^4*a*b/2];
    C35=[M^2*a*b/2];

    C41=0;

    eps=1e-7;

    N=linspace(0,3e5,2e4)';
    q=0;

    for q=1:length(N)
```

```
        ite=1;
        wq=1;
        wq1=0;
        check=1;

        while check>=eps

            C11=[A11*M^2*a*b/2+A66*Nlamb^2*a*b/2-0*N(q)*M^2*a*b/4];
            K1=-(C12*(C21*C13)/C11-C23)/(C11*(C22-C21*C12/C11))-C13/C11;
            K2=(C21*C13/C11-C23)/(C22-C21*C12/C11);
            K3=(C34-N(q)*C35);
            wq1=wq-
((C31*K1+C32*K2+C33)*wq^3+K3*wq+C41)/(3*(C31*K1+C32*K2+C33)*wq^2+K3);

            check=abs(wq1-wq);

            if check<eps || check==0
                w(q)=wq1;
                q_ite(q)=ite;
            end
            wq=wq1;
            ite=ite+1;
        end

    end
        if ar==10
            w_out_ef(:,1)=w;
        elseif ar==20
            w_out_ef(:,2)=w;
        elseif ar==30
            w_out_ef(:,3)=w;
        elseif ar==40
            w_out_ef(:,4)=w;
        elseif ar==50
            w_out_ef(:,5)=w;
        else
        end

        for q=1:length(w)-1
            Ndiff(q)=(w(q+1)-w(q))/w(end);
        end

        Npos=min(find(Ndiff==max(Ndiff)));

        N_cr_eff(ar,m)=2*N(Npos)*b;
        M_buck(ar,1)=m;

end

%%%%%%%%%%%%%%%%%%%%%%%%%%%%%%%%%%%%%%%%%%%%%%%%
%% improved_rrIMP.m - stand alone              %%
%% By. Luis Espinosa                           %%
%% EWEM Thesis           9-01-2017             %%
%%%%%%%%%%%%%%%%%%%%%%%%%%%%%%%%%%%%%%%%%%%%%%%%
```

```
% NOTE: Imperfection modelling. Run stand-alone after running
% plate_model_main.m. Add first IMP=1 for twist imperfection
% or IMP=2 for prebend and w_ini=x [m]

clear w q_ite
mMax=5;
nMax=1;
lamb=5/12;
BETA=bpm;

A11=A1(1,1);
A12=A1(1,2);
A22=A1(2,2);
A16=A1(1,3);
A26=A1(2,3);
A66=A(3,3);
D11=D(1,1);
D12=D(1,2);
D22=D(2,2);
D16=D(1,3);
D26=D(2,3);
D66=D(3,3);

if IMP==1
    Beta=linspace(0,BETA,6);
    Max=6;
elseif IMP==2
    wini=[0,w_ini];
    Max=2;
    mMax=1;
    Beta=[0,0];
end

for ini=1:Max
for m=1:mMax

    M=m*pi/a;
    Nlamb=lamb*pi/b;
    q=1;

    if m==1 || m==3 || m==5 || m==7
        LAMB=0;
    elseif m==2 || m==4 || m==6 || m==8
        LAMB=(2*(1-cos(lamb*pi)/(M*Nlamb)));
    end


    C12=[A66*M*Nlamb*a*b/2];
    C13=[A11*M^3/4-A12*M*Nlamb^2/4+A16*M^2*Nlamb/4+A66*M*Nlamb^2/2]*LAMB;

    C21=[A66*M*Nlamb*a*b/2];
    C22=[A22*Nlamb^2*a*b/2+A66*M^2*a*b/2];
    C23=[A66*M^2*Nlamb/2-A22*Nlamb^3/4-A12*M^2*Nlamb/4]*LAMB;

    C31=[A11*M^3/2-A12*M*Nlamb^2/2-A16*M^2*Nlamb/2+A66*M^2*Nlamb]*LAMB;
```

```
    C32=[A66*M^2*Nlamb-A12*M^2*Nlamb/2-A22*Nlamb^3/2]*LAMB;
    C33a=[A11*M^4*a*b/64*(9-
12*sin(2*lamb*pi)/(2*lamb*pi)+3*sin(4*lamb*pi)/(4*lamb*pi))];
    C33b=[(A12+A66)*M^2*Nlamb^2*a*b/16*(1-sin(4*lamb*pi)/(4*lamb*pi))];

C33c=[A22*Nlamb^4*a*b/64*(9+12*sin(2*lamb*pi)/(2*lamb*pi)+3*sin(4*lamb*pi)/(4
*lamb*pi))];

    C33=C33a+C33b+C33c;

    C34=[D11*M^4*a*b/2+2*(D12+2*D66)*M^2*Nlamb^2*a*b+D22*Nlamb^4*a*b/2];
    C35=[M^2*a*b/2];

    if IMP==1
        C41=-0.5749*Beta(ini)*m*b^2*(sin(Beta(ini)*a-m*pi)/(Beta(ini)*a-
m*pi)+sin(Beta(ini)*a+m*pi)/(Beta(ini)*a+m*pi));
    elseif IMP==2
        C41=-2.9386*wini(ini)*(b/a);
    elseif IMP==3
        C41=0;
    else
    end

    eps=1e-7;

    N=linspace(0,3e5,2e4)';
    q=0;

    for q=1:length(N)
        ite=1;
        wq=1;
        wq1=0;
        check=1;

        while check>=eps

            C11=[A11*M^2*a*b/2+A66*Nlamb^2*a*b/2-0*N(q)*M^2*a*b/4];
            K1=-(C12*(C21*C13)/C11-C23)/(C11*(C22-C21*C12/C11))-C13/C11;
            K2=(C21*C13/C11-C23)/(C22-C21*C12/C11);
            K3=(C34-N(q)*C35);
            wq1=wq-
((C31*K1+C32*K2+C33)*wq^3+K3*wq+N(q)*C41)/(3*(C31*K1+C32*K2+C33)*wq^2+K3);

            check=abs(wq1-wq);

            if check<eps || check==0
                w(q)=wq1;
                q_ite(q)=ite;
            end
            wq=wq1;
            ite=ite+1;
        end

    end
```

```
    w_out_ini(:,ini)=w'+b*sin(Beta(ini)*a*pi/180)/10;

        for q=1:length(w)-1
            Ndiff(q)=(w(q+1)-w(q))/w(end);
        end

        Npos=min(find(Ndiff==max(Ndiff)));

        N_cr_imp(ini,m)=2*N(Npos)*b;
        M_buck(1,1)=m;

end
end

if IMP==1
    xlswrite('Wout twist',[N,w_out_ini])
elseif IMP==2
    xlswrite('Wout pre-b',[N,w_out_ini])
else
end
```

Code Input Files

material_db.xlsx

Mat_name	Exx	Eyy	Ezz	Gxy	Gyz	Gzx	muxy	muyz	muzx
biax	2.60E+10	2.60E+10	1.32E+10	1.35E+10	3.53E+09	3.53E+09	0.15	0.15	0.08
epik	8.80E+08	8.80E+08	8.80E+08	8.80E+08	8.80E+08	8.80E+08	0.35	0.35	0.35
empty	0	0	0	0	0	0	0	0	0

sig_t_xx	sig_t_yy	sig_t_zz	sig_c_xx	sig_c_yy	sig_c_zz	tau_xy	tau_yz	tau_zx	Rho*h
1.30E+08	1.30E+08	8.50E+07	1.30E+08	1.30E+08	1.47E+08	7.60E+07	7.60E+07	4.50E+07	1.79E+03
6.00E+07	6.00E+07	6.00E+07	6.00E+07	6.00E+07	6.00E+07	3.40E+07	3.40E+07	3.40E+07	1.20E+03
0	0	0	0	0	0	0	0	0	0

plate_dim.xlsx

FS mat	FS thick	C mat	C thick	chord	a	twist/m	AR max	a_n	b_n	skew Psi
biax	0.0004	biax	0.002	1.5785	0.5	5	6	50	20	0
biax	0.003	epik	0.006	1.5785	0.5	5	6	50	20	1

Citations

[1] J. G. Holierhoek. Aeroelasticity of Large Wind Turbines. TU Delft. Faculty of Aerospace Engineering. 19-November-2008.

[2] M. A. Eder, R. D. Bitsche, Fracture analysis of adhesive joints in wind turbine blades. Wind Energy 2014. Research Gate. 2015.02.23

[3] M. H. Hansen, T. Kim, C. Bak, M. Mirzaei. Loads, Aerodynamics and Control – Basics of wind turbine aero-servo-elasticity. DTU Wind Energy. Department of Wind Energy.

[4] F. M. Jensen, K. Branner. Introduction to Wind Turbine Blade Design – Advances in Wind Turbine Blade Design and Materials. Woodhead Publishing Series in Energy. 2013. Pages 3-28.

[5] A. Buliga, F. M. Jensen. Blade Failure Catalogue Version 2.0. Bladena. Ringsted, 2014.

[6] J.D. Sørensen, K. Branner & H. Stensgaard Toft, (2013) Recommendations for future subcomponent tests: EUDP: Experimental blade research. - Phase 2 (EBR2). Milestone 6

[7] Dr. B. Stoevesandt. F. Sayer, J. Peinke, A.v. Wingerde, H. Rahimi, M. Rosemeier. Advances in Rotor Blade Design. IWES Fraunhofer.

[8] F. Lahuerta. Trailing Edge Buckling Tests. Knowledge Center WMC. EU FP7 Framework Programme IRPWind Project. 17-August-2016.

[9] P. U. Haselbach, M. A. Eder, F. Belloni, A comprehensive investigation of trailing edge damage in a wind turbine rotor blade. Wind Energy 2016. Wiley Online Library. 2015.11.22

[10] Nielsen, M., Jensen, F. M., Nielsen, P. H., Berring, P., Martyniuk, K., Roczek, A., ... Rasmussen, J. J. A. (2010). Full Scale Test of SSP 34m blade, edgewise loading LTT: Data Report 1. Roskilde: Danmarks Tekniske Universitet, Risø Nationallaboratoriet for Bæredygtig Energi. (Denmark. Forskningscenter Risoe. Risoe-R; No. 1718(EN)).

[11] Nielsen, M., Roczek-Sieradzan, A., Jensen, F. M., Nielsen, P. H., Berring, P., Sieradzan, T., ... Jensen, C. (2010) Full Scale Test SSP 34m blade, edgewise loading LTT. Extreme load and PoC InvE Data report. Roskilde: Danmarks Tekniske Universitet, Ris Nationallaboratoriet for Bredygtig Energi. (Denmark. Forskningscenter Risoe. Risoe-R; No. 1748(EN)).

[12] M. Rosemeier, F. Lahuerta, K. Branner & A. Antoniou, SP3 - Structural Design and Materials, Subcomponent testing of wind turbine blades. IRPWind Conference. Amsterdam, The Netherlands. 2016.09.20

[13] F. Lahuerta, R. Njissen. Buckling tests on trailing edges. Preliminary FE. Hinge at the middle of the CAP. Project 4810A. Report number WMC-2016-007-cc Knowledge Center WMC. Wieringerwerf, The Netherlands. 2016.02.23

[14] K. Branner, P. Berring, P.U. Haselbach. Subcomponent testing of trailing edge panels in wind turbine blades. Dept. of Wind Energy, Denmark Technical University. Roskilde, Denmark. 17th European Conference on Composite Materials. Munich, Germany. 2016.06.26-30

[15] M. Rosemeier, P. Massart, A. Antoniou. WP 7.1 Status Update - Trailing Edge Sub-component

Test 3rd Technical Meeting. Roskilde, Denmark. 2016.04.29

[16] R. Daripa, M.K. Singha. Influence on corner stresses on the stability characteristics of composite skew plates. Department of Applied Mechanics, Indian Institute of Technology. New Delhi, India. 2008.10.21

[17] J.E. Helms, G. Li, S.S. Pang. Buckling analysis of a taper-taper adhesive bonded joint. Department of Mechanical Engineering. Louisiana State University. Louisiana, USA. 2003.02

[18] E. M. Mockensturm. Department of Mechanical and Nuclear Engineering. Pennsylvania State University, University Park. PA 16802 Journal of Applied Mechanics Vol. 68 p. 561-567. 2001.07

[19] D.J. Crispino, R.C. Benson. Stability of twisted orthotropic plates. Department of Mechanical Engineering, Hopeman Building. University of Rochester, Rochester NY. 1986.01.28

[20] Technical Specification EIC TS 61400-23. Wind Turbine Generator Systems. Part 23: full Scale Structural Testing of Rotor Blades. Danish Standards Foundation. First Edition: 2001-2004.

[21] F. Lahuerta, M.J. de Ruiter, L.Espinosa, N. Koorn, D. Smissaert. Assessment of Wind Turbine Blade Trailing Edge Failure with Sub-Component Tests. Knowledge Center WMC. Wieringerwerf, The Netherlands. 21st International Conference on Composite Materials. Xi'an. 20-25-09-2017.

[22] Sambamurty, Saravakota. Trailing edge bonding cap for wind turbine rotor blades. General Electric Company. Patent US 2011/0142661 A1. 16 June 2011.

[23] Rao, Kavala V. Wind Turbine Blade with Improved Trailing Edge Bond. General Electric Company. Patent US 2011/0142668 A1. 16 June 2011.

[24] H.H.E.Leipholz. Stability of Elastic plates via Lyapunov's Second Method. Ingeniur Archiv 45 (1976) 337-345. Springer-Verlag.

[25] C. Kassapoglou. Design and Analysis of Composite Structures with Applications to Aerospace Structures. Delft University of Technology. Delft, The Netherlands. John Wiley & Sons, Ltd. 2013

[26] D. O. Brush, B. O. Almroth. Buckling of Bars, Plates and Shells. International Student Edition. McGraw-Hill Inc. 1975.

[27] Barbero, E.J., Introduction to Composite Material Design, Taylor & Francis Inc, Philadelphia, PA, 1999,

Chapter 9.

[28] Load and Resistance Factor Design Specification for Structural Steel Buildings. Comm. C2, Page 189. 27-December-1999.

[29] Structural Steel Design and Analysis. Introduction to Axially Loaded Compression Members. End Restraint and Effective Length of Columns. Slide 8. University of Maryland, Department of Civil and Environmental Engineering. 2002.

[30] H. Kim, H. Kwon. Buckling of composite flanges in partially disbonded adhesive joints. School of Aeronautics and Astronautics. Purdue University. Indiana, USA. 2004.04.06

[31] D. W. Jensen, P. A. Lagace. Influence of Mechanical Couplings on the Buckling and Postbuckling of Anisotropic Plates. Massachussetts Institute of Technology, Cambridge MA. AIAA Journal October 1988.

[32] G. Singh, G.V. Rao, N.G.R. Iyengar. Large deflection bending of rectangular antisymmetric cross-ply plates. Composite Structures 0263-8223/91/S03.50. Elsevier Science Publishers Ltd.

[33] Ganesh, Rana. 3D Constitutive Equations for Orthotropic Materials and Stress-Stress transformations. Composite Materials. NPTEL 2014.

[34] F. Lahuerta. Thickness Effect in Composite Laminates in Static and Fatigue Loading. TU Delft, 18-01-2017.

[35] Upwind Optidat Database. WMC Knowledge Center. Available at https://www.wmc.eu/optimatblades_optidat.php.

[36] MSC Marc 2016. Volume B: Element Library. MSC Marc Mentat Documentation. MSC Software Corporation. 2016.

[37] J. Tang. Semi-Analytical Solution to Buckling of Variable-Stiffness Composite Panels. TU Delft. Aerospace Structures & Computational Mechanics. May 2015.